KU LEUVEN

Development of High-Quality Perovskite Materials for Efficient and Stable Radiation Detection

Lotte Clinckemalie

Supervisor:
Prof. Dr. Elke Debroye

Co-supervisors:
Prof. Dr. Johan Hofkens
Dr. Bapi Pradhan

Members of the Examination Committee:
Prof. Dr. Wim Dehaen, Chairman
Prof. Dr. Ir. Maarten Roeffaers
Prof. Dr. Steven Defeyter
Prof. Dr. Ir. Rob Ameloot
Prof. Dr. Hai Wang (Max-Planck Institute)

Dissertation presented in partial fulfillment of the requirements for the Degree of Doctor of Science (PhD)

6th September 2023

© 2023 KU Leuven, Science, Engineering & Technology
Uitgegeven in eigen beheer, Lotte Clinckemalie, Leuven, Belgium.

Alle rechten voorbehouden. Niets uit deze uitgave mag worden vermenigvuldigd en/of openbaar gemaakt worden door middel van druk, fotokopie, microfilm, elektronisch of op welke andere wijze ook zonder voorafgaandelijke schriftelijke toestemming van de uitgever.

All rights reserved. No part of the publication may be reproduced in any form by print, photoprint, microfilm, electronic or any other means without written permission from the publisher.

Acknowledgements

Five years ago, I embarked on a journey that would forever shape me as a person. Even though it feels like I just began my PhD, writing these words make me realize more than ever that I just ended what has been one of the most intense periods of my entire life. This journey has been educational on both a professional and personal level, filled with many beautiful and challenging moments. This PhD thesis was only made possible by the continuous support and encouragement of many exceptional individuals, whom I would like to thank from the bottom of my heart.

First of all, I want to express my gratitude to Prof. Johan Hofkens for giving me the opportunity to start my PhD journey within his research group. I am thankful for all the support and guidance I received from him during these years. I am particularly appreciative on the countless FWO mocking sessions, for which he dedicated time during the weekend, giving me the best possible start!

Secondly, and most importantly, I would like to thank Prof. Elke Debroye for being my science mother, becoming my promotor and for always bringing out the best in me. You have taught me everything, from the fundamentals of spectroscopy, up until writing a proper scientific manuscript. Not only are you my promotor, but also a friend, with whom I have shared many moments of laughter, cups of coffee with science or personal discussions, and most importantly, glasses of wine!

Next, I extend my gratitude to Prof. Maarten Roeffaers. From solving my lab problems (one time even together in the actual lab), to providing feedback on my research, you were always there to answer my questions. The incredible team-buildings were also greatly appreciated, thank you! I also want to thank Dr. Bapi Pradhan, who taught me numerous insights and strategies for overcoming challenges I encountered during my research. Your remarkable ideas and the opportunity to explore them in the lab have been invaluable.

I wish to express my gratitude to the examination committee. Prof. Wim Dehaen, thank you for ensuring the smooth execution of the preliminary and public defense. Prof. Steven Defeyter, your role as an assessor and guide throughout my entire PhD journey is deeply appreciated. I am also grateful for Prof. Rob Ameloot as his critical feedback played a vital role in shaping this

manuscript into its final form. Lastly, I extend my thanks to Prof. Hai Wang for our collaboration over the past years. I am extremely grateful for the chance to have visited your lab and for the valuable insights you, Samir, Lei and Heng have contributed to our research.

I would also like to thank all colleagues in the perovskite research group for the many joyful moments and enriching discussions over the years! But most importantly, a special shout-out to the best office mates one could ask for: Harshita, Giacomo, Donato, Li and Bjorn. Thank you for the shared laughter, tears, hugs, coffees, beers, pizza, brownies, and for always being there, both professionally as personally. I feel immensely grateful to have shared an office with all of you!

I would also like to thank my thesis students Simon, Dean, Arnout, Roeland, Jolien and Roel for tolerating my crazy ideas. I am proud of each of you and have thoroughly enjoyed mentoring you. Roel, I wish you and Liam good luck continuing this research; you've got this!

Life would not be the same without some exceptional friends! I am genuinely thrilled to be surrounded by such amazing people. *De harde kern*: Xana, Anne-Charlotte, Michael, Wim, Jan-Willem, Kwinten, Jef, Karel, Jorik, Flip, Wouter, Yenthel and Mark. *The girls*: Chiara, Laura and Caroline. *The boys*: Matthias and Quinten. Your presence has enriched my life beyond measure!

Family is the biggest support system one could have. I would like to thank my Mom, Dad, Stijn and Jolien for their emotional support and belief in me. Also, for the joyous times during family weekends and dinner gatherings. I would also like to thank my family-in-law for those very same reasons.

Lastly, and certainly not the least, I want to express my deep gratitude to my fiancé Pieter, who has always been an unconditional support and encouragement over the past few years. I look forward to marrying you and spending the rest of our life together, accompanied by our beloved cat, Milou.

Summary

X-ray imaging is experiencing a significant growing demand in medical diagnostics, resulting in an expected market growth up to €3.8 Bn by 2027. However, the rise in X-ray imaging has led to more frequent exposure of harmful radiation to the human body, which in turn increases radiation-related health risks. To minimize the necessary X-ray exposure for obtaining an image, extensive research is being performed to develop more sensitive X-ray detectors.

In the quest for more sensitive materials to reduce the operating radiation dose, metal halide perovskites (MHPs) hold significant potential due to their unique physicochemical properties. However, they still face significant challenges that hinder their commercial availability. One of the main obstacles is the long-term stability of the material. The most popular Pb-based MHPs can undergo phase transitions or complete degradation in response to environmental changes, resulting in a loss of the desirable optoelectronic properties. Another challenge is the deposition of large-area MHP layers for device applications, as conventional fabrication methods typically result in films with a high defect density. Finally, the eco-toxicity of lead-containing perovskites is cited as hampering their future implementation in realistic devices. A viable alternative to the lead halide perovskites are the so called double perovskites, as the corresponding single crystals have proven to generate sensitive and stable X-ray detectors. However, the synthesis of high-quality nano- or microcrystals needs to be developed for their implementation in large-area devices.

This PhD dissertation presents several promising pathways to address these challenges. Stable, phase-pure, highly crystalline lead-based and lead-free perovskites with excellent photonic properties have been successfully synthesized, characterized and investigated for their potential application as radiation detectors. In Chapter 1, an introduction on $CsPbBr_3$ perovskite single crystals, microcrystals, nanowires, thin films, and nanocrystals was provided, highlighting the importance and challenges of diverse synthesis strategies of perovskite materials on the final performance as photo- and X-ray detectors.

In Chapter 3, a new scalable fabrication method of compact, thick, and pinhole-free $CsPbBr_3$ films was presented. Furthermore, we investigated how the implementation of the 2D $CsPb_2Br_5$ phase into $CsPbBr_3$ microcrystals affects their structural and optical properties. It was found that the

dual-phase sample demonstrates improved tolerance to higher voltage X-ray detection as it exhibits a much lower dark current, linked to suppressed ion migration. The demonstrated low dark current in combination with the plausible formation of shallow defect states, prevent the building up of polarization in the device configuration. This increased stability to higher voltage regimes provides a promising avenue for future improvements in fast, local charge extraction and X-ray image resolution.

In Chapter 4, chemical vapor deposition was applied as an advanced synthesis strategy to fabricate smooth, high-quality and phase-pure $CsPbBr_3$ thin films. The impact of the grain size on the carrier transport properties has also been examined, indicating an enhanced mobility upon increased grain size. Additionally, Rb-doping was performed as a strategy to boost the performance of the films as the photoactive layer in photodetectors. Finally, the insights gained from this research were utilized to optimize a home-built setup for the fabrication of $CsPbBr_3$ thin films, with the aim of expanding this strategy towards other (lead-free) perovskite materials in the future.

In Chapter 5, the potential application of lead-free perovskite $Cs_2AgBiBr_6$ microcrystals in the field of photodetection was highlighted. Cation exchange transformation was suggested as a synthesis method to fabricate microcrystals of higher quality compared to crystals fabricated by direct synthetic routes. To gain insights in the cation exchange process, the reaction mechanism from $Cs_3Bi_2Br_9$ to $Cs_2AgBiBr_6$ has been studied to understand the crystal phase evolution as well as the changes in structural and optical properties of the materials at different stages of the reaction. Furthermore, a proof-of-concept photodetector device indicated that the $Cs_2AgBiBr_6$ microcrystals obtained by cation exchange exhibit an improved photoresponse when compared to those obtained by the direct antisolvent precipitation synthesis method. This crystallographic transformation may pave pathway for the development of difficult-to-access perovskite structures, which are not available via direct solution-based synthesis pathways.

Overall, the findings presented in this PhD dissertation contribute to the advancement of Pb-based and lead-free MHP materials for radiation detection. Three promising synthesis methods were explored and optimized to address the challenges related to the material stability of MHPs, the development of large-area pinhole-free films for device fabrication, and the lead toxicity. This PhD dissertation provides valuable insights obtained via advanced structural and optical studies and indicates the potential of perovskites as low- and high-energy photodetectors in the future.

Samenvatting

In de medische diagnostiek is er een sterk groeiende vraag naar röntgenbeeldvorming, wat resulteert in een verwachte marktgroei tot € 3,8 miljard in 2027. De toename van röntgenbeeldvorming heeft echter geleid tot een meer frequente blootstelling van de schadelijke X-ray straling op het menselijk lichaam, wat op zijn beurt de stralingsgerelateerde gezondheidsrisico's verhoogt. Om de benodigde röntgenstraling voor het verkrijgen van een beeld te minimaliseren, wordt er uitgebreid onderzoek gedaan naar de ontwikkeling van gevoeligere röntgendetectoren.

In de zoektocht naar gevoeligere materialen om de operationele stralingsdosis te verminderen, hebben metaalhalogenide perovskieten (MHPs) een aanzienlijk potentieel vanwege hun unieke fysische en chemische eigenschappen. Ze staan echter nog steeds voor grote uitdagingen die hun commerciële beschikbaarheid belemmeren. Een van de belangrijkste obstakels is de stabiliteit van het materiaal op lange termijn. De meest populaire op lood gebaseerde MHPs kunnen faseovergangen of volledige degradatie ondergaan als reactie op veranderingen in de omgeving, wat resulteert in het verlies van de gewenste opto-elektronische eigenschappen. Een andere uitdaging is de afzetting van MHP-lagen met een groot oppervlak voor de implementatie in een apparaat, aangezien conventionele fabricagemethoden doorgaans resulteren in films met een hoge defectdichtheid. Ten slotte wordt de ecotoxiciteit van loodhoudende perovskieten genoemd als een belemmering voor hun toekomstige implementatie in realistische apparaten. Een alternatief voor de op lood gebaseerde MHPs zijn de zogenaamde dubbele perovskieten, aangezien dat de overeenkomstige millimeter kristallen reeds bewezen om gevoelige en stabiele röntgendetectoren te genereren. De synthese van hoogwaardige nano- of microkristallen moet echter worden ontwikkeld voor hun implementatie in apparaten met een groot oppervlak.

Dit doctoraatsproefschrift presenteert verschillende veelbelovende wegen om deze uitdagingen het hoofd te bieden. Stabiele, zuivere en zeer kristallijne op lood gebaseerde en loodvrije perovskieten met uitstekende fotonische eigenschappen zijn met succes gesynthetiseerd, gekarakteriseerd en onderzocht op hun potentiële toepassing als stralingsdetectoren. In hoofdstuk 1 werd een inleiding gegeven over $CsPbBr_3$ perovskiet millimeter kristallen, microkristallen, nanodraden, dunne films en nanokristallen, waarbij het belang en de uitdagingen van verschillende synthesestrategieën

van perovskiet materialen voor de uiteindelijke prestaties als foto- en röntgendetectoren werden benadrukt.

In hoofdstuk 3 werd een nieuwe, schaalbare fabricagemethode voor compacte, dikke en gaatjesvrije $CsPbBr_3$-films gepresenteerd. Verder hebben we onderzocht hoe de implementatie van de 2D $CsPb_2Br_5$-fase in $CsPbBr_3$-microkristallen hun structurele en optische eigenschappen beïnvloedt. Er werd ontdekt dat het tweefasige staal verbeterde tolerantie vertoont voor röntgendetectie met een hoger voltage, aangezien het een veel lagere donkerstroom vertoont, gekoppeld aan onderdrukte ionenmigratie. De aangetoonde lage donkerstroom in combinatie met de plausibele vorming van ondiepe defecttoestanden voorkomt de opbouw van polarisatie in de apparaat configuratie. Deze verbeterde stabiliteit voor hogere spanningsregimes biedt een veelbelovende weg voor toekomstige verbeteringen in snelle, lokale ladingsextractie en röntgenbeeldresolutie.

In hoofdstuk 4 werd chemische dampafzetting toegepast als een geavanceerde synthesestrategie om gladde, hoogwaardige en fasezuivere dunne $CsPbBr_3$-films te maken. De impact van de korrelgrootte op de transporteigenschappen van de drager werd ook onderzocht, wat wijst op een verbeterde mobiliteit bij een grotere korrelgrootte. Bovendien werd Rb-dopering uitgevoerd als een strategie om de prestaties van de films als fotoactieve laag in fotodetectoren te verbeteren. Ten slotte werden de inzichten uit dit onderzoek gebruikt om een zelfgemaakte opstelling voor de fabricage van $CsPbBr_3$ dunne films te optimaliseren, met als doel om deze strategie in de toekomst uit te breiden naar andere (loodvrije) perovskiet materialen.

In hoofdstuk 5 werd het potentieel van loodvrije perovskiet $Cs_2AgBiBr_6$ microkristallen op het gebied van fotodetectie belicht. Transformatie door kationenuitwisseling werd voorgesteld als een synthesemethode om microkristallen van hogere kwaliteit te vervaardigen in vergelijking met kristallen die via directe synthetische routes zijn vervaardigd. Om inzicht te krijgen in het kationenuitwisselingsproces, is het reactiemechanisme van $Cs_3Bi_2Br_9$ tot $Cs_2AgBiBr_6$ bestudeerd om de kristalfase-evolutie te begrijpen, evenals de veranderingen in structurele en optische eigenschappen van de materialen in verschillende stadia van de reactie. Bovendien gaf een *proof-of-concept* fotodetectorapparaat aan dat de $Cs_2AgBiBr_6$-microkristallen verkregen door kationenuitwisseling een verbeterde fotorespons vertonen in vergelijking met die verkregen door de directe synthesemethode. Deze kristallografische transformatie kan de weg banen voor de ontwikkeling van

moeilijk toegankelijke perovskiet structuren, die niet beschikbaar zijn via directe syntheseroutes.

Over het algemeen dragen de bevindingen in dit proefschrift bij aan de vooruitgang van op lood gebaseerde en loodvrije perovskiet materialen voor stralingsdetectie. Er werden drie veelbelovende synthesemethoden onderzocht en geoptimaliseerd om de uitdagingen aan te gaan die verband houden met de materiaalstabiliteit van MHPs, de ontwikkeling van grote gaatjesvrije films voor de fabricage van apparaten en de loodtoxiciteit. Dit doctoraatsproefschrift biedt waardevolle inzichten verkregen via geavanceerde structurele en optische studies en geeft het potentieel aan van perovskieten als laag- en hoogenergetische fotodetectoren in de toekomst.

List of Abbreviations

a-Se	Amorphous selenium
AVC	Antisolvent-assisted vapor crystallization
BT	Bridgman technique
CE	Cation exchange
CVD	Chemical vapor deposition
D	X-ray dose rate
D*	Detectivity or detection sensitivity
DAS	Decay associated spectra
DCM	Dichloromethane
DMF	N,N-dimethylformamide
DMSO	Dimethylsulfoxide
DP	Double perovskite
$\Delta\sigma$	Photoconductivity
E_0	THz electric field without photoexcitation
ε_0	Vacuum permittivity
E_g	Bandgap energy
E_{pump}	THz electric field with photoexcitation
E(t)	Electric field
EQE	External quantum efficiency
eV	Electron volt
FPD	Flat panel detector
HAD	1,6-hexamethylenediamine
HBr	Hydrobromic acid
HTL	Hole transport layer
I_d	Dark current
I_p	Photocurrent
IPA	Isopropanol
ITC	Inverse temperature crystallization
ITO	Indium tin oxide
I-V	Current-voltage
K	Conversion rate constant
k_1	Monomolecular recombination rate constant

k_2	Bimolecular recombination rate constant
k_3	Auger recombination rate constant
LARP	Ligand-assisted reprecipitation
LDR	Linear dynamic range
LEDs	Light-emitting diodes
λ_{em}	Emission wavelength
λ_{exc}	Excitation wavelength
m*	Effective mass
MCs	Microcrystals
MeCN	Acetonitrile
MeOH	Methanol
MHPs	Metal halide perovskites
n	Avrami exponent
N	Carrier density
NCs	Nanocrystals
NSs	Nanosheets
n(t)	Time-dependent carrier density
n_{trap}	Trap density
NWs	Nanowires
OAc	Oleic acid
OAm	Oleylamine
OPTP	Optical pump-THz probe
P/D	Photo-to-dark current ratio
PAA	Pressure-assisted annealing
PDMS	Polydimethylsiloxane
PEN	Polyethylene naphthalate
PET	Polyethylene terephthalate
PL	Photoluminescence
PLQY	Photoluminescence quantum yield
PVB	Polyvinyl butyral
QDs	Quantum dots
R	Responsivity
rps	Rotations per second
RT	Room temperature
S	Effective device area

S/N	Signal-to-noise ratio
SCLC	Space-charge-limited current method
SCs	Single crystals
SEM	Scanning electron microscopy
SI	Supporting information
t	Reaction time
τ	Time constant
T_1	Evaporation temperature
T_2	Substrate temperature
t_P	Pump probe delay time
τ_s	Scattering time
TCSPC	Time-correlated single photon counting
THz-TDS	Ultrafast and contact-free THz time-domain spectroscopy
μτ	Mobility-lifetime product
V_{bias}	Bias voltage
VLS	Vapor-liquid-solid
VP	Vapor-phase
W	Energy required to create an electron-hole pair
XRD	X-ray diffraction
ω	Angular frequency
ω_p	Plasma frequency

Table of Contents

Acknowledgements i

Summary iii

Samenvatting v

List of Abbreviations ix

Table of Contents xiii

Chapter 1 State-of-the-art Perovskite Research 1

Abstract 2

1.1 Introduction to Perovskites 3

1.2 Single Crystals 9

1.3 Microcrystals 18

1.4 Nanowires 25

1.5 Thin Films 34

1.6 Nanocrystals 38

1.7 Hybrid Nanocrystal Photodetectors 42

1.8 Summary and Outlook 46

1.9 References 48

Chapter 2 Motivation and Objectives 61

2.1 Motivation 62

2.2 Objectives of the Research 64

2.3 References 66

Chapter 3 Phase-Engineering Compact and Flexible $CsPbBr_3$ Microcrystal Films for Robust X-ray Detection 69

Situation in this PhD Dissertation 70

Abstract 70

3.1 Introduction 71

3.2 Results and Discussion 72

3.3 Conclusion 81
3.4 Supporting Information 82
3.4.1 Experimental Section 82
3.4.2 Material Characterization 83
3.4.3 Supporting Information for Results and Discussion 85
3.5 References 87
Chapter 4 Fabrication of High-Quality $CsPbBr_3$ Perovskite Films Using Chemical Vapor Deposition 95
Situation in this PhD Dissertation 96
Abstract 96
4.1 Introduction 97
4.2 Results and Discussion 99
4.3 Conclusion and Outlook 109
4.4 Supporting Information 110
4.4.1 Experimental Section 110
4.4.2 Material Characterization 110
4.4.3 Supporting Information for Results and Discussion 111
4.5 References 116
Chapter 5 Transformation of $Cs_3Bi_2Br_9$ to $Cs_2AgBiBr_6$ Lead-Free Perovskite Microcrystals Through Cation Exchange 121
Situation in this PhD Dissertation 122
Abstract 122
5.1 Introduction 123
5.2 Results and Discussion 124
5.3 Conclusion 132
5.4 Supporting Information 133
5.4.1 Experimental Section 133
5.4.2 Material Characterization 134
5.4.3 Supporting Information for Results and Discussion 135

5.5 References 144
Chapter 6 Conclusion and Outlook 149
6.1 General Conclusions 150
6.2 Outlook 151
6.3 References 154
Appendix 155
1. Safety Information 156
2. List of Publications 157
3. Student Supervision 157

Chapter 1
State-of-the-art Perovskite Research

This chapter is based on: Challenges and Opportunities for $CsPbBr_3$ Perovskites in Low- and High-Energy Radiation Detection (*ACS Energy Lett*. 2021, 6, 1290−1314.)

Lotte Clinckemalie[#], Donato Valli[#], Maarten B. J. Roeffaers, Johan Hofkens, Bapi Pradhan, Elke Debroye**

Copyright © 2021 American Chemical Society

Reproduced with permission

Author contributions:

[#]L.C. and D.V. contributed equally to the manuscript. L.C., D.V., B.P and E.D. extensively explored the literature and wrote the review paper. B.P. and E.D. designed the general outline. M.B.J.R. and J.H. revised the text.

Abstract

Semiconductor-based light detection finds widespread application in everyday devices. Since the fabrication of commercial photodetectors requires complex and capital-intensive equipment, a search for semiconductors with low-cost processing is essential. To this end, hybrid organic-inorganic metal halide perovskites (MHPs) have gained interest due to their facile processing, in combination with their outstanding properties, such as efficient light absorption and high carrier mobility. Recently, all-inorganic $CsPbBr_3$ has emerged as a promising candidate for photodetection due to its favorable intermediate bandgap, and superior photo-, thermal and moisture stability. Different synthesis strategies have been adopted to obtain highly crystalline $CsPbBr_3$ perovskites with a large variety in morphology and dimension, each allowing for a specific photodetector application, e.g., cameras for handheld devices, large-area flat panel detectors and flexible light sensors. This review provides a comprehensive overview and evaluation of the state-of-the-art preparation and photodetector integration of $CsPbBr_3$ single crystals, microcrystals, nanowires, thin films, and nanocrystals.

1.1 Introduction to Perovskites

Photodetectors, converting incident photons into readable electrical signals, form the cornerstone of everyday electronic devices with widespread application in medical and security imaging, communication, remote control, chemical and biological sensing, artificial intelligence, etc. An ideal semiconductor photodetector should exhibit (i) efficient light absorption over a wide spectral range, (ii) a high photo-to-dark current ratio, (iii) a high mobility of photogenerated charge carriers, (iv) negligible charge trapping, (v) long-term device operational stability and (vi) low-cost upscaling. On the one hand, commercial photodetectors based on GaN, Si and InGaAs materials require complex and capital-intensive equipment along with sophisticated high-vacuum sputtering and high-temperature chemical vapor deposition techniques. Moreover, an electronic preamplifier is frequently required to enhance weak electrical signals from these devices. On the other hand, three-dimensional metal halide perovskites (MHPs) are ionic semiconductor solids with remarkable optoelectronic properties, such as a direct bandgap, high absorption coefficients, long-range charge carrier dynamics, easy bandgap tunability, and high defect tolerance. Moreover, the low-temperature solution processability and earth-abundant low-cost precursors make them attractive semiconductors towards novel, high-performance optoelectronic devices.[1–4] To highlight the commercial potential of this material, it has been estimated that the raw cost per gram of $CsPbBr_3$ is around $ 3.1 ($ 0.3 after industrial scaling up), which is comparable to the price of commercial scintillators (e.g., 2.5 $/g for CsI:Tl) and can be estimated to be two orders of magnitude lower than other semiconductors like CdZnTe (ca. 500 $/g).[5,6] MHPs exhibit the empirical chemical formula ABX_3, where A is a monovalent cation (e.g., Cs^+, $CH_3NH_3^+$), B is a divalent cation (e.g., Pb^{2+}, Sn^{2+}) and X is a halide. Note that lead toxicity is a potential issue; however, recent studies have shown that low amounts in combination with proper recycling channels should minimize this risk.[7] Although MHPs have found extensive applications in solar cells and light-emitting diodes (LEDs), the implementation of these materials as the active layer in photodetectors has received prominent attention only recently.

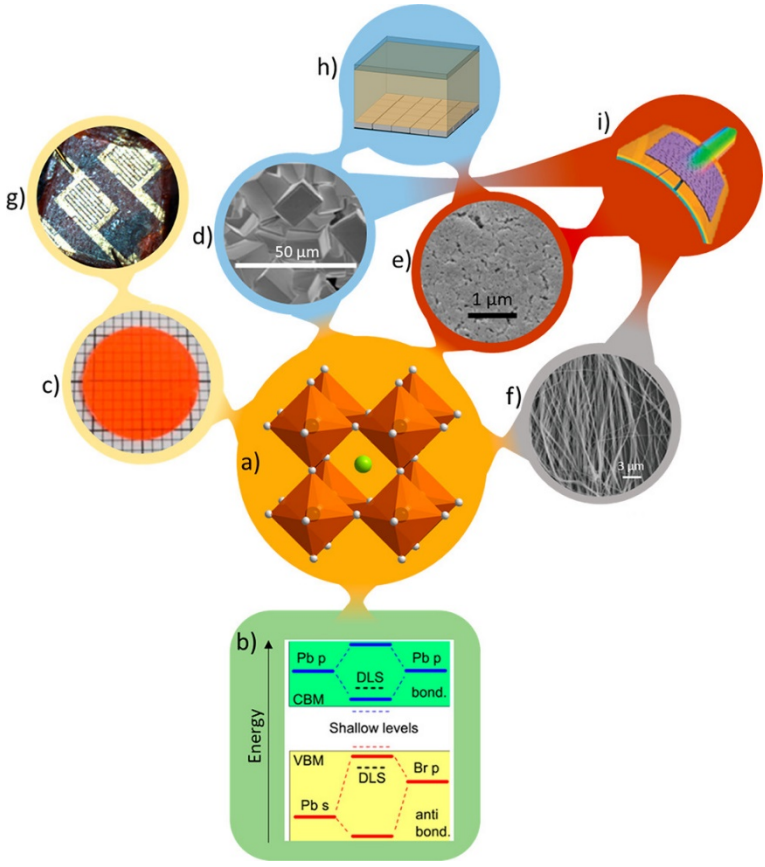

Scheme 1. (a) $CsPbBr_3$ crystal structure. (b) Illustration of the formation of shallow defect levels in $CsPbBr_3$[8], (c-f) Examples of the different $CsPbBr_3$ reported dimensionalities, ranging from (c) single crystals[9] and (d) microcrystals[10], to (e) thin-films[11] and (f) nanowires[12]. (g-i) Different applications belonging to the varying dimensionalities; (g) single pixel cameras (from IR to γ-rays)[13]. (h) flat panel detectors (soft to hard X-rays), (i) flexible detectors (from UV-visible to X-rays)[14]. Reprinted with permission from (b) reference 8, copyright 2017, American Chemical Society; (c) reference 9, copyright 2018, American Chemical Society; (d) reference 10, copyright 2018, American Chemical Society; (e) reference 11, copyright 2018, Royal Society of Chemistry; (f) reference 12, copyright 2018, Royal Society of Chemistry; (g) reference 13, copyright 2016, Wiley-VCH Verlag GmbH & Co. KGaA, Weinheim.; (i) reference 14, copyright 2016, Wiley-VCH Verlag GmbH & Co. KGaA, Weinheim.

Dou *et al*. fabricated the first MHP-based photodetector based on a solar cell architecture with a $CH_3NH_3PbI_{3-x}Cl_x$ absorbing layer in 2014.[15] Since then, MHP-based photodetectors have seen a tremendous upsurge. Devices based on hybrid organic-inorganic MHPs achieved high photoresponsivities up to 2.6×10^6 AW^{-1}.[16] However, those detectors showed rapid performance degeneration in ambient air, which is associated with the volatile nature of the organic cation.[17,18] In contrast, all-inorganic $CsPbX_3$ (X = Cl, Br, I) MHPs have enhanced structural, chemical, and thermal stability in ambient air for more than two months.[19,20] Unlike $CsPbI_3$, which only exhibits its photoactive perovskite phase above 350 °C, and $CsPbCl_3$, which has a relatively large bandgap, $CsPbBr_3$ exhibits remarkable stability at room temperature (RT) with an intermediate bandgap of 2.3 eV, allowing the fabrication of stable photonic devices.[21–25] The low-bandgap, photoactive black $CsPbI_3$ α-cubic phase is structurally stable only above 300 °C. At room temperature, the bulk phase spontaneously transforms to the photoinactive yellow orthorhombic phase due to a size mismatch between the Cs cation and the PbI_6 sublattice, making it an unsuitable candidate for high performance light to charge conversion devices.[26]

The possibility of a wide range of industrially relevant photodetector applications across the different length scales at which $CsPbBr_3$ MHP have been applied is shown in Scheme 1. Apart from the detection of low-energy photons close to the bandgap, the $CsPbBr_3$ optoelectronic properties are also favorable for high-energy X-ray and nuclear (e.g., gamma ray, γ-ray) radiation detectors, which are currently in high demand in medical and industrial imaging, in security and for fundamental scientific research purposes.[27,28] Even though the general operational mechanism of high-energy radiation detectors is similar to that of a low-energy photodetector, they have a few additional prerequisites to ensure excellent performance: (i) strong interaction with high-energy photons, which is fulfilled by the high effective atomic number, Z_{eff}, of $CsPbBr_3$ resulting in strong radiation attenuation, and (ii) stability under high electrical bias (100-500 keV) operation as well as (iii) a low leakage current, which are fulfilled by properly adapted device architectures.[27,28,29,30]

Although exciting progress in $CsPbBr_3$-based photodetectors has been made, the limited responsivity and slow photoresponse are currently major obstacles for further commercialization. These negative features are presumably due to the uncontrolled phase impurities, crystal morphology, and inefficient charge transport in the integrated devices rather than to

intrinsic $CsPbBr_3$ material properties. The most difficult hurdle is the formation of the Cs-rich 0D impurity phase of Cs_4PbBr_6 or the Pb-rich 2D impurity phase of $CsPb_2Br_5$, which substantially deteriorate the optoelectronic properties.[31–33] Electronic band structure calculations indicate a high defect tolerance of $CsPbBr_3$ due to the lack of bonding-antibonding interaction between the conduction and valence bands (Scheme 1b).[8] The prominent defect formation energy under a Br-rich growth condition (e.g., in excess of HBr) is much lower than that under a Br-poor growth condition (e.g., in a polar solvent with a low Br molar ratio). Hence, a Br-rich condition will suppress the defect concentration.[8] In recent years, the synthesis of a wide range of phase- and morphology-tuned $CsPbBr_3$ from the nanoscale to the bulk scale has been optimized for high-gain photodetector applications. The most prominent fabrication procedures are illustrated in Figure 1.

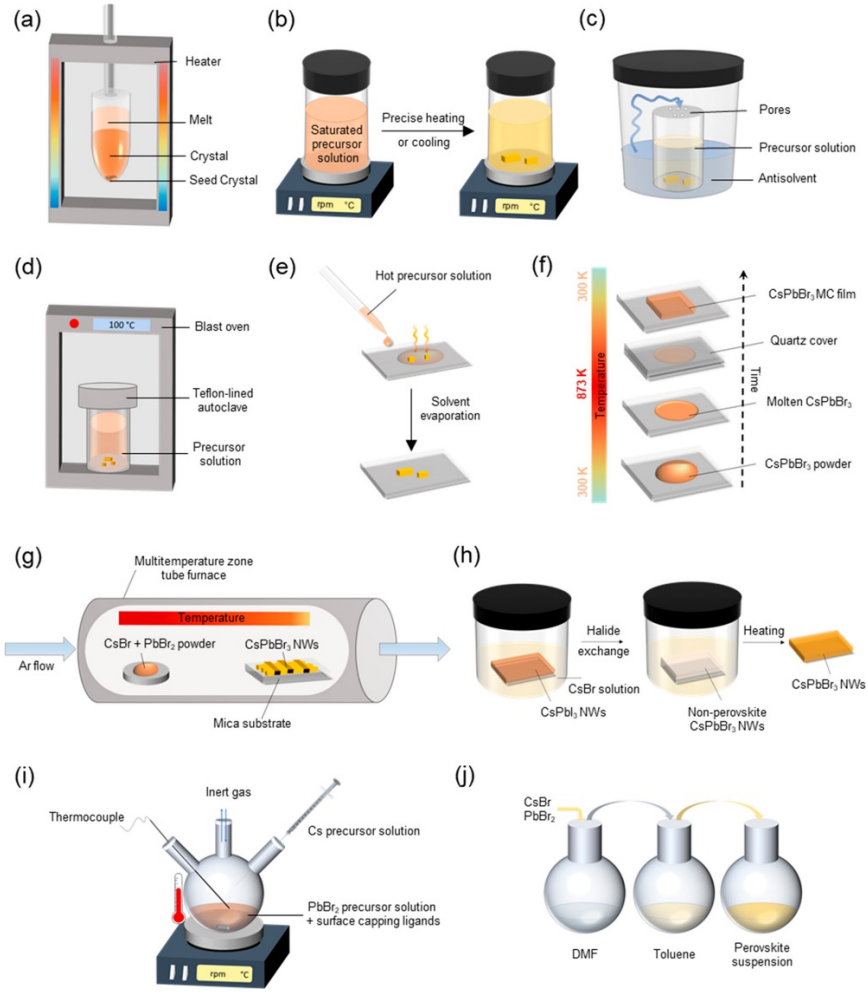

Figure 1. Fabrication procedures for $CsPbBr_3$ single crystals (SCs), microcrystals (MCs), nanowires (NWs), nanocrystals (NCs) and thin films. (a) Bridgman technique (BT) - SCs, (b) inverse temperature crystallization (ITC) and controlled cooling of a saturated solution - SCs and MCs, (c) antisolvent-assisted vapor crystallization (AVC) - SCs and MCs, (d) solvothermal method - NWs, (e) low-temperature solvothermal synthesis - MCs and NWs, (f) hot-pressed synthesis - MCs, (g) vapor-based methods - MCs and NWs, (h) solution synthesis and halide exchange - NWs, (i) hot injection - NCs and (j) ligand-assisted reprecipitation - NCs.

In this review, we provide a comprehensive overview of the recent progress in the synthesis strategies for $CsPbBr_3$ materials - thin films, nanocrystals (NCs), microcrystals (MCs), and single crystals (SCs) - for application in low- and high-energy photodetectors. More specifically, we focus on the critical synthesis parameters that govern the crystalline purity, material stability, and efficient in-device performance. A prominent example of these parameters is the stoichiometric molar ratio of Cs to Pb in the initial precursor mixture since it is crucial for the resulting crystal phase purity by minimizing Cs_4PbBr_6 and $CsPb_2Br_5$ detrimental side product formation. Furthermore, diverse device architectures that strongly affect the performance (i.e., the particular choice of interfacial layers or setup, Figure 2) are discussed with a focus on improving the photodetector performance metrics by reducing the leakage current. For a detailed description of the specific photodetector characteristics, e.g., responsivity (R), detectivity (D*), external quantum efficiency (EQE), linear dynamic range and response speed, we direct the readers to recent reviews by Wang *et al.* and Song *et al*.[34,35] A summary of the critical parameters and the corresponding device performance of the $CsPbBr_3$ compounds and composites discussed in this review can be found in Tables 1-6.

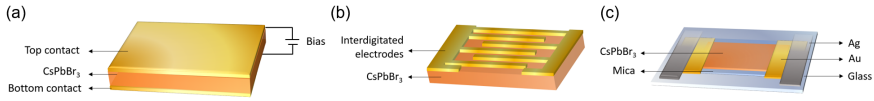

Figure 2. Schematics of a (a) radiation detector based on $CsPbBr_3$ SCs with top-bottom metal electrodes, (b) photodetector based on $CsPbBr_3$ MCs or NCs with interdigitated electrodes on top, and (c) $CsPbBr_3$ nano/microwire-based photodetector with metal electrodes deposited on both sides.

1.2 Single Crystals

The ability to synthesize high-quality SCs is of utmost importance for the evaluation of the fundamental properties of materials and in-depth investigations towards device prototyping. SCs lack grain boundaries and pinholes and contain a relatively low defect concentration (10^9-10^{10} cm^{-3}) compared to their smaller counterparts, e.g., MCs, NCs and polycrystalline thin films.[36] In addition to the recent progress made in the synthesis procedures for $CsPbBr_3$ SCs, the properties in the framework of IR and visible light to X-ray, γ-ray and α-particle detection are highlighted (Figure 3). Two major classes of synthetic approaches have been utilized for the synthesis of SCs, namely, solid-state and solution-based methods (examples of SCs for each technique are depicted in Figure 4).

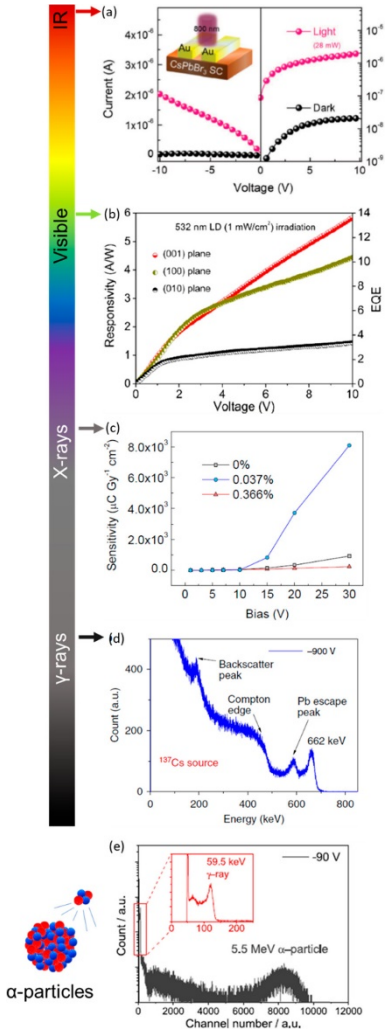

Figure 3. Schematic representation of the wide range of low- to high-energy radiation detection with $CsPbBr_3$ SC devices. Examples ranging from IR light to γ-rays and even α-particles have been reported. The graphs depict the response of $CsPbBr_3$ SCs to (a) IR light, (b) visible light, (c) X-rays, (d) γ-rays, and (e) α-particles. Reprinted with permission from (a) ref. 37, copyright 2017, Wiley-VCH Verlag GmbH & Co. KGaA, Weinheim; (b) ref. 9, copyright 2018, American Chemical Society; (c) ref. 38, copyright 2020, American Chemical Society; (d) ref. 27, copyright 2018, Springer Nature Limited; and (e) ref. 39, copyright 2019, Elsevier.

In a seminal paper, Stoumpos *et al*. reported the possibility of using solid-state synthesis to generate $CsPbBr_3$ SCs, which were further used for high-energy radiation detection.[28] Their synthesis involved the Bridgman technique (BT), which is a melt crystallization method (Figure 1a). Generally, an ampoule (e.g., fused silica or quartz tube) is loaded with a finely powdered $CsPbBr_3$ precursor, after which it is put under vacuum and flame sealed. Afterwards, the ampoule is slowly lowered into a vertical tube furnace with a temperature gradient, leading to $CsPbBr_3$ as a monocrystalline ingot. In this technique, a stoichiometric ratio of high-purity reagents is needed. Moreover, the temperature gradient, as well as the translation speed, need to be finely tuned to obtain a high-quality SC ingot. Finally, the ingot is cut and polished for further analysis and implementation in devices.[28,40,41,27,37,9,39] Stoumpos *et al*.[28] reported that the $CsPbBr_3$ precursor required to fill the ampoule can be prepared by reacting CsBr and $PbBr_2$ at 600 °C or by mixing both precursor salts in an aqueous hydrobromic acid (HBr) solution at RT. From this BT process, an orthorhombic-phase SC ingot of several cm^3 was obtained. A slice of the SC exhibited a 2.5 μs electron relaxation time, which, considering the estimated mobility-lifetime product (μτ) of 1.7×10^{-3} cm^2 V^{-1}, led to an electron mobility as high as 1000 cm^2 V^{-1} s^{-1}. The K_α and K_β peaks of an unfiltered Ag radiation source (λ = 0.5742 Å, 21.59 keV) could even be resolved using a 2.1 mm thick ingot slice between silver contacts.[28] Recently, He *et al*. demonstrated that the high-energy radiation detection range can be extended to γ-rays[27] and even α-particles.[39] A high-purity SC ingot slice was introduced into a Ga/$CsPbBr_3$/Au device configuration for high spectral resolution detection of the 59.5 (^{241}Am γ-ray), 122 and 136 (^{57}Co γ-ray), 511 (^{22}Na γ-ray), and 662 (^{137}Cs γ ray) keV lines (Figure 3d). This impressive result was achieved due to the highly suppressed dark current of the corresponding device. Due to the low work function of the Ga metal contact, a high Schottky barrier was formed under reverse bias, leading to a -10 nA dark current (at 2000 V cm^{-1} bias). Notably, the very long hole lifetime exceeding 25 μs and related μτ of 1.34×10^{-3} cm^2 V^{-1} contributed to the reported high spectral resolution. μτ corresponds to the length charge carriers can travel. The higher this parameter, the higher the charge collection efficiency per specific area will be, hence increasing the detector resolution.[42] Moreover, detection was stable for more than 120 h of continuous operation. In a subsequent report, He *et al*. applied the same procedure to generate an In/$CsPbBr_3$/Au detector capable of resolving the α-particle spectrum (5.5 MeV) and γ-rays (59.5 keV) from a ^{241}Am radiation source (Figure 3e).[39] In 2017, Song *et al.* synthesized high-quality $CsPbBr_3$ SCs via the BT method for low-energy (IR and visible) photon detection.[37] With interdigitated Au

electrodes on a $CsPbBr_3$ SC, they achieved on/off ratios of 1000 and 500 under 532 and 800 nm excitation, respectively. The R value reached 2 AW^{-1} under 535 nm excitation (at a 5 V bias) and 1.4×10^{-3} AW^{-1} for IR excitation, and relatively fast rise and decay times in the µs range were measured for both radiation ranges (Figure 3a). Later, Zhang *et al*. made a $CsPbBr_3$ SC ingot of 40 cm^3.[9] They implemented Au interdigitated electrodes on the SC, generating a device exhibiting a 10^3 on/off ratio, an R of 5.83 AW^{-1} and a D* of 2.5×10^{12} Jones under 532 nm excitation and a 10 V bias (Figure 3b).

Solution-based techniques, such as antisolvent-assisted vapor crystallization (AVC) and inverse temperature crystallization (ITC), are routinely used to grow hybrid organic-inorganic MHP SCs. Unfortunately, for all-inorganic Cs-based perovskites, multiple impurities readily form in solution due to a mismatch of the precursor stoichiometry and the different solubilities in each solvent. Until 2016, the successful application of these techniques for the fabrication of $CsPbBr_3$ SCs was not developed.[43,44] The success largely depends on the precursor purity, stoichiometry, (anti and co)solvent selection and crystallization temperature. In contrast to the BT method, these solution-based techniques employ relatively low temperatures. In the AVC technique, an open vial containing the precursor solution is placed within a container filled with antisolvent (Figure 1c). The slow diffusion of the antisolvent into the precursor solution gradually reduces the solubility of the precursor and promotes crystallization over a few days, leading to the formation of mm-sized, cuboid to rectangular-shaped, orange SCs. Rakita *et al*. applied the AVC method to obtain $CsPbBr_3$ SCs.[43] First, equimolar CsBr and $PbBr_2$ are dissolved in dimethylsulfoxide (DMSO). Next, this solution is saturated by the dropwise addition of methanol (MeOH) or acetonitrile (MeCN). Next, this solution is stirred for one day, yielding a strongly fluorescent green-yellow impure Cs_4PbBr_6 precipitate. After filtration, a vial with the supernatant is placed inside a container filled with the same antisolvent as in the saturation step (either MeOH or MeCN) obtaining, mm-sized rectangular prisms (MeCN) or terrace-shaped crystals (MeOH) in the saturated solution. XRD analysis showed the usual orthorhombic phase, while impedance spectroscopy revealed a substantially lower resistivity in the dark (0.1 GΩ cm) compared to the SCs obtained from the BT technique (1 to 343 GΩ cm), which might lead to a higher dark current when implemented in a device.[28] Cha *et al*. fabricated a photodetector based on a $CsPbBr_3$ SC prepared via AVC with thermally deposited Au electrodes.[45] Their device showed an on/off ratio of 460 (6 V bias), a responsivity of 2.1 A W^{-1} and approximately 0.3 s and 5 s rise and decay times, respectively. Different

from Rakita *et al*.,[43] Cha *et al*. dissolved CsBr and $PbBr_2$ with a molar ratio of 1 to 2.5 in DMSO, and dichloromethane (DCM) was used as the antisolvent, obtaining mm-sized $CsPbBr_3$ SCs as well. Additionally, in 2017, Ding *et al*. and Zhang *et al*. reported the use of AVC-synthesized $CsPbBr_3$ SCs for photodetection.[46,47] Ding *et al*. used a similar protocol as Rakita *et al*. and obtained mm-sized rectangular prisms with an orthorhombic crystal structure. Their device consisted of a $CsPbBr_3$ SC with sputtered Au electrodes (5 V bias), exhibiting a 28 mA W^{-1} R, a 7% EQE and a 1.8×10^{11} Jones D*. Rise and decay times on a timescale below 100 ms were achieved, resulting in the fastest values among AVC-prepared SCs. To stress the importance of the precursor molar ratio in AVC, Zhang *et al*. demonstrated the formation of multiple side phases in a series of experiments by systematically varying the molar equivalent of $PbBr_2$ to CsBr. At a 1.5 ratio, the side phase formation was limited, and the crystals were larger, leading to the largest $CsPbBr_3$ SC ($42 \times 5 \times 3$ mm^3) obtained from solution-based methods. Moreover, the crystal size can be effectively increased by reducing the growth speed by lowering the antisolvent vapor pressure. The resulting orthorhombic crystals, when embedded in a Au/$CsPbBr_3$/Au device, achieved an on/off ratio as high as 100 under a 1 V bias and blue LED (365−420 nm, 1 mW cm^{-2}) excitation. Notably, the reported hole mobility (143 $cm^2 V^{-1} s^{-1}$) and resistivity (2.1 GΩ cm) are among the best reported values for solution-processed $CsPbBr_3$ SCs. In 2018, Yang *et al*. proposed a space-limited version of the standard AVC method (SLAVC) to fabricate large $CsPbBr_3$ monocrystalline films.[48] They dropped 50 µL of precursor solution (DMSO, 1:1 CsBr/$PbBr_2$ ratio) on a hydrophilic substrate, which was clipped onto a hydrophobic substrate. The system was placed in a container with MeCN as the antisolvent, which led to a mm-sized orthorhombic film without grain boundaries. The thickness of the film could be varied by changing the clipping pressure. After depositing interdigitated Au electrodes, they achieved a very low dark current of 7 pA, an on/off ratio > 10^3 (2 V bias), rise and decay times of 0.4 and 9 ms, an R of 2.5 A W^{-1}, an EQE of 6.2 and a D* of 1.4×10^{13} $Hz^{0.5}$ cm W^{-1}. Moreover, the film showed very high hole and electron mobilities of 1770 and 910 $cm^2 V^{-1} s^{-1}$. The device demonstrated stability after seven days of continuous irradiation at 90% relative humidity and 150 °C.

In addition to establishing the AVC protocol, Rakita *et al*. reported $CsPbBr_3$ SC growth from ITC (Figure 1b).[43] The ITC method relies on the retrograde solubility phenomenon typical for lead halide perovskites. Similarly, MeOH and MeCN saturated precursor solutions undergo two heating cycles. After

the first cycle, an orange precipitate is formed and redissolves after cooling, leaving a mixture of Cs_4PbBr_6 and other impure byproducts. The filtered solution is then gradually reheated. The precipitation temperature varies for different antisolvents, as it was found to be 40 °C for MeOH and 120 °C for MeCN. In contrast, Dirin *et al*. reported that fast nucleation and hence multiple nuclei formation can be avoided by using a 1:2 CsBr:$PbBr_2$ molar ratio in a solution of DMSO with cyclohexanol and N,N-dimethylformamide (DMF).[44] At 90 °C, the nuclei started to form, and further heating to 110 °C induced corresponding crystal growth. Both groups obtained orthorhombic-phase mm-sized SCs. Dirin *et al*. reported a competitive SC resistivity of 2 GΩ and a photodetector R of 6 A W^{-1} (10 V bias).[44] The possible use of $CsPbBr_3$ SCs as a γ-ray detector was demonstrated by irradiating a Ag/$CsPbBr_3$/Ag device with a ^{241}Am source. In a later report from Saidaminov *et al*., a 1:2 CsBr/$PbBr_2$ molar ratio was also applied, but this time, the solution at 100 °C was filtered to remove the $CsPb_2Br_5$ impurity phase.[49] Upon further heating to 120 °C for 3 h, 3 × 2 × 1 mm^3 orthorhombic SCs were generated. The corresponding Au/$CsPbBr_3$/Pt device showed a very high on/off ratio of 10^5 at a 0 V bias due to the remarkably low dark current of 10 pA. Furthermore, a 1.7 × 10^{11} Jones D* and a 6% EQE with a 28 mA W^{-1} peak R (at 550 nm excitation) were obtained. The rise and decay times were 230 and 60 ms, respectively. Finally, through the addition of RbBr at a 1% molar ratio in solution, Li *et al*. obtained a 0.037% Rb-doped (CsRb)$PbBr_3$ SC. Rb doping can lead to a highly enhanced X-ray sensitivity of 8097 μC Gy_{air}^{-1} cm^{-2} (compared to 918 μC Gy_{air}^{-1} cm^{-2} for the pure MHP) (Figure 3c).[38] The increased performance was attributed to a positive change in the electron and hole effective masses due to the increased orbital overlap between Pb and Br atomic orbitals induced by the presence of trace Rb. Besides doping and improving the synthesis procedure, an efficient method to improve X-ray sensitivity is by electrode contact engineering in the SC device. This has for example been demonstrated by He *et al.* for γ-rays detection,[27] and extended to X-rays by Zhang *et al*. and Xu *et al*.[50,51] Zhang *et al*. have shown that an Al/$CsPbBr_3$/Au SC-based device, obtained from a modified low-temperature ITC method, can achieve a 1256 μC Gy^{-1} cm^{-2} sensitivity under 40 V. The high sensitivity arises from a constant low dark-current and suppressed ionic migration thanks to the high Schottky barrier at positive bias due to the lower work function of Al. Moreover, their modified ITC method resulted in a high quality SCs with a resistivity (7.85 GΩ cm) and charge carrier mobility (1368 cm^2 V^{-1} s^{-1} for electrons, and 2652 cm^2 V^{-1} s^{-1} for holes), which is even higher than their previous report on the AVC method.[47] Later, also Xu *et al*. have been able to achieve 2860 μC Gy^{-1} cm^{-2} X-rays sensitivity at -10 V by

contact engineering. These results further confirm the viability of contact engineering as an important optimization approach. In this case the Schottky barrier between the Ag (low work function) contact and the $CsPbBr_3$ SCs in the Ag/$CsPbBr_3$/ITO device was also responsible for the high sensitivity due to a decrease in the leakage current.

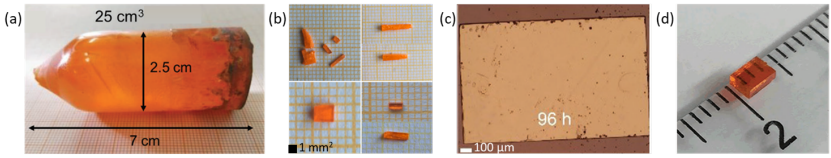

Figure 4. Examples of SCs synthesized by (a) the BT, (b) AVC, (c) space-limited AVC (optical image of a $CsPbBr_3$ monocrystalline thin film with a 100 µm scale bar) and (d) ITC. Reprinted with permission from (a) ref. 37, copyright 2017, Wiley-VCH Verlag GmbH & Co. KGaA, Weinheim; (b) ref. 46, copyright 2017, American Chemical Society; (c) ref. 48, copyright 2018, Wiley-VCH Verlag GmbH & Co. KGaA, Weinheim; and (d) ref. 49, copyright 2017, Wiley-VCH Verlag GmbH & Co. KGaA, Weinheim.

Summarizing, an accurate comparison between different techniques is not straightforward due to the high diversity in the reported experimental conditions and setups. However, even though high temperatures and high-purity reagents are needed, the BT method[28,40,41,27,37,9,39] appears to result in the best quality SCs with a high resistivity, high electron and hole mobilities, low trap densities, charge carrier lifetimes up to 25 µs and a corresponding high µτ product. These promising features are reflected in their corresponding photodetectors, which show on/off ratios as high as 10^3 - due to the extremely low dark current (nA range) and high photocurrent (mA range) - and response times in the µs range. Note that the intrinsic physical properties of the solution-prepared crystals only slightly fall behind while offering a more rapid and feasible method to synthesize $CsPbBr_3$ SCs. For each type of device architecture, comparable detector performances are obtained. For instance, on/off ratios between 10^2 and 10^5 and a photodetectivity as high as 10^{11} Jones have been reported[33-39] for visible wavelengths, while a sensitivity as high as 8097 µC Gy_{air}^{-1} cm^{-2} has been demonstrated for X-ray radiation.[38]

Possible improvements in this field could be achieved through screening the effects of different dopants, aside Rb, to enhance the photodetection properties of $CsPbBr_3$ SCs. Moreover, contact engineering could be extended to low-energy photodetection. Even though SCs could already find their application in e.g., single pixel cameras for both low and high-energy devices, they would certainly benefit from an increase in dimension to cover larger areas. For instance, semiconducting wafers of Si SC ingots of 300 mm diameter are nowadays routinely grown by melt-growth methods for electronic applications.[52] Moreover, the importance of large area SCs can be stressed by the fact that commercially available FPDs, normally used for X-ray computed tomography scans in medicine, require detector areas up to 45 x 45 cm^2, which is very challenging to achieve with the synthetic techniques reported so far for SCs.

Overall, the application potential of highly crystalline SCs in devices with impressive optoelectronic properties has been demonstrated. Furthermore, an interesting outlook on their use for polarization sensitive detection have recently been reported by Yang *et al*. and Fu *et al*.[53,54] Yang *et al*. substituted the Cs cation with diamines for application in polarization-sensitive photodetection.[53] By applying solution-based synthesis (Figure 1b), they were able to form 2D Dion-Jacobson-type perovskites described by the chemical formula $(HDA)CsPb_2Br_7$ (HDA = 1,6-hexamethylenediamine). The reduced dimensionality resulted in an optical absorption anisotropy ratio of 2.2 (α_c/α_b) and a dichroism ratio of 1.6 (I_{ph}^c/I_{ph}^b) along two different crystallographic axes. A D* as high as 10^9 Jones and rise and decay times of hundreds of µs were found under 405 nm light irradiation. Likewise, Fu *et al*. alloyed $CsPbBr_3$ with 2-methyl-1,5-diaminopentane ($2meptH_2$), obtaining a $(2meptH_2)CsPb_2Br_7$ perovskite composition.[54] Similar to the results of Yang *et al*., this perovskite showed an on/off ratio of 10^3, a D* as high as 10^9 Jones and rise and decay times in the hundreds of µs range under UV irradiation. Both diamine-substituted compounds exhibited good stability after being stored for several days in ambient conditions, with almost no changes in their structure and performance.

Table 1. Summary of critical parameters and the corresponding device performance of $CsPbBr_3$ single crystals in the UV-Vis-IR range.

Material (device structure)	Preparation method	Responsivity (light source, intensity, bias)	Detectivity (light source, intensity, bias)	Response speed rise/decay time (light source, intensity, bias)	on/off ratio (dark/photo-current)	External quantum efficiency	Reference
$CsPbBr_3$ ($Au/CsPbBr_3/Au$)	Brigdman technique	2 A W^{-1} (535 nm, 5 V)	--	69/261 µs (532 nm)	> 1000 (2.9 nA/6.8 µA) (532 nm, 0.31 mW, 2 V)	460 % (535 nm, 5 V)	37
		1.4 x 10^{-3} A W^{-1} (two photon IR, 106 mW)	--	111/575 µs	500 (16 nA/9.1 µA) (800 nm, 80 mW, 5 V)	--	
$CsPbBr_3$ ($Au/CsPbBr_3/Au$)	Brigdman technique	5.83 A W^{-1} (532 nm, 1 mW cm^{-2}, 10 V)	2.5 x 10^{12} Jones (532 nm, 1 mW cm^{-2}, 10 V)	--	> 1000 (2 V) (1.84 µA/2.73 mA) (532 nm, 16.5 mW cm^{-2}, 10 V)	1360% (532 nm, 1 mW cm^{-2}, 10 V)	9
$CsPbBr_3$ ($Au/CsPbBr_3/Au$)	AVC	2.1 A W^{-1} (520 nm, 1 µW)	--	0.3/5 s (520 nm, 10 µW)	460 (520 nm, 500 µW, 6 V)	--	45
$CsPbBr_3$ ($Au/CsPbBr_3/Au$)	AVC	0.028 A W^{-1} (450 nm, 1 mW, 5 V)	1.8 x 10^{11} Jones (450 nm, 1 mW, 5 V)	< 100 ms (462 nm)	100 (462 nm, 5 V)	7.00% (450 nm, 1 mW, 5 V)	46
$CsPbBr_3$ ($Au/CsPbBr_3/Au$)	AVC	--	--	--	100 (365-420 nm, 1 mW cm^{-2}, 1 V)	--	47
$CsPbBr_3$ ($Au/CsPbBr_3/Au$)	SLAVC	2.5 A W^{-1}	1.4 x 10^{13} cm $Hz^{0.5}$ W^{-1}	0.4/9 ms	> 1000 7 pA/97 nA (530 nm, 216 µW cm^{-2}, 2 V)	6.2	48
$CsPbBr_3$ (Ag paste/$CsPbBr_3$/Ag paste)	ITC	6 A W^{-1}	--	--	--	--	44
$CsPbBr_3$ ($Pt/CsPbBr_3/Au$)	ITC	28 x 10^{-3} A W^{-1} (550 nm)	1.7 x 10^{11} Jones	230/60 ms	10^5 (10 pA/1 µA) (white light, 10 mW cm^{-2}, 0 V)	6% (550 nm)	49
$(HDA)CsPb_2Br_7$ (Carbon/$(HDA)CsPb_2Br_7$/ Carbon)	Controlled Cooling	0.21 x 10^{-3} A W^{-1} (405 nm, 90° polaized light illumination)	1.5 10^9 Jones (405 nm)	200/300 µs	(23.4 pA/246 pA) (405 nm, 3 mW cm^{-2}, 10 V)	--	53
$(2meptH_2)CsPb_2Br_7$ (Ag/$(2meptH_2)CsPb_2Br_7$/Ag)	Controlled Cooling	0.1 A W^{-1}	10^8 Jones	232/150 µs	> 1000 (17 pA/15 nA) (266 nm, 37.5 mW cm^{-2}, 10 V)	40%	54

Table 2. Summary of critical parameters and the corresponding device performance of $CsPbBr_3$ single crystals for X-, γ-rays and α particles.

Material (device structure)	Preparation method	Sensitivity/Energy resolution	Detection limit	Response speed rise/decay time (light source, intensity, bias)	on/off ratio (dark/photo-current)	Reference
$CsPbBr_3$ (Au/$CsPbBr_3$/Au)	ITC	918 μC Gy_{air}^{-1} cm^{-2} (Au anode, 30 V)	--	--	-- --/1.33 nA (Au anode 50 kV, 5.499 mGy s^{-1}, 1 V)	38
$Cs_{0.963}Rb_{0.037}PbBr_3$ (Au/$Cs_{0.963}Rb_{0.037}PbBr_3$/Au)		8097 μC Gy_{air}^{-1} cm^{-2} (Au anode, 30 V)	--	--	-- --/2.56 nA (Au anode 50 kV, 5.499 mGy s^{-1}, 1 V)	
$CsPbBr_3$ (Al/$CsPbBr_3$/Au)	ITC	1256 μC Gy_{air}^{-1} cm^{-2} (80 kVp, 20 Vmm^{-1}, 40 V)	--	--	<100 3/-- nA (420 nm, 1 mW, 50 V)	50
$CsPbBr_3$ (Ag/$CsPbBr_3$/ITO)	ITC	2860 μC Gy_{air}^{-1} cm^{-2} (Ag 45 keV, 333.69 μGy s^{-1}, -10 V)	--	--	-- 5−27/-- nA cm^{-2} (8 V)	51
$CsPbBr_3$ (Ga/$CsPbBr_3$/Au)	Bridgman Technique	3.9% (122 keV ^{57}Co)	--	--	-- -10 nA/-- (-200 V)	27
$CsPbBr_3$ (In/$CsPbBr_3$/Au)	Bridgman Technique	15% (5.5 MeV α particle)	--	--	-- 100 nA cm^{-2}/-- (- 100 V)	39

1.3 Microcrystals

Recently, $CsPbBr_3$ MCs have gained major attention, particularly towards directed linear carrier transport.[55] MC-based photodetectors aim for a sizeable lateral area with a low thickness for more efficient collection of photogenerated charge carriers, which can ultimately lead to more efficient large area photo- or flat panel detectors (FPD).[10] The preparation strategies for $CsPbBr_3$ MCs mainly consist of solution techniques: ITC, low-temperature solvothermal synthesis and antisolvent precipitation methods (Figures 1b-c, e), each allowing tunable optoelectronic characteristics. Additionally, a few examples of vapor-phase (VP) synthesis and hot-pressed methods (Figures 1f-g) are discussed. $CsPbBr_3$ MCs are found to adopt mainly the orthorhombic but also cubic[56,57] and monoclinic[58] phases, depending on the reaction parameters.

Yang *et al.* reported the synthesis of $CsPbBr_3$ MCs by applying a modified ITC procedure.[59] In this method, CsBr and $PbBr_2$ in a 1:2 molar ratio are dissolved in DMSO, after which the solution is cooled to RT, filtered, diluted, and the antisolvent toluene is added dropwise until saturation. By gradually heating the mixture under constant stirring, an interconnected MC layer forms. Cubic-shaped $CsPbBr_3$ MCs with dimensions of 10-50 µm form on a glass substrate after evaporation of the remaining solution. The trap density (n_{trap}) of these crystals was measured by the space-charge-limited current method (SCLC) to be ~4.5×10^{12} cm^{-3}, which is higher than the n_{trap} for SCs but much lower than that of spin-coated thin films. The corresponding photodetector device consisted of a film of $CsPbBr_3$ MCs between two interspaced ITO electrodes and exhibited R, EQE, and D* of 6×10^4 A W^{-1}, 2×10^7% and 10^{13} Jones, respectively.[59] Zhou *et al.* reported a similar synthesis strategy directly on a SnO_2-coated substrate, resulting in an 11 µm thick film of phase-pure orthorhombic MC cubes up to 10 µm in size (Figure 5a) with a similar n_{trap} of 2.8×10^{12} cm^{-3}. The long PL lifetime reached 10 ms, which is three orders of magnitude higher than that of the MCs of Yang *et al.*, suggesting improved carrier transport.[10] The corresponding photodetector device structure was glass/ITO/SnO_2/$CsPbBr_3$/spiro-OMeTAD/Au, with an enhanced D* of 4.8×10^{12} Jones, an on/off ratio of 1.3×10^5 and an R of 0.172 AW^{-1}.

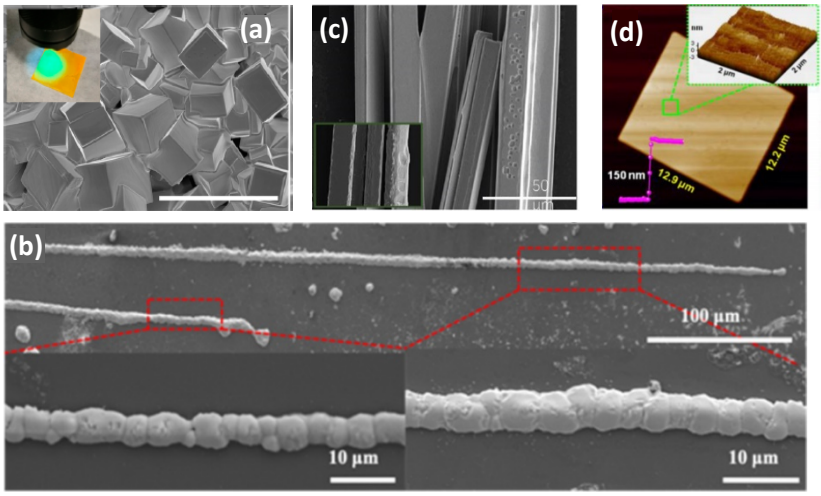

Figure 5. (a) SEM image of a $CsPbBr_3$ MC perovskite film. The scale bar is 50 µm. Inset: digital photograph of the film under 365 nm illumination. (b) SEM image of $CsPbBr_3$ microwires (MWs) with connected grains. (c) SEM image of oriented $CsPbBr_3$ microrods. (d) 2D AFM image of a $CsPbBr_3$ microplatelet. Reprinted with permission from (a) ref. 10, copyright 2018, American Chemical Society; (b) ref. 56, copyright 2020, American Chemical Society; (c) ref. 55, copyright 2019, Royal Society of Chemistry; and (d) ref. 57, copyright 2019, American Chemical Society.

Tong *et al*. modified this ITC strategy to obtain $CsPbBr_3$ microwires (MWs) by controlling the phase transition from $CsPb_2Br_5$. $CsPb_2Br_5$ films were first grown on Si/SiO_2 substrates via vacuum vapor deposition of a powder containing CsBr and $PbBr_2$ in a 1:2 molar ratio, after which they were converted to $CsPbBr_3$ during post-annealing. The combination of the high-temperature instability of $CsPb_2Br_5$ and volatile nature of $PbBr_2$ promoted the reaction $CsPb_2Br_5 \rightarrow CsPbBr_3 + PbBr_2$. This resulted in ultralong ~ 500 µm cubic-phase MWs composed of connected grains with an average grain size over 5 µm and a height of 1.4 µm (Figure 5b). A photodetector was fabricated by depositing an 80 nm thick Au layer on the top surface of the MWs. Upon illumination at -3 V, this device exhibited comparable results with an R of 6.44 AW^{-1} and a D* of 10^{12} Jones. Furthermore, a high photocurrent of -1 nA and a very low dark current of -60 pA were obtained.[56] Applying low-temperature solvothermal synthesis (Figure 1e), Zheng *et al.* prepared crystals with a micro/nanoflake morphology. This is a very fast and

easy method starting from dissolving CsBr and $PbBr_2$ in a 1:2 molar ratio in DMF. This solution is dropped on a conductive SiO_2 or polyethylene terephthalate (PET) substrate, and the temperature is then gradually lowered, with the DMF slowly evaporating, resulting in a uniform $CsPbBr_3$ film. The corresponding photodetector on flexible PET with Au electrodes exhibited an R of 2.766 AW^{-1} and an EQE as high as 1254%. Furthermore, the dark current and photocurrent at 5 V were 286 pA and 14.7 nA, respectively, resulting in an on/off ratio of 51. Notably, the device also exhibited fast rise and decay times of 40 and 20 ms with high stability and reproducibility (Figure 6a,b).[60]

$CsPbBr_3$ microrods were obtained by placing a porous membrane filled with a precursor solution of stoichiometric CsBr and $PbBr_2$ in DMSO at 40 °C in a hermetically closed space (Figure 1c). This space was then filled with MeOH at 60 °C as an antisolvent.[55] As a result, 1000-2000 µm × 3-20 µm × 0.8 µm rectangular orthorhombic microrods were grown (Figure 5c). A photodetector was prepared by depositing Au electrodes using a metal mask on single $CsPbBr_3$ microrods. The resulting device exhibited promising properties, such as a low dark current of 0.2 nA, a D* of 3.67×10^{12} Jones, an R of 0.025 AW^{-1} and an EQE of 7.68%.[55] As a similar strategy, MWs with a length of 50 µm and a diameter of 2 µm were grown by Gui *et al*. by using an easy and fast two-step solution process.[61] In this process, PbI_2 MWs were first grown by dissolving PbI_2 in DMF, adding water and leaving the solution overnight. Next, PbI_2 wires were spun on a Si/SiO_2 substrate with prepatterned ITO electrodes with a 10 µm spacing and dipped into a CsBr solution in methanol for 1 h. Upon excitation, the resulting photodetector achieved a spectacularly low dark current in the range of 40 pA at a bias of 5 V. In addition, the authors also measured an R of 118 AW^{-1}, an EQE of 1×10^4% and a D* of 8×10^{12} Jones, which are very promising parameters for integration into large-scale photodetectors.[61] Finally, Li *et al*. applied an easy vapor-based synthesis method to fabricate microplatelets with lateral dimensions of 7-15 µm and thicknesses of approximately 150 nm (Figure 5d).[57] In this method, a 1:2 molar ratio CsBr and $PbBr_2$ mixture is heated at 580 °C in the first zone of a double temperature zone tube furnace. Ar carrier gas is used to transport the volatile components to the second temperature zone, which is kept at 360 °C so that $CsPbBr_3$ microplatelets start to grow on a SiO_2/Si substrate. A photodetector was fabricated by dispersing the cubic phase microplatelets in toluene and then dropcasting them onto a SiO_2/Si substrate with Au patterned fingers. This photodetector

exhibited a low dark current of 17 pA, an R of 1.33 AW^{-1} and a D* of 0.86×10^{12} Jones, comparable to previously described works.

Gu *et al*. modified the VP growth strategy by introducing perovskite seeds onto a silicon substrate.[62] A dilute (0.05 M) 2:1 CsBr/$PbBr_2$ precursor solution was printed in a controlled pattern using inkjet printing, after which the seeded substrate was brought into a chemical vapor deposition system to ripen.[63] This resulted in precise control of the location, size and growth of uniform $CsPbBr_3$ microplates. The phase-pure plates exhibited a low trap density of 2.1 x 10^{12} cm^{-3} and a relatively long carrier lifetime of up to 101 ns. The corresponding photodetector was fabricated by depositing Au electrodes on an individual $CsPbBr_3$ microplate grown on quartz glass. The photodetector exhibited a low dark current of 1.6 nA, an R of 480 AW^{-1} and a D* of 2 x 10^{11} Jones when illuminated by a 450 nm laser.

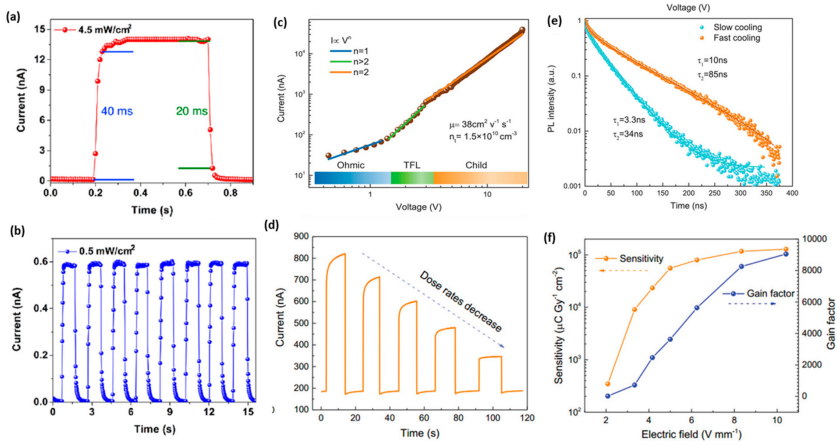

Figure 6. Device properties of an MC-based (a-b) photodetector and (c-f) X-ray detector. (a) Time-dependent photocurrent, where the rise time is 40 ms and the decay time is 20 ms. (b) Time-dependent response of the device, confirming good stability and repeatability. (c) Current-voltage curve of a $CsPbBr_3$ film. (d) Device responses under different X-ray dose rates with an applied electric field of 4.2 V mm^{-1}. (e) Time-dependent photoluminescence. (f) Sensitivity and gain factor as functions of the electric field. Reprinted with permission from (a, b) ref. 60, copyright 2018, American Chemical Society and (c-f) ref. 64, copyright 2019, Wiley-VCH.

Pressure control has a significant influence on the crystal quality, as demonstrated by Pan *et al.* and Zhou *et al.*, who presented a hot-pressed $CsPbBr_3$ film and a pressure-assisted annealing (PAA) strategy, respectively.[64,65] According to Zhou *et al.*, PAA can significantly reduce the void density and surface roughness. This results in a lowered trap density of approximately 8×10^{11} cm^{-3}, with exponentially decreased dark current and exponentially increased photocurrent.[65] Furthermore, properties relevant to photodetectors, such as R and D* of 0.206 AW^{-1} and 7.23×10^{12} Jones, respectively, were obtained. The hot-pressed films of Pan *et al*. were prepared by a four-step process (Figure 1f).[64] $CsPbBr_3$ powder, synthesized by sintering a 1:1 mixture of CsBr and $PbBr_2$, is placed on an FTO glass substrate and heated to the molten state. This is then covered with a preheated quartz plate, followed by lowering the temperature, leading to a 240 µm thick quasi-monocrystalline MC film with a fixed orientation and without grain boundaries. The carrier mobility of these compact films is comparable to that of SCs, with a value of 38 cm^2 V^{-1} s^{-1} and a µτ of 1.32×10^{-2} cm^2 V^{-1}. However, the film has a trap density of 1.5×10^{10} cm^{-3}, which is still slightly higher than that of SCs. The $CsPbBr_3$ MCs were applied in an FTO/$CsPbBr_3$/Au X-ray detector structure with auspicious properties, such as a low dark current of 2.8 x 10^5 nA cm^{-2} and a sensitivity of 55684 µC Gy_{air}^{-1} cm^{-2} at 5 Vmm^{-1}, which is the highest among all the kinds of direct and indirect X-ray detectors reported thus far. Furthermore, it exhibited the lowest detectable dose rate of 215 nGy_{air} s^{-1} at a V_{bias} of 4.2 Vmm^{-1}, which is much lower than the regular dose rate in a medical diagnostic application (5.5 μGy_{air} s^{-1}) (Figure 6c-f).[64] Another X-ray detector prototype was fabricated by Matt *et al.* by using a simple melt process to synthesize 250 µm thick $CsPbBr_3$ films consisting of MCs with sizes between 1 and 10 µm. In this easy process, $CsPbBr_3$ powder is first prepared by solution-based synthesis, after which it is melted directly on a glass/FTO substrate at 575 °C, followed by variable cooling to 560 °C and slow cooling to RT. As a result, a monocrystalline orthorhombic $CsPbBr_3$ MC film forms. A gallium contact was then deposited on top of the perovskite film by brushing, resulting in the lowest detectable dose rate of 500 nGy_{air} s^{-1}, which is two times that reported by Pan *et al.* but still lower than the regular dose rate used in medical diagnostics. The measured sensitivity at a high bias voltage of 300 V is 1450 µC $Gy_{air}^{-1}cm^{-2}$, which approaches the value of the commercial CdZnTe detector and is therefore very promising. However, it is lower than the sensitivity reported by Pan *et al*.[64,66]

In summary, several approaches towards efficient low- and high-energy radiation detectors based on MCs, MWs and even microrods have been developed, each exhibiting prominent features for large-area photodetectors such as a high carrier mobility and fast response time. However, the trap density of MCs remains higher than SCs, leaving room for improvement. Overall, MCs synthesized by the ITC method performed slightly better in photodetection, reaching an R of 6×10^4 AW^{-1}, an EQE of 2×10^7% and a D* of 10^{13} Jones.[59] Furthermore, pressure control is an interesting processing method for realizing more sensitive X-ray detection. The hot-pressed MC films of Pan *et al*. exhibited a very promising sensitivity of 55684 µC Gy_{air}^{-1} cm^{-2}, which is comparable to commercially available detectors and the highest sensitivity reported thus far among all kinds of direct and indirect X-ray detectors.[64,66] This leaves ample opportunities for further development of MC-based flat panel X-ray detectors. Besides the very interesting and promising properties for photo- and X-ray detection, the use of $CsPbBr_3$ MCs can be extended to the UV-Vis range. A new and innovative approach might comprise their use for polarization sensitive detection, similar to what Yang *et al*. and Fu *et al*. have studied for SCs.[53,54]

Table 3. Summary of critical parameters and the corresponding device performance of $CsPbBr_3$ microcrystals.

Material (device structure)	Preparation method	Responsivity (light source, intensity, bias)	Detectivity (light source, intensity, bias)	Response speed rise/decay time (light source, intensity, bias)	on/off ratio (dark/photo-current)	External quantum efficiency	Reference
$CsPbBr_3$ (ITO/$CsPbBr_3$)	SG	6 x 10^4 A W^{-1} (400 nm, 200 nW cm^{-2}, 3 V)	10^{13} Jones (400 nm, 200 nW cm^{-2}, 3 V)	0.5/1.6 ms (400 nm, 200 nW cm^{-2}, 3 V)	--	2 x 10^7 %	59
$CsPbBr_3$ (PET/$CsPbBr_3$/Au)	LPS	2.776 A W^{-1} (275 nm, 5 V)	--	0.04/0.02 s (275 nm, 5 V)	--	1254 %	60
$CsPbBr_3$ (Metal mask/$CsPbBr_3$/Au)	Anti-solvent	0.025 A W^{-1} (405 nm, 0.016 W cm^{-2}, 6V)	3.67 x 10^{12} Jones (405 nm, 0.016 W cm^{-2}, 6 V)	170/160 ms (405 nm, 5 mW)	988 (405 nm, 5 mW, 4 V)	7.68 %	55
$CsPbBr_3$ (Glass/ITO/PEALD-SnO_2/$CsPbBr_3$/PTAA/Au)	PAA	0.206 A W^{-1} (473 nm, 0.64 mW cm^{-2})	7.23 x 10^{12} Jones (473 nm, 0.64 mW cm^{-2})	30/39 µs (473 nm, 0.64 mW cm^{-2})	106	--	65
$CsPbBr_3$ (Glass/ITO/PEALD-SnO_2/ $CsPbBr_3$ /spiro-OMeTAD/Au)	ITC	0.172 A W^{-1} (473 nm, 100 mW, 0 V)	4.8 x 10^{12} Jones (473 nm, 100 mW, 0 V)	0.14/0.12 ms	1.3 x 10^5	--	10
$CsPbBr_3$ (Si/SiO_2/$CsPbBr_3$ /ITO electrodes)	Precipitation	118 A W^{-1} (520 nm, 26.5 µW, 5 V)	8 x 10^{12} Jones (520 nm, 26.5 µW, 5 V)	38/36 ms (520 nm, 26.5 µW, 5 V)	> 2	1 x 10^4 %	61
$CsPbBr_3$ (Au/$CsPbBr_3$/Au)	Vapor	1.33 A W^{-1} (405 nm, 1 µW)	0.86 x 10^{12} Jones (405 nm, 1 µW)	20.9/24.6 ms	4.56 x 10^3	--	57
$CsPbBr_3$ (Si/SiO_2/ $CsPbBr_3$ /Au)	ITC	6.44 A W^{-1} (400 nm, 30 µW cm^{-2},-3 V)	2.88 x 10^{12} Jones (400 nm, 30 µW cm^{-2},-3 V)	301/242 ms (400 nm, 20.06 mW cm^{-2})	(-6.35 x 10^{-11}/-9.66 x 10^{-10} A) (400 nm, 30 µW cm^{-2}, -3 V)	--	56
$CsPbBr_3$ (Quarts/$CsPbBr_3$/Au)	Vapor	480 A W^{-1} (450 nm, 1.8 mW cm^{-2}, 2 V)	2 x 10^{11} Jones (450 nm, 1.8 mW cm^{-2}, 2 V)	--	--	--	62
Material (device structure)	**Preparation method**	**Sensitivity**	**Detection limit**	**Response speed rise/decay time (light source, intensity, bias)**	**on/off ratio (dark/photo-current)**		**Reference**
$CsPbBr_3$ (FTO/$CsPbBr_3$/Au)	Hot-pressed	55684 µCGy_{air}^{-1} cm^{-2} (5 V mm^{-1})	215 nGy_{air} s^{-1}	--	--		64
$CsPbBr_3$ (glass-FTO/$CsPbBr_3$/Gallium)	Melt processing	1450 µCGy_{air}^{-1} cm^{-2} (300 V)	500 nGy_{air} s^{-1}	--	2.2		66

1.4 Nanowires

One-dimensional (1D) MHP nanowires (NWs) can be synthesized with high crystalline quality, exhibiting large surface-to-volume ratios and low trap densities, which generally lead to a direct carrier conduction pathway, long carrier diffusion lengths, reduced carrier recombination rates, and excellent mobilities. These characteristics make NWs very popular in recent developments of ultrasensitive photodetectors.[67–69] To prepare high-quality $CsPbBr_3$ NWs for photodetector applications, various methods have been developed, such as low-temperature solvothermal processes, solution-phase synthesis followed by halide exchange and VP-induced growth of NWs on substrates by the (grapho)epitaxial effect. In this section, protocols involving vapor-liquid-solid (VLS)-induced growth and templated growth by the capillary effect are also illustrated. Note that synthesis of phase pure $CsPbBr_3$ NWs with well-defined uniform morphology and stoichiometry remains a major challenge.

In contrast to conventional hot-injection techniques with fast crystal growth kinetics, Zhai *et al.* applied a 3-day solvothermal method (Cs/Pb = 1.5) to realize the synthesis of $CsPbBr_3$ NWs with ultrahigh aspect ratios exhibiting a diameter of 12 nm and lengths of several mm[12] (Figure 1d, Figure 7a,b). The controlled growth under mild conditions and by effective surface ligand passivation resulted in highly pure cubic-phase $CsPbBr_3$ NWs with a long PL lifetime of 24 ns together with enhanced thermal stability and photostability. The corresponding photodetectors (SiO_2/Si wafers/NWs/Ti-Au electrodes) exhibited a high on/off ratio of 1100 and a very low dark current lower than 1 pA at a V_{bias} of 8 V. After 72 h of illumination, the photocurrent only dropped to 52% of the initial value, indicating reasonable stability. Zeng *et al.* investigated the morphology and performance of $CsPbBr_3$ NW films by combining easy solution-phase synthesis of $CsPbI_3$ NWs with subsequent halide exchange (Figure 1h).[70] Both the conditions for direct growth of $CsPbI_3$ NWs on glass substrates and for their conversion into orthorhombic $CsPbBr_3$ NWs were carefully screened. The optimal metal-semiconductor-metal photodetector consisted of 200 nm x 20 µm sized NWs with a 100 µm interdigitated Au electrode spacing. The device was sensitive in the wavelength range of 300-600 nm with a D* of 1.7×10^{11} Jones, a low dark current of 0.1 nA (V_{bias} = 5 V) and rise and decay times of 10 ms and 22 ms, respectively. Notably, high stabilities under 3 h of UV light illumination and for 200 h at high temperature and humidity were obtained.

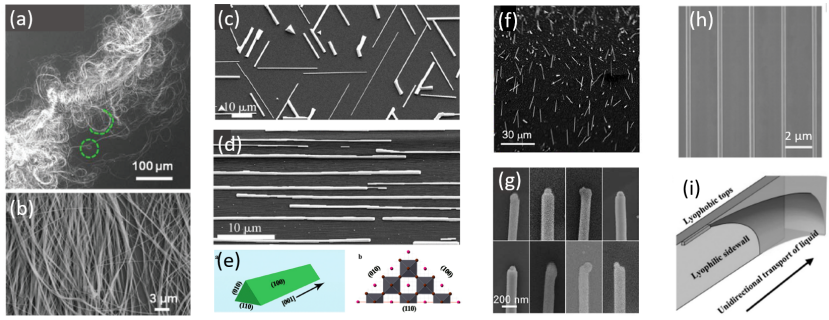

Figure 7. (a) Typical low-magnification SEM image of $CsPbBr_3$ NWs obtained via mild solvothermal synthesis, showing ultrahigh aspect ratios. (b) High-magnification SEM image of the NWs. (c-d) SEM images of $CsPbBr_3$ NWs obtained via (c) epitaxial growth on flat C-plane sapphire and (d) graphoepitaxial growth on faceted M-plane sapphire. (e) Illustration of the triangular morphology of the $CsPbBr_3$-guided NWs and their crystal structure. (f) SEM image of the vertical $CsPbBr_3$ NWs grown on a SiO_2/Si substrate by applying Sn catalysts. (g) Tilted SEM images of individual $CsPbBr_3$ NWs displaying the Sn catalytic seeds. (h) SEM image of crystallographically aligned NWs obtained by capillary trailing confined between lyophobic tops and lyophilic sidewalls in a micropillar-structured template. (i) Schematic of single capillary trailing. Reprinted with permission from (a, b) ref. 12, copyright 2018, Royal Society of Chemistry; (c-e) ref. 71, copyright 2018, American Chemical Society; (f, g) ref. 72, copyright 2019, American Chemical Society; and (h, i) ref. 73, copyright 2017, Wiley-VCH Verlag GmbH & Co. KGaA, Weinheim.

In general, solution-grown $CsPbBr_3$ NWs tend to have no specific crystallographic orientation or alignment, often resulting in unwanted nanostructure morphologies, such as nanoplates and NCs. Furthermore, transfer of NWs is required for physical characterization and device fabrication. VP deposition (Figure 1g) is generally applied to prepare high-quality electronic materials and may offer an alternative method for the growth of planar arrays of $CsPbX_3$ NWs with controlled morphology and orientation for direct integration into high-quality perovskite optoelectronic devices. $CsPbX_3$ NWs tend to grow randomly on an amorphous substrate, as in the case of a Si/SiO_2 substrate,[74] and along specific directions that are

imposed by the substrate surface (epitaxy) or the morphology (graphoepitaxy), as for mica[75–77] or sapphire.[71,78]

Horizontal $CsPbX_3$ (X = Cl, Br, I) NWs and MWs with controlled crystallographic orientation were grown on transparent mica substrates as straightforward platforms for optoelectronic devices by VP epitaxial growth.[76] A 1:1 precursor mixture of CsBr and $PbBr_2$ was heated in the middle of a three-zone furnace at 325 °C at reduced pressure. After two hours, monocrystalline cubic wires ~1 µm in width with a length of tens of µm were obtained. SEM imaging indicated wires with a triangular cross-section grown along the [001] direction and with the low-energy (100) facets exposed. This is in clear contrast to the rectangular cross-section typically observed in solution-grown perovskite NWs. The $CsPbBr_3$ NW photodetector device (Ag/Au/NW network/mica/glass) revealed an on/off ratio of $>10^3$ and a fast response time less than 0.1 s. These respectable characteristics indicate good crystalline quality and connection of the NW network. Similarly, Sun *et al*.[77] grew cubic $CsPbBr_3$ NWs of 1 µm x 10 µm through VP epitaxial deposition on mica substrates. The reaction occurred in a multizone tube furnace starting from a 1:1 precursor mixture, which was heated to 380 °C while the mica substrate was held at 350 °C. Again, the obtained NWs exhibited a high crystalline quality and a low defect density. To increase the photoresponse over a broader spectral range and improve the photo-to-dark current ratio, amorphous indium-gallium-zinc oxide (IGZO) was deposited, forming a perovskite-IGZO heterojunction. IGZO is a typical n-type oxide semiconductor with a high electron mobility and a large bandgap of 3-3.4 eV, exhibiting great potential in ultraviolet optoelectronic applications. The corresponding UV-Vis photodetectors displayed good optoelectronic properties such as a low dark current of 0.1 nA (at -5 V), a high on/off ratio of 1.2×10^4, a response time of 2 ms, an R of 3.8 A W^{-1} and ambient stability for 2 months. The high photo-to-dark current ratio is attributed to the hybrid perovskite-IGZO structure, which forms a p-n-type heterojunction, in which holes efficiently diffuse to IGZO and free electrons diffuse to the $CsPbBr_3$ NWs. Shoaib *et al*. reported VP-induced graphoepitaxial growth of ultralong $CsPbBr_3$ NWs along the nanogrooves of M-plane sapphire substrates.[78] A 2:1 mixture of CsBr and $PbBr_2$ powder was placed at the center of the heating zone of a quartz tube under N_2 gas at ambient pressure. Annealed M-plane sapphire sheets with aligned V-shaped nanogrooves were placed downstream as the growth substrates. After 10 min at 600 °C, a large number of ultralong NWs were obtained on the sapphire surface. The as-obtained NWs exhibited widths of 500 nm, lengths up to several mm and high monoclinic crystallinity. Their

strong band-edge emission combined with the long PL decay time of 25 ns indicated limited optical scattering and leakage from the surface, as confirmed by efficient waveguiding (Figure 8a-d).[79] NW photodetectors were prepared by depositing 16.5 μm interspaced Au electrodes. The high R of 4400 AW^{-1} at 3 V and fast rise and decay times make them one of the most efficient photodetectors based on a single MHP NW. However, their efficiency is limited to a spectral range of 400-600 nm. In comparison, Oksenberg *et al*. demonstrated epitaxial and graphoepitaxial growth of $CsPbBr_3$ NWs as triangular prisms on flat C-plane and faceted M-plane sapphire surfaces, respectively.[71] Epitaxial growth resulted in horizontal NWs along six isoperiodic directions of the flat sapphire substrate, while graphoepitaxial growth led to aligned $CsPbBr_3$ NWs with bidirectional growth along the nanogrooves on the faceted sapphire substrate (Figure 7c,d). For the VP growth of the NWs, the 1:1 Cs to Pb precursor mixture was held at 550 °C in a three-zone tube furnace, while the substrates were placed downstream at 350-390 °C and ambient pressure. The NWs (50 nm – 1 μm x 100 μm) are highly crystalline cubic structures with axial growth along the [100] direction and triangular cross-sections driven by the maximum interface area between the V-shaped sapphire nanogroove and NW (Figure 7e). A typical photodetector contains between 1 and 10 relatively large $CsPbBr_3$ NWs crossing a 10-20 μm gap between the C/Ti electrodes (10 nm/100 nm). These devices exhibited low dark currents of 15 pA at 1 V and the fastest rise (5.2 μs) and decay (3.2 μs) times reported thus far for $CsPbBr_3$-based photodetectors.

Although VP methods lead to 1D nanostructures with improved crystalline quality and lower defect density compared with the solution-phase techniques, the noncatalyzed growth shows uncontrolled radial growth along the NWs. Meng *et al*. developed VLS growth of $CsPbX_3$ NWs on SiO_2/Si substrates by applying Sn catalysts (Figure 7f-g).[72] Different from the epitaxial deposition involving a vapor-solid interface, the critical feature of VLS growth is selective crystal growth at the liquid-solid interface. CsBr and $PbBr_2$ precursor powders with a molar ratio of 2:1 are placed in a tube furnace at 440 °C and 1.5 Torr. A substrate predeposited with Sn catalysts with a diameter of ∼ 150 nm is placed in the low-temperature zone at 310 °C. At this temperature, the Sn catalyst exists in its liquid state and becomes supersaturated through the VP precursors, leading to vertical growth of $CsPbX_3$ NWs at the liquid-solid interface. This results in defect-free and monocrystalline cubic $CsPbBr_3$ NW arrays with a uniform diameter of ∼150 nm and lengths up to 30 μm. The photodetectors consisted of single

$CsPbX_3$ NWs coated with Ti-Au electrodes and exhibited a notable performance with low dark currents of 0.1-1 pA at 5 V, up to 10^5 on/off ratios, a large R exceeding 3300 AW^{-1} and a D* of 6.0×10^{12} Jones across the visible light region. The notable photodetection performance is strongly related to the low trap-state density, causing long 1D carrier diffusion lengths on the order of 10 µm and long carrier lifetimes (0.1-1 µs) in these high-quality VLS-grown $CsPbBr_3$ NWs. Moreover, Meng *et al*. passivated the surface of VLS-grown $CsPbBr_3$ NWs with a MoO_3 shell to prevent the diffusion of detrimental water and oxygen molecules throughout the perovskite material.[80] Interfacial electron transfer from the $CsPbBr_3$ NW core to the MoO_3 shell strongly resembles a p-type heterojunction. This noninvasive surface doping does not introduce any additional impurity into the host crystal lattice but enhances the carrier mobility while eliminating charge carrier scattering by ionized dopants. The $CsPbBr_3$-MoO_3 core-shell NWs showed efficient photodetection with an R of 2.36 x 10^3 AW^{-1} and an EQE of ~5.48 x 10^5%.

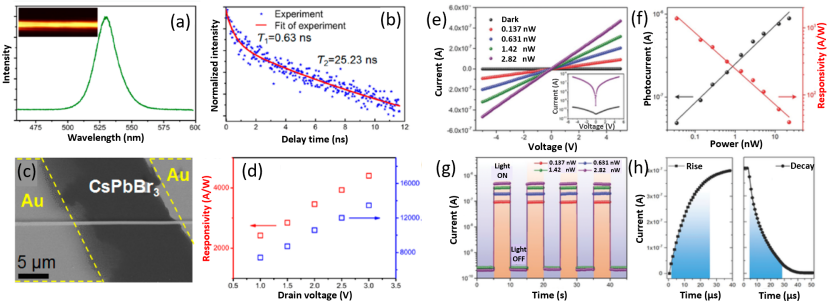

Figure 8. (a-d) Ultralong and directional $CsPbBr_3$ NWs grown along faceted M-plane sapphire. (a) PL spectrum of a NW. Inset: PL mapping of the NW. (b) Time-resolved PL decay kinetics. (c) SEM image of the as-fabricated device. (d) R and gain as a function of the bias voltage (irradiance 0.2 mW/cm^2) (λ_{exc} = 405 nm). (e-h) Device performance of a polarization-sensitive photodetector based on a 1D $CsPbBr_3$ NW array. (e) Dark current and photocurrent under different illumination powers. The inset shows logarithmic *I–V* curves in the dark and under 2.8 nW illumination power. (f) Photocurrent and R under different incident powers. (g) *I-t* response under different illumination powers. (h) Temporal response under 2.8 nW illumination power, which shows a fast rise time of 21.5 µs and a decay time of 23.4 µs. Reprinted with permission from (a-d) ref. 78, copyright 2017,

American Chemical Society and (e-h) ref. 73, copyright 2017, Wiley-VCH Verlag GmbH & Co. KGaA, Weinheim.

In general, NWs with high aspect ratios exhibit highly anisotropic optical absorption, PL emission and photoconductivity. However, single NW-based photodetectors only show a weak photocurrent due to the small surface area of the NW, impeding their applications as polarization-sensitive photodetectors. Hence, the construction of strictly aligned and crystallographically ordered NW arrays is a potential route to ensure large polarization anisotropy combined with a high photoresponse. Feng *et al*.[73] demonstrated the fabrication of perfectly aligned 1D $CsPbBr_3$ NW arrays with controlled dimensions of ~ 500 nm × 8 μm and high cubic crystallinity with a low carrier trap density. A capillary effect governs the growth process of the perovskite NWs in the micropillar-structured template with asymmetric wettability. The lyophobic tops have little or no affinity for the precursor liquid, and the lyophilic sidewalls are marked by a strong affinity for the perovskite solution (Figure 7h,i). A high-performance polarization-sensitive photodetector based on these 1D $CsPbBr_3$ arrays exhibited an R of 1377 AW^{-1}, a photoconductive gain of approximately 10^4 and fast rise and decay times (Figure 8e-h).

The application of individual or aligned NWs in metal/$CsPbBr_3$/metal photodetectors requires complex preparation procedures and nanoscale manipulation. Generally, the photocurrents achieved for these devices are limited due to the small absorption cross-section or the large spacing between the metal electrodes. Moreover, for these systems, integrating a p-n junction or a proper Schottky barrier junction to produce high-performance self-powered photodetector devices is very challenging. Zhou *et al*. were pioneers in the design of self-powered $CsPbBr_3$ NW photodetectors with a vertical p-i-n structure.[81] A combination of solution-phase and halide exchange processes led to orthorhombic-structured $CsPbBr_3$ NWs (Cs to Pb < 1) with dimensions of 180 nm × ± 20 μm. Poly(methyl methacrylate) was coated onto the perovskite NWs to fill the voids and thereby passivate the surface defects. This layer was then sandwiched between SnO_2 and poly(triarylamine) as the electron and hole selective layers, respectively. The passivation effect resulted in an ultralow J_{dark} of 4.0 nA cm^{-2} and a high photocurrent density of 22.9 mA cm^{-2}, leading to a high linear dynamic range (LDR) of 135 dB. In addition, the self-powered $CsPbBr_3$ NW devices exhibited ultrahigh on/off ratios above 10^6, an R of up to

0.3 AW^{-1} and a high D* of up to 1×10^{13} Jones at 0 V with a relatively fast response speed of 0.4 ms.

An improved self-powered UV-vis-NIR photodetector was fabricated by integrating a $CsPbBr_3$ NW array with PDPP3T and P3HT conjugated polymers.[82] The 1D array consisting of NWs with widths of 500 nm and lengths up to several cm was prepared by spin-coating a 1:1 $CsBr/PbBr_2$ precursor onto SnO_2/ITO substrates, followed by imprinting and annealing. Consequently, the PDPP3T and P3HT polymer layers were spin-coated on top of the $CsPbBr_3$ 1D array. Optoelectronic measurements revealed that the hybrid photodetector (Ag/P3HT/PDPP3T/$CsPbBr_3$ NWs/SnO_2/ITO) has a broad photoresponse from the 300 to 950 nm window with a fast response speed of 111 µs, an R of 0.25 AW^{-1}, a large D* of 1.2×10^{13} Jones and excellent stability in the wide UV-vis-NIR spectral region. These beneficial values are mainly attributed to the increased light harvesting through the NW array structure and the proper bandgap alignment with the conjugated polymers promoting efficient photogenerated carrier separation and transport.

Wang *et al*. created a self-powered lateral photodetector based on $CsPbI_3$-$CsPbBr_3$ heterojunction nanowire arrays.[83] The photodetector was fabricated on two different substrates, i.e. a rigid glass and flexible polyethylene naphthalate (PEN), wherein a $CsPbI_3$ film was printed into a nanowire array and then coated with a thin polydimethylsiloxane (PDMS) film. Next, Ag wires were aligned as electrodes. Finally, half of the Ag wires and the PDMS film was removed to perform VP ion exchange in a vacuum tube furnace, transforming the $CsPbI_3$ nanowires into $CsPbBr_3$. The resulting heterojunction device exhibited an R of 125 mAW^{-1} and a fast rise and decay time of 0.7 and 0.8 ms under 650 nm illumination and zero bias. Furthermore, the light response of the rigid and flexible detector is very similar, leaving ample opportunities for the development of self-powered, flexible NW-based photodetectors.

To date, $CsPbBr_3$ NWs have mostly been applied in low-energy photodetectors and have not yet been used for high-energy radiation detection. Photodetectors based on $CsPbBr_3$ NWs with controlled crystallographic orientation obtained by VP epitaxial growth exhibited high on/off ratios over 10^4 and the fastest rise and decay times reported thus far.[71,77,78] Additionally, Sn-catalyzed VLS vertical growth of $CsPbX_3$ NWs resulted in photodetectors with 10^5 on/off ratios, large R and a D* of 6.0×10^{12} Jones across the visible light region.[72] However, VP- or VLS-assisted

crystal growth is quite a demanding technique, requiring high temperatures up to 600 °C and/or reduced pressure. In contrast, the D* of a photodetector device based on simple solution-processed NWs was only slightly lower, at approximately 1.7×10^{11} Jones, but this device exhibited substantially slower response times in the ms range.[70] As a substantial improvement, coating the solution-processed perovskite NWs with additional polymer layers allowed stabilization via encapsulation and defect passivation, simultaneously extending the sensitivity over a broader spectral window and shortening the response times with self-powered photodetection (V_{bias} = 0 V) due to efficient carrier extraction, leading to record on/off ratios of above 10^6 and D* up to 1.2×10^{13} Jones.[81,82] Other innovative approaches include the creation of a perovskite hybrid structure with, e.g., single-layer graphene, which has shown to combine the favorable light-harvesting properties of the perovskite with efficient electron transfer to the highly conductive graphene.[84] Furthermore, the fact that the optical properties of perovskite NWs are polarization sensitive can be exploited for next-generation polarization-sensitive photodetector devices, potentially based on bespoke perovskite-graphene heterojunctions.

Table 4. Summary of critical parameters and the corresponding device performance of $CsPbBr_3$ nanowires.

Material (device structure)	Preparation method	Responsivity (light source, intensity, bias)	Detectivity (light source, intensity, bias)	Response speed rise/decay time (light source, intensity, bias)	on/off ratio (dark/photo-current)	External quantum efficiency	Reference
$CsPbBr_3$ ($Ag/P_3HT/PDPP_3T/CsPbBr_3/SnO_2/ITO$)	Precursor spincoating	0.25 $A\,W^{-1}$ (self-powered)	1.2 x 10^{13} Jones (0 V)	111/306 µs	--	85 %	82
$CsPbBr_3$ ($CsPbBr_3$/Ti-Au electrodes)	VLS	3306 $A\,W^{-1}$	6.0 x 10^{12} Jones	Less than 50 ms	10^4 - 10^5	--	72
$CsPbBr_3$ (Photo glass/ITO/SnO_2/$CsPbBr_3$/ PTAA/Au)	Solution phase	0.3 $A\,W^{-1}$ (self-powered)	1.0 x 10^{13} Jones (0 V)	0.4/0.43 ms	> 10^6	--	81
$CsPbBr_3$ (Au/$CsPbBr_3$/Au 16.5 µm spacing)	VP	4400 $A\,W^{-1}$ (3V)	--	252/300 µs	--	--	78
$CsPbBr_3$ (SiO_2/Si wafers/$CsPbBr_3$/Ti-Au electrodes)	Solvothermal synthesis	--	--	--	1100 (365 nm, 8 V)	--	12
$CsPbBr_3$ (Au/$CsPbBr_3$/Au 100 µm interdigitated electrode spacing)	Solution phase – halide exchange	1.13 $A\,W^{-1}$	1.7 x 10^{11} Jones	10/22 ms	> 150	--	70
$CsPbBr_3$ (Ag/Au/$CsPbBr_3$/Mica/glass)	VP	--	--	< 0.1 s	> 10^3	--	76
$CsPbBr_3$ (C/Ti electrodes 10-20 µm gap)	VP	--	--	5.2/3.2 µs	10^3	--	71
$CsPbBr_3$	Confining	1377 $A\,w^{-1}$	--	21.5/23.4 µs	3632 to 10^6	--	73
$CsPbBr_3$ (metal electrodes/$CsPbBr_3$/IGZO)	VP	3.8 $A\,W^{-1}$	--	2/96 ms	1.2 x 10^4	--	77
$CsPbBr_3$ (Si/SiO_2/$CsPbBr_3$-MoO3/Au)	VLS	2.36 x 10^3 $A\,W^{-1}$	2.1 x 10^{12} Jones	230/280 µs	10^3	5.48 x 10^5 %	80
$CsPbBr_3$ (PEN/$CsPbI_3$-$CsPbBr_3$/PDMS/Ag)	Halide exchange	125 mA W^{-1} (650 nm, self-powered)	--	0.7/0.8 ms	1000	--	83

1.5 Thin Films

The extensively explored polycrystalline thin-film solar cell strategy has been adapted as a straightforward solution-processable approach for $CsPbBr_3$ thin-film photodetectors.[11,85–87] The main challenges consist of making a uniform and compact film of large grain sizes, thereby minimizing the presence of grain boundaries, which are detrimental to the device performance due to the inefficient charge transport and nonradiative recombination. Li *et al.* employed a novel recyclable dissolution-recrystallization (RDR) technique to obtain large-area, crack-free, low-roughness $CsPbBr_3$ thin films. The thin films capped with surface ligands were slowly washed with a mixture of ethanol and toluene, allowing reversible size tuning of the particles from 10 nm up to 1 μm.[11] Highly dynamic ligand binding with a high surface diffusion coefficient[88] of the ligands allows a fast exchange of surface atom-surfactant species between their bound and free states so that they can be easily washed off the surface. Low polarity toluene enhances this diffusion process, while high polarity ethanol promotes the dissolution of surface atoms. Following the evaporation of these solvents, the dissolved species reattach to the particle surfaces and recrystallize, forming a large-grain, compact and uniform film by connecting isolated particles (Figures 9a-f). The significantly improved film results in superior enhancement of the charge transport with an R of ~ 700%, an EQE of ~ 700%, a fast response speed (1.0 and 1.8 ms rise and decay times), and high device stability.[11] To tackle the low precursor solubility and uncontrolled growth issue of $CsPbBr_3$ thin films, Zeng *et al*. utilized ordered polystyrene sphere templates for space-confined growth of ultradense polycrystalline thin films with preferred orientation and enlarged crystal grains.[87] The device showed a record D* of 7.55×10^{13} Jones, an R of 216 A W^{-1}, a high LDR of 101 dB and a 3.1×10^5 Hz 3 dB bandwidth with ultrafast rise (4 μs) and decay (5 μs) times.[87] Additionally, the optimized 1:1.2 CsBr to $PbBr_2$ ratio led to the lowest trap density of 3.07×10^{12} cm^{-3} and the highest carrier mobility of 9.27 cm^2 V^{-1} s^{-1} among $CsPbBr_3$ polycrystalline films, which was further supported by XRD, PL lifetime, and Urbach energy measurements (Figure 9g,h). A lower amount of $PbBr_2$ resulted in less textured films, and higher amounts of $PbBr_2$ may reside between the grain boundaries, which reduces carrier transport and increases nonradiative recombination. A recent finding by Ramadan *et al*. showed that a small modulation of the Cs content at substoichiometric concentrations causes a considerable variation in the electronic structure of $CsPbBr_3$.[89] However, above a critical point (CsBr:$PbBr_2$ = 0.75:1.0), changes in the chemical composition do not significantly alter the band energies, revealing the

stoichiometric tolerance of $CsPbBr_3$ thin films.[89] Ji *et al*. fabricated an all-inorganic $NiO_x/CsPbBr_3/TiO_2$ photodetector, where the perovskite layer was formed by spin-coating and the two charge transport layers were formed via atomic layer deposition. The NiO_x layer assists in forming a high-quality perovskite layer via an efficient interfacial interaction at the substrate/perovskite interface and acts as an efficient hole transport layer (HTL), while TiO_2 passivates surface defects and extracts photogenerated electrons.[90] The optimized device exhibited an ultralow dark current of ~10^{-11} A, rise/fall times of 0.056/0.25 ms, an LDR of 186.7 dB and an ultralow detection limit of 857 pW cm^{-2}.

Fernandez-Izquierdo *et al*.[91] applied an innovative close space sublimation (CSS) process to deposit thin $CsPbBr_3$ films with controlled thickness. Millimeter-sized AVC-grown $CsPbBr_3$ SCs were used as a source for the CSS process under vacuum at 500 °C, followed by postdeposition annealing, resulting in large single-grain columnar growth of the films. Photolithographic deposition of a Ga_2O_3 layer formed a $Ga_2O_3/CsPbBr_3$ diode on patterned ITO for indirect neutron sensing. The device showed a low leakage current of 5 x 10^{-8} A mm^{-2}, a rectification of 10^4 and rise/decay times of 190/460 µs.

Liu *et al*. fabricated a pinhole-free uniform $CsPb_2Br_5$-$CsPbBr_3$ perovskite film with an average grain size of ≈1 µm showing good photodetector behavior, as the 2D $CsPb_2Br_5$ phase effectively reduces carrier recombination by bromide vacancy filling at the grain boundaries.[92]

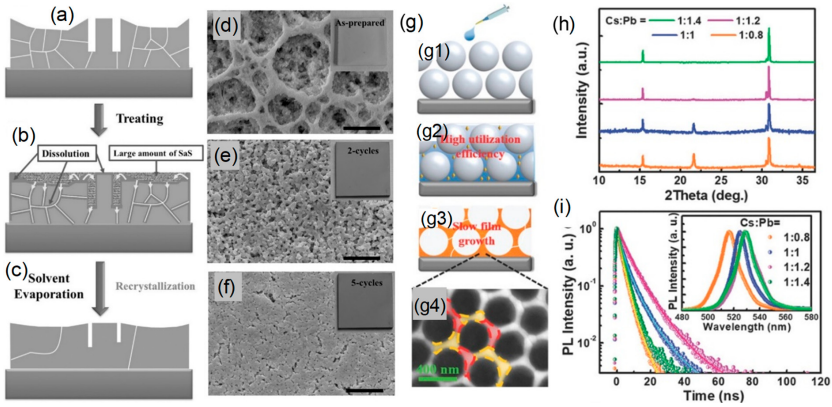

Figure 9. Schematic of the $CsPbBr_3$ thin film modification mechanism: (a) High film roughness and low continuity in the original film. (b) Mixed-solvent (ethanol and toluene)-induced film modification process: surface and sharp parts dissolve, and the fast-exchanging surface atoms-surfactants (SaS) diffuse to the gaps and holes. After the evaporation of solvents, the SaS recrystallize, and the films are healed. (c) Compact and smooth film after solvent evaporation. SEM images of (d) a pristine $CsPbBr_3$ thin film and thin films treated (e) two and (f) five times with mixed solvents during the successive healing of $CsPbBr_3$ films via RDR. The scale bars are 5 μm, and the insets are pictures of the corresponding samples. (g) Schematic illustration of space-confined $CsPbBr_3$ film fabrication strategies. (h) XRD patterns and (i) PL decay and PL spectra (inset) of stoichiometrically modulated thin films. Reprinted with permission from (a-f) ref. 11 and (g-h) ref. 87, copyright 2016, 2018, Wiley-VCH Verlag GmbH & Co. KGaA, Weinheim.

Table 5. Summary of critical parameters and the corresponding device performance of $CsPbBr_3$ thin films.

Material (device structure)	Preparation method	Responsivity (light source, intensity, bias)	Detectivity (light source, intensity, bias)	Response speed rise/decay time (light source, intensity, bias)	on/off ratio (dark/photo-current)	External quantum efficiency	Reference
$CsPbBr_3$ ($Au/CsPbBr_3/Au$)	Centrifugal casting	0.18 A W^{-1}	6.1 x 10^{10} Jones (442 nm, 1.01 mW cm^{-2}, 1.3V)	1.8/1.0 ms	8000	41% (531 nm, 10 V)	11
$CsPbBr_3$ ($Au/CsPbBr_3/Au$)	Spin-coating	55 A W^{-1}	0.9 x 10^{13} Jones	0.43/0.318 ms	10^5 (405 nm, 25.3 mW, 6V)	16700	86
$CsPbBr_3$–ZnO ($Au/CsPbBr_3$–ZnO/Au)	Spin-coating	4.25 A W^{-1} (515 nm, 10V)	--	0.21/0.24 ms	10^4 (450 nm, 0.15-32.58 mW cm^{-2}, 10 V)	--	85
$CsPbBr_3$ ($Au/CsPbBr_3/Au$)	Spin-coating	216 A W^{-1}	7.55 x 10^{13} Jones	3.96/4.92 µs	1.5 x 10^5 (442 nm laser, 47 µW, 5V)	--	87
$CsPbBr_3$ ($Au/CsPbBr_3/Au$)	Templated growth	1000 A W^{-1} (470 nm, 5V)	--	21.5/23.4 µs (2.82 nW)	10^3	--	73
$CsPbBr_3$ ($ITO/Ga_2O_3/CsPbBr_3$)	CSS	4.33 A W^{-1}	--	0.19/0.46 ms	10^2	--	91
$CsPbBr_3$ ($NiO_x/CsPbBr_3/TiO_2$)	Spin-coating	0.22 A W^{-1}	1.59 x 10^{13} Jones	56/250 µs	--	--	90
$CsPbBr_3$-$CsPb_2Br_5$ ($SnO_2/CsPbBr_3$-$CsPb_2Br_5$/Carbon)	Spin-Coating	0.109 A W^{-1}	1.4 x 10^{12} Jones	--	1.37 x 10^6	--	92

1.6 Nanocrystals

Colloidal NC synthesis allows superior control over the particle size and shape, improved surface morphology, crystallinity, optoelectronic properties and exhibits better environmental stability with reduced defect densities. Since the initial report describing the possible synthesis of MHP NCs,[93] rigorous development of new synthesis methodologies has been pursued. The most commonly used techniques include hot injection and RT antisolvent-based ligand-assisted reprecipitation (LARP), which effectively produces uniform $CsPbX_3$ NCs.[94,20,95] Song *et al*. synthesized 2D $CsPbBr_3$ nanosheets (NSs) by a modified colloidal hot-injection strategy (Figure 1i) using long-chain alkyl amines and oleic acid (OAc) surfactants.[14] The use of a mixture of dodecylamine, oleylamine (OAm) and n-octylamine resulted in large-scale formation of high-quality cubic 2D $CsPbBr_3$ NSs with an edge length of approximately 1 µm (Figure 10a). Both AFM (Figures 10b,c) and small-angle X-ray diffraction measurements confirmed the formation of mono- and bilayer $CsPbBr_3$ NSs. Their large surface area results in good light absorption along with long carrier diffusion lengths. Centrifugal casting of these NSs on a PET/ITO flexible substrate formed a compact film with a 120 nm thickness (Figures 10d). The corresponding photodetector exhibited a high photocurrent and a low dark current of 3 µA and 0.9 nA at 5 V, respectively, with an on/off ratio of ~10^3, an R of 0.25 AW^{-1} and a peak EQE of 53%, indicating good photoswitching behavior (Figures 10e). Similarly, Lv *et al*.[96] synthesized monolayer thick (~2 nm) $CsPbBr_3$ NSs by modifying the hot-injection synthesis of Protesescu *et al*.[93] The volume of OAm was doubled, and cesium oleate was mixed in pure OAc to prevent RT precipitation. These modifications led to the formation of uniform NSs via an oriented attachment mechanism.[97] The ultrathin NSs were dropcasted on an Au electrode (50 nm) with a channel dimension of 20 µm × 2000 µm, on a SiO_2/Si substrate, exhibiting fast rise and decay times of 17.8 ms and 14.7 ms with a low dark current of 10^{-12} A. Similarly, Shen *et al*. applied solution-processed $CsPbBr_3$ quantum dots (QDs) treated with a CsBr/KBr mixture, obtaining high-performance flexible photodetectors exhibiting a high R of 10.1 A W^{-1}, a D* of 9.35×10^{13} Jones, and an on/off ratio up to ≈10^4.[98] Similarly, Zhao *et al*. fabricated transparent $CsPbBr_3$ QDs photodetectors showing a good performance.[99]

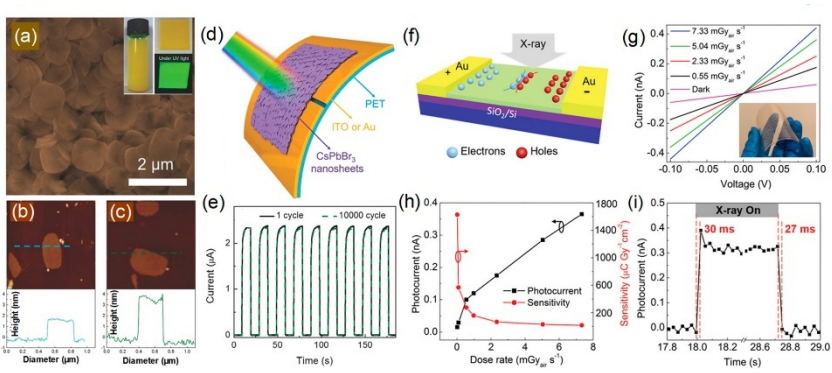

Figure 10. (a) SEM and (b-c) AFM images and height profiles of 2D ultrathin $CsPbBr_3$ NSs. The inset shows photographs of the NS dispersion and film without and with UV excitation. (d) Schematic diagram of the flexible NS device structure. (e) Photoresponse at a 5 V bias in the 1st and 10000th bending-recovery cycles of the printed flexible photodetector. (f) Schematic illustration of the device architecture and working principle of the $CsPbBr_3$ NC-based X-ray detector. (g) *I-V* curve under different X-ray dose rates, (h) X-ray photocurrent and sensitivity as a function of dose rate and (i) temporal response of the device under a 7.33 mGy_{air} s^{-1} dose rate with a 0.1 V external bias voltage. Reprinted with permission from (a-e) ref 14. and (f-i) ref. 100 copyright 2016, 2019, Wiley-VCH Verlag GmbH & Co. KGaA, Weinheim.

Liu *et al*. utilized solution-processed $CsPbBr_3$ QDs in both rigid and flexible X-ray detectors towards the direct conversion of soft X-rays (Figures 10f-i).[100] $CsPbBr_3$ QDs were synthesized by using a modified hot-injection technique. Instead of OAc, they employed diiso-octyl phosphinic acid to solubilize Cs_2CO_3 and $PbBr_2$. The X-ray detector device was fabricated on a SiO_2/Si substrate and a flexible PET substrate with source-drain contacts of Cr/Au (15/50 nm) with a channel width of 10 μm. At a synchrotron soft X-ray beamline, the optimized device showed a high sensitivity of 1450 μC Gy_{air}^{-1} cm^{-2} under a 17.2 μGy_{air} s^{-1} X-ray dose and a 0.1 V bias, which is ~70 times more sensitive than conventional α-Se-based devices.[100] Furthermore, the authors demonstrated multichannel detector arrays by performing large-scale QD fabrication via inexpensive inkjet printing. Similar observations were reported by Xin *et al*., where $CsPbBr_3$ NCs were prepared by LARP.[101] $CsPbBr_3$ NCs are generally highly luminescent due to the fast

radiative recombination kinetics of the photogenerated excitons. Efficient interfacial transfer of photogenerated electrons and holes will enhance the efficiency of $CsPbBr_3$ NCs photodetectors. Either the use of suitable hole and electron transporting layers[21,102] or the addition of small molecules[103] can efficiently separate photogenerated hot charge carriers.

Table 6. Summary of critical parameters and the corresponding device performance of $CsPbBr_3$ nanocrystals.

Material (device structure)	Preparation method	Responsivity (light source, intensity, bias)	Detectivity (light source, intensity, bias)	Response speed rise/decay time (light source, intensity, bias)	on/off ratio (dark/photo-current)	External quantum efficiency	Reference
$CsPbI_3$ (Au/$CsPbI_3$/Au)	Hot-injection	--	--	0.024/0.029 ms	10^5 (405 nm)	--	95
$CsPbBr_3$ (ITO/$CsPbBr_3$/ITO)	Hot-injection	0.64 A W^{-1}	--	0.019/0.024 ms (442 nm, 0.35 mW cm^{-2} to 4.74 mW cm^{-2})	10^4 (442 nm)	54% (515 nm, 10V)	14
$CsPbI_3$ (Au/$CsPbI_3$/Au)	Hot-injection	--	--	17.8/14.7 ms (450 nm, 13.0 mW cm^{-2}, 1 V)	--	--	96
$CsPbBr_{3-x}I_x$ (Au/Graphene-$CsPbBr_{3-x}I_x$/Au)	Hot-injection	8.2 x 10^6 A W^{-1} (405 nm, 0.07 μW cm^{-2})	2.4 x 10^{16} Jones	0.81/3.65 s (405 nm, 1 V)	--	--	105
$CsPbI_3$ (Au/$CsPbI_3$/Au)	LARP	10.04 A W^{-1}	4.56 x 10^8 Jones	0.2/1.2 ms	1.6 x 10^6 (532 nm, 4.65 mW cm^{-2}, 2V)	8%	109
$CsPbBr_3$-CNTs (Ag/$CsPbBr_3$-CNTs/Ag)	LARP	31.1 A W^{-1} (442 nm, 3 V)	--	0.016/0.38 ms (40 μW, 3 V)	10^5	7488 (442 nm, 3 V)	110
$CsPbBr_3$-dina… (Au/$CsPbBr_3$ dina/Au)	Hot-injection	1.7 x 10^4 A W^{-1}	2 x 10^{14} Jones	1.089/1.438 s	8.1 x 10^4 (460 nm, 1 mW cm^{-2}, -20V)	67000 (400 nm, 0.5 mW cm^{-2}, −10 V)	104
$CsPbBr_3$–PbS (Au/$CsPbBr_3$–PbS/Au)	LARP	4.5 x 10^5 A W^{-1}	1.26 x 10^{13} Jones	6.5 ms/7.5 ms	1.4 x 10^8	--	106
$CsPbBr_3$-MPA(mp-TiO2) (Au/$CsPbBr_3$-MPA(mp-TiO2)/Au)	Hot-injection	24.5 A W^{-1}	8.9 x 10^{13} Jones	4700/2300 ms	10^5	--	120
$CsPbBr_3$-$CH_3NH_3PbI_{3-x}Cl_x$ (Au/$CsPbBr_3$-$CH_3NH_3PbI_{3-x}Cl_x$/Au)	Hot-injection	0.39 A W^{-1} (405 nm, 200 mW cm^{-2},1 V)	5.43 x 10^9 Jones	0.121/0.107 ms	--	--	107
$CsPbBr_3$–MoS_2 (Au/$CsPbBr_3$–MoS_2/Au)	LARP	4.4 A W^{-1} (442 nm, 20 μW cm^{-2},10 V)	2.5 x 10^{10} Jones	0.72/1.01 ms	16700	302 %	118
$CsPbBr_3$	Hot-injection	0.08 A W^{-1}	2.2 x 10^{11} Jones	--	--	--	99
Material (device structure)	**Preparation method**	**Sensitivity**	**Detection limit**	**Response speed rise/decay time (light source, intensity, bias)**	**on/off ratio (dark/photo-current)**		**Reference**
$CsPbBr_3$ (Au/$CsPbBr_3$/Au)	Hot-injection	1450 μC Gy_{air}^{-1} cm^{-2} (0.0172 mGy_{air} s^{-1}, 0.1 V)	--	30/27 ms	--	--	100

1.7 Hybrid Nanocrystal Photodetectors

Although $CsPbBr_3$ NC photodetectors exhibit great potential, the low charge transport efficiency limits their potential application. To overcome this limitation, several strategies have been developed to fabricate a hybrid composite device with the introduction of organic semiconductors,[104] graphene[105] and metal chalcogenides.[106] Composite photodetectors are beneficial for enhancing the charge transport and further increasing the stability of $CsPbBr_3$ NCs. The most promising hybrid NC photodetectors are discussed in this section. Yang *et al.* employed a $CH_3NH_3PbI_{3-x}Cl_x$ MHP layer decorated with all-inorganic $CsPbBr_3$ QDs towards a fast response photodetector.[107] The $CH_3NH_3PbI_{3-x}Cl_x$ layer was fabricated on a Si/SiO_2 layer by spin-coating a solution containing 1:3 molar ratio $PbCl_2/CH_3NH_3I$ in DMF, followed by thermal annealing. Then, cubic-phase $CsPbBr_3$ NCs, which were synthesized by the conventional hot-injection procedure with a limited Cs-oleate concentration, were spin-coated on top.[108] The Fermi energy (E_F) level of $CsPbBr_3$ is higher than that of the hybrid MHP, facilitating the transport of holes from the sensitizer ($CsPbBr_3$) to the active layer ($CH_3NH_3PbI_{3-x}Cl_x$). The hybrid photodetector operating in the visible spectral window exhibited R ~0.39 AW^{-1}, D* ~5.43 × 10^9 Jones, carrier mobilities $\mu_p = 172\ cm^2\ V^{-1}s^{-1}$ and $\mu_n = 216\ cm^2\ V^{-1}s^{-1}$, and rise and fall times of 121 µs and 107 µs, respectively.[107,108]

Following this, a novel $CsPbBr_3$-Au nanocomposite-based photodetector was fabricated by coupling the overlapping localized surface plasmon resonance (LSPR) of noble Au metal NCs to the broad MHP absorbance.[109] Dong *et al.* found that the LSPR of Au NCs overlaps perfectly with the $CsPbBr_3$ NC absorption window, favoring the plasmonic enhancement factor towards more efficient photodetectors.[109] Highly monodisperse cubic-shaped $CsPbBr_3$ NCs of 60-80 nm were synthesized by LARP (Figure 1j).[94] In a typical process, equal molar $PbBr_2$ and CsBr were dissolved in DMSO via ultrasonication, followed by the addition of OAc and OAm. This mixture was swiftly added to toluene at RT to start crystallization. The centrifugal-cast $CsPbBr_3$ NC thin film shows texturing along the (200) direction, forming a compact oriented film with a smooth surface, allowing facile charge transport (Figure 11a). The $CsPbBr_3$ NC film is centrifugally cast on top of a Au NC film. The synergistic effect of the photogenerated carriers in the oriented $CsPbBr_3$ film along with LSPR coupling of the Au NCs led to a photocurrent rise from 245.6 to 831.1 µA due to the plasmonic enhancement factor and a 10^6 on/off ratio at a 2 V bias with high photoswitching stability (Figure 11b). Chen *et al*.[104] demonstrated a

very promising high-performance phototransistor based on a hybrid $CsPbBr_3$ NC-dinaphtho[2,3-*b*:2′,3′-*f*]thieno[3,2-*b*]thiophen organic semiconductor composite. The ordered packing of organic semiconductor molecules above the smooth surface of the $CsPbBr_3$ layer resulted in high charge transport efficiency. Additionally, the gate effect of the transistor structure enhanced R by maintaining a high I_{photo}/I_{dark} ratio such that the device exhibited very high R (1.7×10^4 AW^{-1}), D* (2.0×10^{14} Jones), EQE (67000%), and on/off ratio (8.1×10^4) along with prolonged ambient stability, which are much higher than those of state-of-the-art perovskite-only photodetectors.[104]

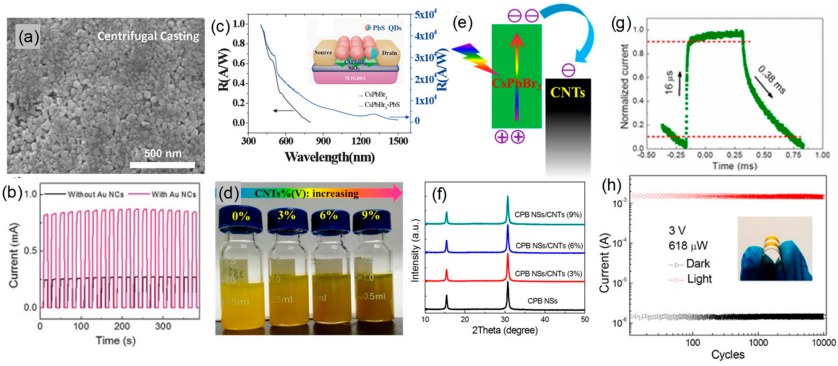

Figure 11. (a) SEM image of a centrifugal-cast $CsPbBr_3$ film. (b) Photoswitching (*I*-*t*) curves of $CsPbBr_3$/Au NC photodetectors under 532 nm laser illumination and a 2 V bias. (c) *R* of the $CsPbBr_3$-PbS hybrid phototransistor over the 400-1500 nm window under a 2 V bias and zero applied gate bias. The inset shows the device schematic. (d) Photograph of the dispersions with different amounts of $CsPbBr_3$ NSs mixed with carbon nanotubes (CNTs), (e) type-II energy level of $CsPbBr_3$ NSs and CNTs, and (f) thin film XRD patterns. (g) Rise and decay times of the device at a frequency of 500 Hz. (h) Photocurrent and dark current after more than 10000 cycles under a 3 V bias with 442 nm light illumination; the inset shows a photograph of the flexible device. Reprinted with permission from (a, b) ref. 109, and (c) ref. 106, copyright 2016, 2017, Wiley-VCH Verlag GmbH & Co. KGaA, Weinheim and (d-h) ref. 110 copyright 2017, American Chemical Society.

Kwak *et al*. employed a similar composite strategy towards the fabrication of a high-performance hybrid photodetector of $CsPbBr_{3-x}I_x$-graphene by combining the high absorptivity of MHPs and high mobility of 2D graphene.[105] The ultrahigh carrier mobility in 2D graphene (~2 x 10^5 cm^2 V^{-1} s^{-1}) in combination with the high absorptivity of $CsPbBr_3$ NCs resulted in a highly photosensitive 2D-0D composite photodetector.[111,112] Colloidal hot-injection-synthesized $CsPbBr_3$ NCs[93] were anion-exchanged with LiI,[95] achieving 10 nm cubic-phase $CsPbBr_{3-x}I_x$ NCs. The corresponding photodetector exhibited high R of ~10^8 AW^{-1} and D* of ~10^{16} Jones, exceeding those of all other graphene-based composites, including hybrid organic-inorganic MHP-graphene composites.[112–117] However, the rise and decay times of 0.81 s and 3.65 s, respectively, are much slower than those of other photodetectors, which is ascribed to the inhibition of charge transport by the bulky OAc and OAm capping ligands on the NCs and requires further investigation.[105] Similarly, Yu *et al*. fabricated a heterojunction phototransistor consisting of $CsPbBr_3$-PbS NCs.[106] PbS NCs were spin-coated on top of cubic-phase $CsPbBr_3$ NC thin films synthesized by RT LARP. Subsequently, ligand exchange was performed with a short-chain ethanedithiol ligand to enhance the charge transport. The coupling of these two different classes of semiconductor NCs via type-II bandgap energy alignment led to a high mobility and efficient charge carrier separation. Furthermore, the absorbance of the composite film extended from the visible to the NIR window. The corresponding hybrid phototransistor exhibited excellent stability and reproducibility along with an R of 4.5×10^5 AW^{-1}, a D* of 7×10^{13} Jones, and fast rise and decay times of 6.5 ms and 7.5 ms, respectively (Figure 11c).[106] However, the photoresponse mechanism heavily depends on the photoexcitation energy (hv). For hv > 2.3 eV, both materials generate excitons that accumulate over PbS due to the bandgap energy alignment. For 2.3 eV > hv > 0.9 eV, charge carriers are mostly generated in PbS, yielding a low photocurrent, which completely diminishes at hv < 0.9 eV. Similarly, hybrid $CsPbBr_3$ NSs-MoS_2 resulted in high-performance photodetectors via efficient charge transfer attributed to suitable band alignment over a broad absorption window between 350 and 800 nm.[118]

Zhou *et al*. utilized hot-injection-synthesized $CsPbBr_3$ NCs as a photosensitizer combined with a mesoporous TiO_2 (m-TiO_2) film, showing a three times improvement in the on/off ratio compared to the pristine device by suppressing the dark current and hysteresis.[119,120] The twofold PL quenching and faster lifetime of $CsPbBr_3$ NCs imply efficient extraction of charge carriers in the composite structure.[119] In a consecutive study, Zhou *et al.* introduced

3-mercaptopropionic acid (MPA) as a bifunctional linker molecule between $CsPbBr_3$ and m-TiO_2, which further improved the device performance via faster electron transfer.[120] A high on/off ratio of 10^5 was observed, which is two orders of magnitude higher than that of the device without the linker. Furthermore, R was significantly enhanced from ~2.2 to ~24.5 AW^{-1}, and D* increased from 3.5×10^{12} to 8.9×10^{13} Jones.[120] Li *et al.* combined $CsPbBr_3$ NSs with carbon nanotubes (CNTs) to enhance the perovskite film conductivity and fast carrier transport towards efficient photodetectors (Figures 11d-f).[110] $CsPbBr_3$ NSs were synthesized by adapting the LARP method,[118] where CsBr and $PbBr_2$ in a 1:0.5 molar ratio were dissolved in DMSO with octadecylamine and acetic acid by prolonged ultrasonication. This mixture was then injected into toluene under RT stirring to start the nucleation. Due to the negligible resistance of CNTs, the total resistance of the device was substantially reduced. The optimized device with 6% CNTs showed an R of 31.1 AW^{-1} and an EQE of 7488%, along with a fast rise time of 16 µs and a decay time of 0.38 ms under a 10 V external bias and 442 nm excitation. Additionally, the ultrathin 2D and 1D nature of the $CsPbBr_3$ and CNTs in the composite film resulted in impressive flexibility of the device (>10000 bending cycles) and stability of the photoresponse (< 3.8% after 10000 on/off switching cycles), making this a very promising pathway for commercial photodetectors (Figures 11g,h).[110]

Nanocrystalline $CsPbBr_3$ has been synthesized either by hot injection or LARP, with both techniques leading to comparable optoelectronic properties. Despite the presence of bulky surface capping ligands that hinder effective charge transport, the solution processability offers ease of fabrication for flexible thin-film optoelectronic devices. Hybrid NC composites further extend the optical absorption window, reduce defects by surface passivation, increase the absorptivity, efficiently separate photogenerated charges, and enhance the NC stability by encapsulation, making them better photodetectors.

1.8 Summary and Outlook

Light-to-electrical signal conversion plays a crucial role in everyday life within applications such as imaging devices, cameras, and security or medical scanners. The ubiquitous nature of MHP semiconductors within solar cells, LEDs, lasers, and photocatalysts has recently motivated researchers to explore effective ways to repurpose them for efficient low- and high-energy radiation detectors. The facile synthesis strategies, tunable bandgaps, large absorption coefficients, ambipolar charge transport, and long carrier diffusion lengths of hybrid organic-inorganic MHPs make them excellent candidates for next-generation photodetectors. However, the severe perturbation in the structural, chemical, and thermal stability under ambient and high humidity conditions poses major technical hurdles towards industrialization. All-inorganic $CsPbBr_3$ perovskite is a suitable alternative for photodetection in terms of its chemical and structural stability under ambient conditions. Additionally, the design of composite-$CsPbBr_3$ devices further extends the photodetection window. In this review, we have discussed the synthesis, growth and optoelectronic properties towards low- and high-energy radiation detection of $CsPbBr_3$ perovskites across SCs, MCs, NWs, thin films, NCs, and composites in terms of the versatile reaction stoichiometry, crystal purity, morphology, device architecture, and interfacial engineering. High-quality SCs can be prepared by either solid-state or solution-phase synthesis, both yielding good performance when the SCs are implemented in devices. However, each synthetic method requires its own specific conditions in terms of reagent stoichiometry, solvents, and temperature and should be carefully considered. The linear charge carrier transport in combination with the sizeable lateral area and low thickness of phase-pure MCs relative to bulk SCs results in efficient collection of photogenerated carriers in low- and high-energy radiation detection. Furthermore, aspect-ratio-tuned 1D NWs exhibit high crystalline quality and large surface-to-volume ratios with low trap densities. They can be applied for polarized light detection due to large anisotropy in optical absorption and charge transport. Surface ligand binding dynamics play a crucial role in the device performance and long-term operation cycles of NCs. Relatively short ligands strongly adsorb onto the nanocrystalline surface, resulting in higher colloidal stability with the passivation of defects and efficient charge transport. Overall, this review demonstrates that $CsPbBr_3$ thin films, SCs, MCs and NCs enable unprecedented advantages in large-area and flexible next-generation optical detectors with potential applications in medical and industrial imaging as well as in consumer electronics. Nevertheless, there are still several points at

which the current state-of-the-art needs to be improved: (1) Inhomogeneous crystal morphologies of $CsPbBr_3$ nano-to-SCs, leading to poor charge transport, can be addressed by controlling the crystallization kinetics via surface treatment or solvent engineering. (2) Phase impurity engineering of Cs-Pb-Br systems (3D $CsPbBr_3$, 2D $CsPb_2Br_5$ and 0D Cs_4PbBr_6) can lead to a low leakage current by balancing charge carrier mobility and reducing ion migrations.[92] (3) Alkali metal substitution ($Cs_{1-x}M_yPbBr_3$ M: Rb^+) can positively affect the fundamental charge carrier dynamics, leading to an enhancement of carrier transport, which is beneficial for hard radiation detection.[121,38] Furthermore, europium doping has been shown to efficiently suppress the non-radiative recombination kinetics and enhance the PL lifetime,[122,123] or the introduction of an Eu^{3+}-Eu^{2+} ion pair as redox shuttle recovers metastable lead and halide atom defects during device fabrication and operation.[124] These novel compositional engineering needs to be investigated for $CsPbBr_3$ photodetectors towards long-term device operation stability. (4) Pinhole-free thick films with a smooth surface morphology can be fabricated at low-temperature by engineering the $CsPbBr_3$ nano-to-MCs within a conductive polymer matrix. (5) For high-energy X-ray and γ-ray detectors, the resistivity of the photoactive layers needs to be increased based on new material design to attain a low radiation detection limit.[5,42] The use of a thicker layer allows operation under high bias but can have an adverse effect on the dark current and operation stability due to ion migration. The implementation of high-quality single crystals, larger bandgap perovskites, metallic or doped graphene layers can overcome these issues. In general, improvements in dark current and spatial resolution can be achieved by optimizing the crystallinity, by understanding charge sharing between individual perovskite crystallites and by optimizing charge transfer at the device interfaces. (6) It has been demonstrated that light-induced lattice expansion of hybrid MHPs enhances solar sell performances.[125] Similarly, the effect of light exposure on the $CsPbBr_3$ photodetector device structures needs further investigation. (7) The recombination rates of photogenerated charge carriers in $CsPbBr_3$ NCs are high, leading to the low utilization of holes and electrons and thus, poor performance. This can be mitigated either by using bandgap aligned HTLs and ETLs,[21,102] by employing suitable small molecules[103] or solvents for efficient interfacial charge transfer. (8) Lead toxicity can be addressed by (partial) substitutions with environmentally friendly homovalent metal ions (e.g. Sn^{2+}, Ge^{2+}, Mn^{2+}), or a set of heterovalent metal ions (e.g. Ag^+ and Bi^{3+}), or by making a composite with lead-free perovskites such as $Cs_2AgBiBr_6$ or $Cs_3Bi_2Br_9$. At the same time, this can lead to enhanced photonic performance along with low detection limits.

1.9 References

(1) Brenner, T. M.; Egger, D. A.; Kronik, L.; Hodes, G.; Cahen, D. Hybrid Organic—Inorganic Perovskites: Low-Cost Semiconductors with Intriguing Charge-Transport Properties. *Nature Reviews Materials* **2016**, *1*, 15007.

(2) Kovalenko, M. V.; Protesescu, L.; Bodnarchuk, M. I. Properties and Potential Optoelectronic Applications of Lead Halide Perovskite Nanocrystals. *Science* **2017**, *358*, 745–750.

(3) Huang, H.; Pradhan, B.; Hofkens, J.; Roeffaers, M. B. J.; Steele, J. A. Solar-Driven Metal Halide Perovskite Photocatalysis: Design, Stability, and Performance. *ACS Energy Lett.* **2020**, *5*, 1107–1123.

(4) Bhatia, H.; Steele, J. A.; Martin, C.; Keshavarz, M.; Solis-Fernandez, G.; Yuan, H.; Fleury, G.; Huang, H.; Dovgaliuk, I.; Chernyshov, D.; Hendrix, J.; Roeffaers, M. B. J.; Hofkens, J.; Debroye, E. Single-Step Synthesis of Dual Phase Bright Blue-Green Emitting Lead Halide Perovskite Nanocrystal Thin Films. *Chem. Mater.* **2019**, *31*, 6824–6832.

(5) Zhou, Y.; Chen, J.; Bakr, O. M.; Mohammed, O. F. Metal Halide Perovskites for X-Ray Imaging Scintillators and Detectors. *ACS Energy Lett.* **2021**, 739–768.

(6) Wei, H.; Huang, J. Halide Lead Perovskites for Ionizing Radiation Detection. *Nature Communications* **2019**, *10*, 1066.

(7) Billen, P.; Leccisi, E.; Dastidar, S.; Li, S.; Lobaton, L.; Spatari, S.; Fafarman, A. T.; Fthenakis, V. M.; Baxter, J. B. Comparative Evaluation of Lead Emissions and Toxicity Potential in the Life Cycle of Lead Halide Perovskite Photovoltaics. *Energy* **2019**, *166*, 1089–1096.

(8) Kang, J.; Wang, L.-W. High Defect Tolerance in Lead Halide Perovskite CsPbBr3. *J. Phys. Chem. Lett.* **2017**, *8*, 489–493.

(9) Zhang, P.; Zhang, G.; Liu, L.; Ju, D.; Zhang, L.; Cheng, K.; Tao, X. Anisotropic Optoelectronic Properties of Melt-Grown Bulk CsPbBr3 Single Crystal. *J. Phys. Chem. Lett.* **2018**, *9*, 5040–5046.

(10) Zhou, H.; Zeng, J.; Song, Z.; Grice, C. R.; Chen, C.; Song, Z.; Zhao, D.; Wang, H.; Yan, Y. Self-Powered All-Inorganic Perovskite Microcrystal Photodetectors with High Detectivity. *J. Phys. Chem. Lett.* **2018**, *9*, 2043–2048.

(11) Li, X.; Yu, D.; Cao, F.; Gu, Y.; Wei, Y.; Wu, Y.; Song, J.; Zeng, H. Healing All-Inorganic Perovskite Films via Recyclable Dissolution–Recyrstallization for Compact and Smooth Carrier Channels of Optoelectronic Devices with High Stability. *Advanced Functional Materials* **2016**, *26*, 5903–5912.

(12) Zhai, W.; Lin, J.; Li, C.; Hu, S.; Huang, Y.; Yu, C.; Wen, Z.; Liu, Z.; Fang, Y.; Tang, C. Solvothermal Synthesis of Cesium Lead Halide Perovskite Nanowires with Ultra-High Aspect Ratios for High-Performance Photodetectors. *Nanoscale* **2018**, *10*, 21451–21458.

(13) Lin, Q.; Armin, A.; Burn, P. L.; Meredith, P. Near Infrared Photodetectors Based on Sub-Gap Absorption in Organohalide Perovskite Single Crystals. *Laser & Photonics Reviews* **2016**, *10*, 1047–1053.

(14) Song, J.; Xu, L.; Li, J.; Xue, J.; Dong, Y.; Li, X.; Zeng, H. Monolayer and Few-Layer All-Inorganic Perovskites as a New Family of Two-Dimensional Semiconductors for Printable Optoelectronic Devices. *Advanced Materials* **2016**, *28*, 4861–4869.

(15) Dou, L.; Yang, Y. (Micheal); You, J.; Hong, Z.; Chang, W.-H.; Li, G.; Yang, Y. Solution-Processed Hybrid Perovskite Photodetectors with High Detectivity. *Nat Commun* **2014**, *5*, 5404.

(16) Spina, M.; Lehmann, M.; Náfrádi, B.; Bernard, L.; Bonvin, E.; Gaál, R.; Magrez, A.; Forró, L.; Horváth, E. Microengineered CH3NH3PbI3 Nanowire/Graphene Phototransistor for Low-Intensity Light Detection at Room Temperature. *Small* **2015**, *11*, 4824-4828.

(17) Yuan, H.; Debroye, E.; Janssen, K.; Naiki, H.; Steuwe, C.; Lu, G.; Moris, M.; Orgiu, E.; Uji-i, H.; De Schryver, F.; Samorì, P.; Hofkens, J.; Roeffaers, M. Degradation of Methylammonium Lead Iodide Perovskite Structures through Light and Electron Beam Driven Ion Migration. *J. Phys. Chem. Lett.* **2016**, *7*, 561–566.

(18) Azpiroz, J. M.; Mosconi, E.; Bisquert, J.; Angelis, F. D. Defect Migration in Methylammonium Lead Iodide and Its Role in Perovskite Solar Cell Operation. *Energy Environ. Sci.* **2015**, *8*, 2118–2127.

(19) Kang, J.; Wang, L.-W. High Defect Tolerance in Lead Halide Perovskite CsPbBr3. *J. Phys. Chem. Lett.* **2017**, *8*, 489–493.

(20) Li, X.; Wu, Y.; Zhang, S.; Cai, B.; Gu, Y.; Song, J.; Zeng, H. CsPbX3 Quantum Dots for Lighting and Displays: Room-Temperature Synthesis, Photoluminescence Superiorities, Underlying Origins and White Light-Emitting Diodes. *Advanced Functional Materials* **2016**, *26*, 2435–2445.

(21) Liang, J.; Wang, C.; Wang, Y.; Xu, Z.; Lu, Z.; Ma, Y.; Zhu, H.; Hu, Y.; Xiao, C.; Yi, X.; Zhu, G.; Lv, H.; Ma, L.; Chen, T.; Tie, Z.; Jin, Z.; Liu, J. All-Inorganic Perovskite Solar Cells. *J. Am. Chem. Soc.* **2016**, *138*, 15829–15832.

(22) Hoffman, J. B.; Schleper, A. L.; Kamat, P. V. Transformation of Sintered CsPbBr3 Nanocrystals to Cubic CsPbI3 and Gradient CsPbBrxI3–x through Halide Exchange. *J. Am. Chem. Soc.* **2016**, *138*, 8603–8611.

(23) Ravi, V. K.; Scheidt, R. A.; DuBose, J.; Kamat, P. V. Hierarchical Arrays of Cesium Lead Halide Perovskite Nanocrystals through Electrophoretic Deposition. *J. Am. Chem. Soc.* **2018**, *140*, 8887–8894.

(24) Gualdrón-Reyes, Andrés. F.; Yoon, S. J.; Barea, E. M.; Agouram, S.; Muñoz-Sanjosé, V.; Meléndez, Á. M.; Niño-Gómez, M. E.; Mora-Seró, I. Controlling the Phase Segregation in Mixed Halide Perovskites through Nanocrystal Size. *ACS Energy Lett.* **2019**, *4*, 54–62.

(25) Pradhan, B.; Kumar, G. S.; Sain, S.; Dalui, A.; Ghorai, U. K.; Pradhan, S. K.; Acharya, S. Size Tunable Cesium Antimony Chloride Perovskite Nanowires and Nanorods. *Chem. Mater.* **2018**, *30*, 2135–2142.

(26) Li, Z.; Yang, M.; Park, J.-S.; Wei, S.-H.; Berry, J. J.; Zhu, K. Stabilizing Perovskite Structures by Tuning Tolerance Factor: Formation of Formamidinium and Cesium Lead Iodide Solid-State Alloys. *Chem. Mater.* **2016**, *28*, 284–292.

(27) He, Y.; Matei, L.; Jung, H. J.; McCall, K. M.; Chen, M.; Stoumpos, C. C.; Liu, Z.; Peters, J. A.; Chung, D. Y.; Wessels, B. W.; Wasielewski, M. R.; Dravid, V. P.; Burger, A.; Kanatzidis, M. G. High Spectral Resolution of Gamma-Rays at Room Temperature by Perovskite CsPbBr 3 Single Crystals. *Nat Commun* **2018**, *9*, 1609.

(28) Stoumpos, C. C.; Malliakas, C. D.; Peters, J. A.; Liu, Z.; Sebastian, M.; Im, J.; Chasapis, T. C.; Wibowo, A. C.; Chung, D. Y.; Freeman, A. J.; Wessels, B. W.; Kanatzidis, M. G. Crystal Growth of the Perovskite Semiconductor CsPbBr3: A New Material for High-Energy Radiation Detection. *Crystal Growth & Design* **2013**, *13*, 2722–2727.

(29) Rowlands, J. A. Material Change for X-Ray Detectors. *Nature* **2017**, *550*, 47–48.

(30) Kim, Y. C.; Kim, K. H.; Son, D.-Y.; Jeong, D.-N.; Seo, J.-Y.; Choi, Y. S.; Han, I. T.; Lee, S. Y.; Park, N.-G. Printable Organometallic Perovskite Enables Large-Area, Low-Dose X-Ray Imaging. *Nature* **2017**, *550*, 87–91.

(31) Palazon, F.; Urso, C.; De Trizio, L.; Akkerman, Q.; Marras, S.; Locardi, F.; Nelli, I.; Ferretti, M.; Prato, M.; Manna, L. Postsynthesis Transformation of Insulating Cs4PbBr6 Nanocrystals into Bright Perovskite CsPbBr3 through Physical and Chemical Extraction of CsBr. *ACS Energy Lett.* **2017**, *2*, 2445–2448.

(32) Saidaminov, M. I.; Almutlaq, J.; Sarmah, S.; Dursun, I.; Zhumekenov, A. A.; Begum, R.; Pan, J.; Cho, N.; Mohammed, O. F.; Bakr, O. M. Pure Cs4PbBr6: Highly Luminescent Zero-Dimensional Perovskite Solids. *ACS Energy Lett.* **2016**, *1*, 840–845.

(33) Wu, L.; Hu, H.; Xu, Y.; Jiang, S.; Chen, M.; Zhong, Q.; Yang, D.; Liu, Q.; Zhao, Y.; Sun, B.; Zhang, Q.; Yin, Y. From Nonluminescent Cs4PbX6 (X = Cl, Br, I) Nanocrystals to Highly Luminescent CsPbX3 Nanocrystals: Water-Triggered Transformation through a CsX-Stripping Mechanism. *Nano Lett.* **2017**, *17*, 5799–5804.

(34) Wang, H.; Kim, D. H. Perovskite-Based Photodetectors: Materials and Devices. *Chem. Soc. Rev.* **2017**, *46*, 5204–5236.

(35) Wang, Y.; Song, L.; Chen, Y.; Huang, W. Emerging New-Generation Photodetectors Based on Low-Dimensional Halide Perovskites. *ACS Photonics* **2020**, *7*, 10–28.

(36) Jin, H.; Debroye, E.; Keshavarz, M.; Scheblykin, I. G.; Roeffaers, M. B. J.; Hofkens, J.; Steele, J. A. It's a Trap! On the Nature of Localised

States and Charge Trapping in Lead Halide Perovskites. *Mater. Horiz.* **2020**, *7*, 397–410.

(37) Song, J.; Cui, Q.; Li, J.; Xu, J.; Wang, Y.; Xu, L.; Xue, J.; Dong, Y.; Tian, T.; Sun, H.; Zeng, H. Ultralarge All-Inorganic Perovskite Bulk Single Crystal for High-Performance Visible–Infrared Dual-Modal Photodetectors. *Advanced Optical Materials* **2017**, *5*, 1700157.

(38) Li, J.; Du, X.; Niu, G.; Xie, H.; Chen, Y.; Yuan, Y.; Gao, Y.; Xiao, H.; Tang, J.; Pan, A.; Yang, B. Rubidium Doping to Enhance Carrier Transport in CsPbBr3 Single Crystals for High-Performance X-Ray Detection. *ACS Appl. Mater. Interfaces* **2020**, *12*, 989–996.

(39) He, Y.; Liu, Z.; McCall, K. M.; Lin, W.; Chung, D. Y.; Wessels, B. W.; Kanatzidis, M. G. Perovskite CsPbBr3 Single Crystal Detector for Alpha-Particle Spectroscopy. *Nuclear Instruments and Methods in Physics Research Section A: Accelerators, Spectrometers, Detectors and Associated Equipment* **2019**, *922*, 217–221.

(40) Nitsch, K.; Hamplová, V.; Nikl, M.; Polák, K.; Rodová, M. Lead Bromide and Ternary Alkali Lead Bromide Single Crystals — Growth and Emission Properties. *Chemical Physics Letters* **1996**, *258*, 518–522.

(41) Clark, D. J.; Stoumpos, C. C.; Saouma, F. O.; Kanatzidis, M. G.; Jang, J. I. Polarization-Selective Three-Photon Absorption and Subsequent Photoluminescence in CsPbBr3 Single Crystal at Room Temperature. *Phys. Rev. B* **2016**, *93*, 195202.

(42) Kakavelakis, G.; Gedda, M.; Panagiotopoulos, A.; Kymakis, E.; Anthopoulos, T. D.; Petridis, K. Metal Halide Perovskites for High-Energy Radiation Detection. *Advanced Science* **2020**, *7*, 2002098.

(43) Rakita, Y.; Kedem, N.; Gupta, S.; Sadhanala, A.; Kalchenko, V.; Böhm, M. L.; Kulbak, M.; Friend, R. H.; Cahen, D.; Hodes, G. Low-Temperature Solution-Grown CsPbBr3 Single Crystals and Their Characterization. *Crystal Growth & Design* **2016**, *16*, 5717–5725.

(44) Dirin, D. N.; Cherniukh, I.; Yakunin, S.; Shynkarenko, Y.; Kovalenko, M. V. Solution-Grown CsPbBr3 Perovskite Single Crystals for Photon Detection. *Chem. Mater.* **2016**, *28*, 8470–8474.

(45) Cha, J.-H.; Han, J. H.; Yin, W.; Park, C.; Park, Y.; Ahn, T. K.; Cho, J. H.; Jung, D.-Y. Photoresponse of CsPbBr3 and Cs4PbBr6 Perovskite Single Crystals. *J. Phys. Chem. Lett.* **2017**, *8*, 565–570.

(46) Ding, J.; Du, S.; Zuo, Z.; Zhao, Y.; Cui, H.; Zhan, X. High Detectivity and Rapid Response in Perovskite CsPbBr3 Single-Crystal Photodetector. *J. Phys. Chem. C* **2017**, *121*, 4917–4923.

(47) Zhang, H.; Liu, X.; Dong, J.; Yu, H.; Zhou, C.; Zhang, B.; Xu, Y.; Jie, W. Centimeter-Sized Inorganic Lead Halide Perovskite CsPbBr3 Crystals Grown by an Improved Solution Method. *Crystal Growth & Design* **2017**, *17*, 6426–6431.

(48) Yang, Z.; Xu, Q.; Wang, X.; Lu, J.; Wang, H.; Li, F.; Zhang, L.; Hu, G.; Pan, C. Large and Ultrastable All-Inorganic CsPbBr3 Monocrystalline Films:

Low-Temperature Growth and Application for High-Performance Photodetectors. *Advanced Materials* **2018**, *30*, 1802110.

(49) Saidaminov, M. I.; Haque, M. A.; Almutlaq, J.; Sarmah, S.; Miao, X.-H.; Begum, R.; Zhumekenov, A. A.; Dursun, I.; Cho, N.; Murali, B.; Mohammed, O. F.; Wu, T.; Bakr, O. M. Inorganic Lead Halide Perovskite Single Crystals: Phase-Selective Low-Temperature Growth, Carrier Transport Properties, and Self-Powered Photodetection. *Advanced Optical Materials* **2017**, *5*, 1600704.

(50) Zhang, H.; Wang, F.; Lu, Y.; Sun, Q.; Xu, Y.; Zhang, B.-B.; Jie, W.; Kanatzidis, M. G. High-Sensitivity X-Ray Detectors Based on Solution-Grown Caesium Lead Bromide Single Crystals. *J. Mater. Chem. C* **2020**, *8*, 1248–1256.

(51) Xu, Q.; Wang, X.; Zhang, H.; Shao, W.; Nie, J.; Guo, Y.; Wang, J.; Ouyang, X. CsPbBr3 Single Crystal X-Ray Detector with Schottky Barrier for X-Ray Imaging Application. *ACS Appl. Electron. Mater.* **2020**, *2*, 879–884.

(52) Kearns, J. K. 2 - Silicon Single Crystals. In *Single Crystals of Electronic Materials*; Fornari, R., Ed.; Woodhead Publishing Series in Electronic and Optical Materials; Woodhead Publishing, 2019; pp 5–56.

(53) Yang, T.; Li, Y.; Han, S.; Xu, Z.; Liu, Y.; Zhang, X.; Liu, X.; Teng, B.; Luo, J.; Sun, Z. Highly-Anisotropic Dion–Jacobson Hybrid Perovskite by Tailoring Diamine into CsPbBr3 for Polarization-Sensitive Photodetection. *Small* **2020**, *16*, 1907020.

(54) Fu, D.; Wu, S.; Xin, J.; Zhang, X.; Han, G.; Zhang, X.-M. Polar CsPbBr3-Based Dion–Jacobson Hybrid for Promising UV Photodetection. *Chem. Commun.* **2020**, *56*, 14381-14384.

(55) Cheng, X.; Yuan, Y.; Jing, L.; Zhou, T.; Li, Z.; Peng, Z.; Yao, Q.; Zhang, J.; Ding, J. Nucleation-Controlled Growth of Superior Long Oriented CsPbBr3 Microrod Single Crystals for High Detectivity Photodetectors. *J. Mater. Chem. C* **2019**, *7*, 14188–14197.

(56) Tong, G.; Jiang, M.; Son, D.-Y.; Qiu, L.; Liu, Z.; Ono, L. K.; Qi, Y. Inverse Growth of Large-Grain-Size and Stable Inorganic Perovskite Micronanowire Photodetectors. *ACS Appl. Mater. Interfaces* **2020**, *12*, 14185–14194.

(57) Li, Y.; Shi, Z.; Lei, L.; Zhang, F.; Ma, Z.; Wu, D.; Xu, T.; Tian, Y.; Zhang, Y.; Du, G.; Shan, C.; Li, X. Highly Stable Perovskite Photodetector Based on Vapor-Processed Micrometer-Scale CsPbBr3 Microplatelets. *Chem. Mater.* **2018**, *30*, 6744–6755.

(58) Su, X.; Zhang, J.; Bai, G. Facile Synthesis and Characterization of CsPbBr3 and CsPb2Br5 Powders. *Bull Mater Sci* **2018**, *41*, 38.

(59) Yang, B.; Zhang, F.; Chen, J.; Yang, S.; Xia, X.; Pullerits, T.; Deng, W.; Han, K. Ultrasensitive and Fast All-Inorganic Perovskite-Based Photodetector via Fast Carrier Diffusion. *Advanced Materials* **2017**, *29*, 1703758.

(60) Zheng, W.; Xiong, X.; Lin, R.; Zhang, Z.; Xu, C.; Huang, F. Balanced Photodetection in One-Step Liquid-Phase-Synthesized CsPbBr3 Micro-/Nanoflake Single Crystals. *ACS Appl. Mater. Interfaces* **2018**, *10*, 1865–1870.

(61) Gui, P.; Chen, Z.; Li, B.; Yao, F.; Zheng, X.; Lin, Q.; Fang, G. High-Performance Photodetectors Based on Single All-Inorganic CsPbBr3 Perovskite Microwire. *ACS Photonics* **2018**, *5*, 2113–2119.

(62) Gu, Z.; Zhou, Z.; Huang, Z.; Wang, K.; Cai, Z.; Hu, X.; Li, L.; Li, M.; Zhao, Y. S.; Song, Y. Controllable Growth of High-Quality Inorganic Perovskite Microplate Arrays for Functional Optoelectronics. *Advanced Materials* **2020**, *32*, 1908006.

(63) Mo, X.; Li, X.; Dai, G.; He, P.; Sun, J.; Huang, H.; Yang, J. All-Inorganic Perovskite CsPbBr3 Microstructures Growth via Chemical Vapor Deposition for High-Performance Photodetectors. *Nanoscale* **2019**, *11*, 21386–21393.

(64) Pan, W.; Yang, B.; Niu, G.; Xue, K.-H.; Du, X.; Yin, L.; Zhang, M.; Wu, H.; Miao, X.-S.; Tang, J. Hot-Pressed CsPbBr3 Quasi-Monocrystalline Film for Sensitive Direct X-Ray Detection. *Advanced Materials* **2019**, *31*, 1904405.

(65) Zhou, H.; Song, Z.; Grice, C. R.; Chen, C.; Yang, X.; Wang, H.; Yan, Y. Pressure-Assisted Annealing Strategy for High-Performance Self-Powered All-Inorganic Perovskite Microcrystal Photodetectors. *J. Phys. Chem. Lett.* **2018**, *9*, 4714–4719.

(66) Matt, G. J.; Levchuk, I.; Knüttel, J.; Dallmann, J.; Osvet, A.; Sytnyk, M.; Tang, X.; Elia, J.; Hock, R.; Heiss, W.; Brabec, C. J. Sensitive Direct Converting X-Ray Detectors Utilizing Crystalline CsPbBr3 Perovskite Films Fabricated via Scalable Melt Processing. *Advanced Materials Interfaces* **2020,** *7*, 1901575.

(67) Feng, J.; Gong, C.; Gao, H.; Wen, W.; Gong, Y.; Jiang, X.; Zhang, B.; Wu, Y.; Wu, Y.; Fu, H.; Jiang, L.; Zhang, X. Single-Crystalline Layered Metal-Halide Perovskite Nanowires for Ultrasensitive Photodetectors. *Nature Electronics* **2018**, *1*, 404–410.

(68) Zhang, D.; Eaton, S. W.; Yu, Y.; Dou, L.; Yang, P. Solution-Phase Synthesis of Cesium Lead Halide Perovskite Nanowires. *J. Am. Chem. Soc.* **2015**, *137*, 9230–9233.

(69) Amgar, D.; Stern, A.; Rotem, D.; Porath, D.; Etgar, L. Tunable Length and Optical Properties of CsPbX3 (X = Cl, Br, I) Nanowires with a Few Unit Cells. *Nano Lett.* **2017**, *17*, 1007–1013.

(70) Zeng, J.; Zhou, H.; Liu, R.; Wang, H. Combination of Solution-Phase Process and Halide Exchange for All-Inorganic, Highly Stable CsPbBr3 Perovskite Nanowire Photodetector. *Sci. China Mater.* **2019**, *62*, 65–73.

(71) Oksenberg, E.; Sanders, E.; Popovitz-Biro, R.; Houben, L.; Joselevich, E. Surface-Guided CsPbBr3 Perovskite Nanowires on Flat and Faceted

Sapphire with Size-Dependent Photoluminescence and Fast Photoconductive Response. *Nano Lett.* **2018**, *18*, 424–433.

(72) Meng, Y.; Lan, C.; Li, F.; Yip, S.; Wei, R.; Kang, X.; Bu, X.; Dong, R.; Zhang, H.; Ho, J. C. Direct Vapor–Liquid–Solid Synthesis of All-Inorganic Perovskite Nanowires for High-Performance Electronics and Optoelectronics. *ACS Nano* **2019**, *13*, 6060–6070.

(73) Feng, J.; Yan, X.; Liu, Y.; Gao, H.; Wu, Y.; Su, B.; Jiang, L. Crystallographically Aligned Perovskite Structures for High-Performance Polarization-Sensitive Photodetectors. *Advanced Materials* **2017**, *29*, 1605993.

(74) Zhou, H.; Yuan, S.; Wang, X.; Xu, T.; Wang, X.; Li, H.; Zheng, W.; Fan, P.; Li, Y.; Sun, L.; Pan, A. Vapor Growth and Tunable Lasing of Band Gap Engineered Cesium Lead Halide Perovskite Micro/Nanorods with Triangular Cross Section. *ACS Nano* **2017**, *11*, 1189–1195.

(75) Wang, Y.; Sun, X.; Shivanna, R.; Yang, Y.; Chen, Z.; Guo, Y.; Wang, G.-C.; Wertz, E.; Deschler, F.; Cai, Z.; Zhou, H.; Lu, T.-M.; Shi, J. Photon Transport in One-Dimensional Incommensurately Epitaxial CsPbX3 Arrays. *Nano Lett.* **2016**, *16*, 7974–7981.

(76) Chen, J.; Fu, Y.; Samad, L.; Dang, L.; Zhao, Y.; Shen, S.; Guo, L.; Jin, S. Vapor-Phase Epitaxial Growth of Aligned Nanowire Networks of Cesium Lead Halide Perovskites (CsPbX3, X = Cl, Br, I). *Nano Lett.* **2017**, *17*, 460–466.

(77) Sun, M.; Fang, Q.; Zhang, Z.; Xie, D.; Sun, Y.; Xu, J.; Li, W.; Ren, T.; Zhang, Y. All-Inorganic Perovskite Nanowires–InGaZnO Heterojunction for High-Performance Ultraviolet–Visible Photodetectors. *ACS Appl. Mater. Interfaces* **2018**, *10*, 7231–7238.

(78) Shoaib, M.; Zhang, X.; Wang, X.; Zhou, H.; Xu, T.; Wang, X.; Hu, X.; Liu, H.; Fan, X.; Zheng, W.; Yang, T.; Yang, S.; Zhang, Q.; Zhu, X.; Sun, L.; Pan, A. Directional Growth of Ultralong CsPbBr3 Perovskite Nanowires for High-Performance Photodetectors. *J. Am. Chem. Soc.* **2017**, *139*, 15592–15595.

(79) Fu, Y.; Zhu, H.; Stoumpos, C. C.; Ding, Q.; Wang, J.; Kanatzidis, M. G.; Zhu, X.; Jin, S. Broad Wavelength Tunable Robust Lasing from Single-Crystal Nanowires of Cesium Lead Halide Perovskites (CsPbX3, X = Cl, Br, I). *ACS Nano* **2016**, *10*, 7963–7972.

(80) Meng, Y.; Lai, Z.; Li, F.; Wang, W.; Yip, S.; Quan, Q.; Bu, X.; Wang, F.; Bao, Y.; Hosomi, T.; Takahashi, T.; Nagashima, K.; Yanagida, T.; Lu, J.; Ho, J. C. Perovskite Core–Shell Nanowire Transistors: Interfacial Transfer Doping and Surface Passivation. *ACS Nano* **2020**, *14*, 12749–12760.

(81) Zhou, H.; Song, Z.; Grice, C. R.; Chen, C.; Zhang, J.; Zhu, Y.; Liu, R.; Wang, H.; Yan, Y. Self-Powered CsPbBr3 Nanowire Photodetector with a Vertical Structure. *Nano Energy* **2018**, *53*, 880–886.

(82) Cao, F.; Tian, W.; Deng, K.; Wang, M.; Li, L. Self-Powered UV–Vis–NIR Photodetector Based on Conjugated-Polymer/CsPbBr3 Nanowire Array. *Advanced Functional Materials* **2019**, *29*, 1906756.

(83) Wang, M.; Tian, W.; Cao, F.; Wang, M.; Li, L. Flexible and Self-Powered Lateral Photodetector Based on Inorganic Perovskite CsPbI3–CsPbBr3 Heterojunction Nanowire Array. *Advanced Functional Materials* **2020**, *30*, 1909771.

(84) Chen, J.-S.; Doane, T. L.; Li, M.; Zang, H.; Maye, M. M.; Cotlet, M. 0D–2D and 1D–2D Semiconductor Hybrids Composed of All Inorganic Perovskite Nanocrystals and Single-Layer Graphene with Improved Light Harvesting. *Particle & Particle Systems Characterization* **2018**, *35*, 1700310.

(85) Liu, H.; Zhang, X.; Zhang, L.; Yin, Z.; Wang, D.; Meng, J.; Jiang, Q.; Wang, Y.; You, J. A High-Performance Photodetector Based on an Inorganic Perovskite–ZnO Heterostructure. *J. Mater. Chem. C* **2017**, *5*, 6115–6122.

(86) Li, Y.; Shi, Z.-F.; Li, S.; Lei, L.-Z.; Ji, H.-F.; Wu, D.; Xu, T.-T.; Tian, Y.-T.; Li, X.-J. High-Performance Perovskite Photodetectors Based on Solution-Processed All-Inorganic CsPbBr3 Thin Films. *J. Mater. Chem. C* **2017**, *5*, 8355–8360.

(87) Zeng, J.; Li, X.; Wu, Y.; Yang, D.; Sun, Z.; Song, Z.; Wang, H.; Zeng, H. Space-Confined Growth of CsPbBr3 Film Achieving Photodetectors with High Performance in All Figures of Merit. *Advanced Functional Materials* **2018**, *28*, 1804394.

(88) De Roo, J.; Ibáñez, M.; Geiregat, P.; Nedelcu, G.; Walravens, W.; Maes, J.; Martins, J. C.; Van Driessche, I.; Kovalenko, M. V.; Hens, Z. Highly Dynamic Ligand Binding and Light Absorption Coefficient of Cesium Lead Bromide Perovskite Nanocrystals. *ACS Nano* **2016**, *10*, 2071–2081.

(89) Ramadan, A. J.; Ralaiarisoa, M.; Zu, F.; Rochford, L. A.; Wenger, B.; Koch, N.; Snaith, H. J. Revealing the Stoichiometric Tolerance of Lead Trihalide Perovskite Thin Films. *Chem. Mater.* **2020**, *32*, 114–120.

(90) Ji, Z.; Cen, G.; Su, C.; Liu, Y.; Zhao, Z.; Zhao, C.; Mai, W. All-Inorganic Perovskite Photodetectors with Ultrabroad Linear Dynamic Range for Weak-Light Imaging Applications. *Advanced Optical Materials* **2020**, *8*, 2001436.

(91) Fernandez-Izquierdo, L.; Reyes-Banda, M. G.; Mathew, X.; Chavez-Urbiola, I. R.; Bouanani, L. E.; Chang, J.; Avila-Avendano, C.; Mathews, N. R.; Pintor-Monroy, M. I.; Quevedo-Lopez, M. Cesium Lead Bromide (CsPbBr3) Thin-Film-Based Solid-State Neutron Detector Developed by a Solution-Free Sublimation Process. *Advanced Materials Technologies* **2020,** *5*, 2000534.

(92) Liu, R.; Zhang, J.; Zhou, H.; Song, Z.; Song, Z.; Grice, C. R.; Wu, D.; Shen, L.; Wang, H. Solution-Processed High-Quality Cesium Lead Bromine

Perovskite Photodetectors with High Detectivity for Application in Visible Light Communication. *Advanced Optical Materials* **2020**, *8*, 1901735.

(93) Protesescu, L.; Yakunin, S.; Bodnarchuk, M. I.; Krieg, F.; Caputo, R.; Hendon, C. H.; Yang, R. X.; Walsh, A.; Kovalenko, M. V. Nanocrystals of Cesium Lead Halide Perovskites (CsPbX3, X = Cl, Br, and I): Novel Optoelectronic Materials Showing Bright Emission with Wide Color Gamut. *Nano Lett.* **2015**, *15*, 3692–3696.

(94) Zhang, F.; Zhong, H.; Chen, C.; Wu, X.; Hu, X.; Huang, H.; Han, J.; Zou, B.; Dong, Y. Brightly Luminescent and Color-Tunable Colloidal CH3NH3PbX3 (X = Br, I, Cl) Quantum Dots: Potential Alternatives for Display Technology. *ACS Nano* **2015**, *9*, 4533–4542.

(95) Ramasamy, P.; Lim, D.-H.; Kim, B.; Lee, S.-H.; Lee, M.-S.; Lee, J.-S. All-Inorganic Cesium Lead Halide Perovskite Nanocrystals for Photodetector Applications. *Chem. Commun.* **2016**, *52*, 2067–2070.

(96) Lv, L.; Xu, Y.; Fang, H.; Luo, W.; Xu, F.; Liu, L.; Wang, B.; Zhang, X.; Yang, D.; Hu, W.; Dong, A. Generalized Colloidal Synthesis of High-Quality, Two-Dimensional Cesium Lead Halide Perovskite Nanosheets and Their Applications in Photodetectors. *Nanoscale* **2016**, *8*, 13589–13596.

(97) Bekenstein, Y.; Koscher, B. A.; Eaton, S. W.; Yang, P.; Alivisatos, A. P. Highly Luminescent Colloidal Nanoplates of Perovskite Cesium Lead Halide and Their Oriented Assemblies. *J. Am. Chem. Soc.* **2015**, *137*, 16008–16011.

(98) Shen, K.; Xu, H.; Li, X.; Guo, J.; Sathasivam, S.; Wang, M.; Ren, A.; Choy, K. L.; Parkin, I. P.; Guo, Z.; Wu, J. Flexible and Self-Powered Photodetector Arrays Based on All-Inorganic CsPbBr3 Quantum Dots. *Advanced Materials* **2020,** *32*, 2000004.

(99) Zhao, C.; Liu, Y.; Chen, L.; Li, J.; Fu, H. Y.; Zhao, S.; Li, W.-D.; Wei, G. Transparent CsPbBr3 Quantum Dot Photodetector with a Vertical Transistor Structure. *ACS Appl. Electron. Mater.* **2021**, *3*, 337–343.

(100) Liu, J.; Shabbir, B.; Wang, C.; Wan, T.; Ou, Q.; Yu, P.; Tadich, A.; Jiao, X.; Chu, D.; Qi, D.; Li, D.; Kan, R.; Huang, Y.; Dong, Y.; Jasieniak, J.; Zhang, Y.; Bao, Q. Flexible, Printable Soft-X-Ray Detectors Based on All-Inorganic Perovskite Quantum Dots. *Advanced Materials* **2019**, *31*, 1901644.

(101) Xin, B.; Alaal, N.; Mitra, S.; Subahi, A.; Pak, Y.; Almalawi, D.; Alwadai, N.; Lopatin, S.; Roqan, I. S. Identifying Carrier Behavior in Ultrathin Indirect-Bandgap CsPbX3 Nanocrystal Films for Use in UV/Visible-Blind High-Energy Detectors. *Small* **2020**, *16*, 2004513.

(102) DuBose, J. T.; Kamat, P. V. TiO2-Assisted Halide Ion Segregation in Mixed Halide Perovskite Films. *J. Am. Chem. Soc.* **2020**, *142*, 5362–5370.

(103) Sarkar, S.; Ravi, V. K.; Banerjee, S.; Yettapu, G. R.; Markad, G. B.; Nag, A.; Mandal, P. Terahertz Spectroscopic Probe of Hot Electron and Hole Transfer from Colloidal CsPbBr3 Perovskite Nanocrystals. *Nano Lett.* **2017**, *17*, 5402–5407.

(104) Chen, Y.; Chu, Y.; Wu, X.; Ou-Yang, W.; Huang, J. High-Performance Inorganic Perovskite Quantum Dot–Organic Semiconductor Hybrid Phototransistors. *Advanced Materials* **2017**, *29*, 1704062.

(105) Kwak, D.-H.; Lim, D.-H.; Ra, H.-S.; Ramasamy, P.; Lee, J.-S. High Performance Hybrid Graphene–CsPbBr3−xIx Perovskite Nanocrystal Photodetector. *RSC Adv.* **2016**, *6*, 65252–65256.

(106) Yu, Y.; Zhang, Y.; Song, X.; Zhang, H.; Cao, M.; Che, Y.; Dai, H.; Yang, J.; Zhang, H.; Yao, J. High Performances for Solution-Pocessed 0D–0D Heterojunction Phototransistors. *Advanced Optical Materials* **2017**, *5*, 1700565.

(107) Yang, Y.; Dai, H.; Yang, F.; Zhang, Y.; Luo, D.; Zhang, X.; Wang, K.; Sun, X. W.; Yao, J. All-Perovskite Photodetector with Fast Response. *Nanoscale Research Letters* **2019**, *14*, 291.

(108) Protesescu, L.; Yakunin, S.; Bodnarchuk, M. I.; Krieg, F.; Caputo, R.; Hendon, C. H.; Yang, R. X.; Walsh, A.; Kovalenko, M. V. Nanocrystals of Cesium Lead Halide Perovskites (CsPbX3, X = Cl, Br, and I): Novel Optoelectronic Materials Showing Bright Emission with Wide Color Gamut. *Nano Lett.* **2015**, *15*, 3692–3696.

(109) Dong, Y.; Gu, Y.; Zou, Y.; Song, J.; Xu, L.; Li, J.; Xue, J.; Li, X.; Zeng, H. Improving All-Inorganic Perovskite Photodetectors by Preferred Orientation and Plasmonic Effect. *Small* **2016**, *12*, 5622–5632.

(110) Li, X.; Yu, D.; Chen, J.; Wang, Y.; Cao, F.; Wei, Y.; Wu, Y.; Wang, L.; Zhu, Y.; Sun, Z.; Ji, J.; Shen, Y.; Sun, H.; Zeng, H. Constructing Fast Carrier Tracks into Flexible Perovskite Photodetectors To Greatly Improve Responsivity. *ACS Nano* **2017**, *11*, 2015–2023.

(111) Schwierz, F. Graphene Transistors. *Nature Nanotech* **2010**, *5*, 487–496.

(112) Konstantatos, G.; Badioli, M.; Gaudreau, L.; Osmond, J.; Bernechea, M.; Arquer, F. P. G. de; Gatti, F.; Koppens, F. H. L. Hybrid Graphene–Quantum Dot Phototransistors with Ultrahigh Gain. *Nature Nanotech* **2012**, *7*, 363–368.

(113) Guo, W.; Xu, S.; Wu, Z.; Wang, N.; Loy, M. M. T.; Du, S. Oxygen-Assisted Charge Transfer Between ZnO Quantum Dots and Graphene. *Small* **2013**, *9*, 3031–3036.

(114) Lee, Y.; Kwon, J.; Hwang, E.; Ra, C.-H.; Yoo, W. J.; Ahn, J.-H.; Park, J. H.; Cho, J. H. High-Performance Perovskite–Graphene Hybrid Photodetector. *Advanced Materials* **2015**, *27*, 41–46.

(115) Wang, Y.; Zhang, Y.; Lu, Y.; Xu, W.; Mu, H.; Chen, C.; Qiao, H.; Song, J.; Li, S.; Sun, B.; Cheng, Y.-B.; Bao, Q. Hybrid Graphene–Perovskite

Phototransistors with Ultrahigh Responsivity and Gain. *Advanced Optical Materials* **2015**, *3*, 1389–1396.

(116) Talapin, D. V.; Lee, J.-S.; Kovalenko, M. V.; Shevchenko, E. V. Prospects of Colloidal Nanocrystals for Electronic and Optoelectronic Applications. *Chem. Rev.* **2010**, *110*, 389–458.

(117) Che, Y.; Cao, X.; Zhang, Y.; Yao, J. High-Performance Photodetector Using CsPbBr3 Perovskite Nanocrystals and Graphene Hybrid Channel. *J Mater Sci* **2021**, *56*, 2341–2346.

(118) Song, X.; Liu, X.; Yu, D.; Huo, C.; Ji, J.; Li, X.; Zhang, S.; Zou, Y.; Zhu, G.; Wang, Y.; Wu, M.; Xie, A.; Zeng, H. Boosting Two-Dimensional MoS2/CsPbBr3 Photodetectors via Enhanced Light Absorbance and Interfacial Carrier Separation. *ACS Appl. Mater. Interfaces* **2018**, *10*, 2801–2809.

(119) Zhou, L.; Yu, K.; Yang, F.; Zheng, J.; Zuo, Y.; Li, C.; Cheng, B.; Wang, Q. All-Inorganic Perovskite Quantum Dot/Mesoporous TiO2 Composite-Based Photodetectors with Enhanced Performance. *Dalton Trans.* **2017**, *46*, 1766–1769.

(120) Zhou, L.; Yu, K.; Yang, F.; Cong, H.; Wang, N.; Zheng, J.; Zuo, Y.; Li, C.; Cheng, B.; Wang, Q. Insight into the Effect of Ligand-Exchange on Colloidal CsPbBr3 Perovskite Quantum Dot/Mesoporous-TiO2 Composite-Based Photodetectors: Much Faster Electron Injection. *J. Mater. Chem. C* **2017**, *5*, 6224–6233.

(121) Keshavarz, M.; Debroye, E.; Ottesen, M.; Martin, C.; Zhang, H.; Fron, E.; Küchler, R.; Steele, J. A.; Bremholm, M.; Vondel, J. V. de; Wang, H. I.; Bonn, M.; Roeffaers, M. B. J.; Wiedmann, S.; Hofkens, J. Tuning the Structural and Optoelectronic Properties of Cs2AgBiBr6 Double-Perovskite Single Crystals through Alkali-Metal Substitution. *Advanced Materials* **2020**, *32*, 2001878.

(122) Xiang, W.; Wang, Z.; Kubicki, D. J.; Tress, W.; Luo, J.; Prochowicz, D.; Akin, S.; Emsley, L.; Zhou, J.; Dietler, G.; Grätzel, M.; Hagfeldt, A. Europium-Doped CsPbI2Br for Stable and Highly Efficient Inorganic Perovskite Solar Cells. *Joule* **2019**, *3*, 205–214.

(123) Swarnkar, A.; Mir, W. J.; Nag, A. Can B-Site Doping or Alloying Improve Thermal- and Phase-Stability of All-Inorganic CsPbX3 (X = Cl, Br, I) Perovskites? *ACS Energy Lett.* **2018**, *3*, 286–289.

(124) Wang, L.; Zhou, H.; Hu, J.; Huang, B.; Sun, M.; Dong, B.; Zheng, G.; Huang, Y.; Chen, Y.; Li, L.; Xu, Z.; Li, N.; Liu, Z.; Chen, Q.; Sun, L.-D.; Yan, C.-H. A Eu3+-Eu2+ Ion Redox Shuttle Imparts Operational Durability to Pb-I Perovskite Solar Cells. *Science* **2019**, *363*, 265–270.

(125) Tsai, H.; Asadpour, R.; Blancon, J.-C.; Stoumpos, C. C.; Durand, O.; Strzalka, J. W.; Chen, B.; Verduzco, R.; Ajayan, P. M.; Tretiak, S.; Even, J.; Alam, M. A.; Kanatzidis, M. G.; Nie, W.; Mohite, A. D. Light-Induced Lattice Expansion Leads to High-Efficiency Perovskite Solar Cells. *Science* **2018**, *360*, 67–70.

Chapter 2
Motivation and Objectives

2.1 Motivation

In 1885, Physicist W.C. Röntgen made a groundbreaking discovery of a new kind of ray, which he named the "X-ray" due to its unknown nature at the time.[1] Ever since, X-rays have been a topic of ongoing research due to their remarkable ability to penetrate through various materials, including biological tissues, and their absorption or scattering behavior that varies depending on the density and composition of the material they encounter. These unique properties have led to widespread applications of X-rays in diverse fields such as medical diagnostics (e.g. mammography), material analysis (X-ray crystallography), airport security (luggage scanners) and art authentication (to verify the artist).[2] Among these applications, medical diagnostics holds the largest market share and is forecasted to show significant growth. The use of X-rays in non-destructive testing is witnessing an increasing demand, resulting in an expected market growth up to €3.8 Bn by 2027.[3] However, the rise in X-ray imaging has led to a more frequent accumulated exposure of X-rays to humans, which in turn increases radiation-related health risks.[4] To reduce the risks to the human body, extensive research to lower the necessary X-ray exposure for obtaining an image is fundamental. To minimize such exposure, continuous research is being performed to develop more sensitive X-ray detectors.[5-7]

Over the last decade, metal halide perovskites (MHPs) have emerged as a new class of semiconductor materials for optoelectronics.[5,8,9] In the quest for more sensitive materials to reduce the operating radiation dose, MHP-based X-ray detectors hold significant potential due to their unique physicochemical properties. First, MHPs have a high atomic number (high-Z), which is beneficial for efficient absorption of high-energy X-ray photons. Additionally, they exhibit high charge carrier generation and good charge transport characteristics, including high mobility and long charge carrier lifetime, which ensure a high charge collection efficiency. Furthermore, they are defect tolerant, which contributes to their ability to maintain high sensitivity and a high signal-to-noise ratio by keeping the dark current (a response produced in the absent of radiation under an applied bias) sufficiently low. Finally, perovskites offer the opportunity to move from indirect detectors, where a scintillator material is coupled to a photodetector, towards more sensitive direct conversion X-ray detectors that convert the X-rays directly in photo-charges. Compared to amorphous selenium (a-Se), the current market standard, Pb-based MHPs offer higher X-ray sensitivity, as well as cheaper and more convenient processing.[5,10–12]

However, Pb-based MHPs face significant challenges that hinder their commercial availability. One of the main obstacles is the long-term stability of the material. Pb-based MHPs can undergo phase transitions in response to changes in temperature, humidity, pressure and light irradiation.[11–13] As a result, they can exist both in true perovskite and non-perovskite structures. This poses a significant problem in producing device-quality materials, as the desirable optoelectronics are exhibited exclusively by the perovskite structure. Moreover, degradation related to ion migration under influence of light is problematic for their application as X-ray detectors.[8] Due to the high energy X-ray radiation and applied voltage, ionic defects are readily formed, resulting in prominent ion migration and thus an increase in dark current.[14] This leads to a low signal-to-noise ratio and compromises the device performance.[15–18]

Another challenge is the deposition of large-area MHP layers for device applications, as perovskite single crystals (SCs) with high-quality performance are typically small in size. During the development of these films, it is crucial to maintain the high-quality and stability achieved with SCs. Perovskite layers for devices are conventionally prepared by spin-coating precursor solutions, resulting in polycrystalline films with inherently high defect density.[19,20] The high amount of defects hinders further improvements in device efficiency by trapping of electrons and holes.[21]

In addition, the eco-toxicity of lead-containing perovskites is cited as hampering its future implementation in realistic devices. Although reports have downplayed the toxicity issue,[22] it is highly preferable to find Pb-free alternatives. One viable alternative to the lead halide perovskite are the so called double-perovskites $A_2BB'X_6$ (DP) obtained by replacing Pb^{2+} with heterovalent cation pairs, such as Ag^{+} and Bi^{3+}.[23–25] SCs have proven great response as X-ray detectors.[26] However, processability is important, as flat-panels X-ray detectors (FPDs) used in hospitals (e.g. 35 x 43 cm^2) are large, and the production of single crystals large enough to cover that area is very difficult. An alternative approach is to make high-quality perovskite nano/micro crystals and fabricate them into a dense, thick film.

2.2 Objectives of the Research

The general objective of this dissertation is to synthesize stable, phase-pure, highly crystalline perovskites that exhibit excellent photonic properties for their application as radiation detectors. The use of these materials is expected to enhance detection sensitivity and reduce risks to the human body upon X-ray exposure.

In the first part (Chapter 3) of this PhD dissertation, new synthesis and device fabrication methods will be developed to improve the stability of perovskite microcrystals. The existing state-of-the-art synthesis protocols for $CsPbBr_3$ will be further refined to achieve precise control over crystal purity. Moreover, the effect of introducing a secondary phase on degradation related to ion migration will be studied. Finally, a new strategy to fabricate a dense thick film under ambient conditions will described. To gain insights into the changes in structural and photophysical properties, various techniques such as X-ray diffraction (XRD), UV-Vis spectroscopy, steady-state and time-resolved photoluminescence spectroscopy and THz spectroscopy, will be employed. These techniques will provide valuable data on the structural integrity, optical properties, and dynamic behavior of the synthesized perovskite microcrystals, allowing for a detailed characterization and analysis of their performance as radiation detectors.

In the second part (Chapter 4), chemical vapor deposition (CVD) will be applied as an advanced synthesis strategy to fabricate high-quality and phase-pure $CsPbBr_3$ thin films. The phase-purity of the films will be verified using XRD, and the uniformity and coverage of the films will be investigated through scanning electron microscopy (SEM). The impact of the grain size on the carrier transport properties will also be examined through THz spectroscopy. Additionally, Rb-doping will be implemented to improve the performance of the films as photodetectors. Finally, the insights gained from this research will be utilized to optimize a home-built setup for the fabrication of $CsPbBr_3$ thin films, with the aim of expanding this strategy towards the controlled deposition of other (lead-free) perovskite materials in the future.

In the last part (Chapter 5), we aim to address the environmental concerns by exploring the (micro-)spectroscopic properties of lead-free, pure inorganic perovskites. We will fabricate high-quality perovskite microcrystals by performing structural transformation via ion exchange to overcome current shortcomings in quality when applying direct synthetic routes. The crystal lattice transformation will be followed through the synthesis of intermediates, which allows for an in-depth study of the changes in structural and optical

properties over time. To gain insights into the cation exchange process, a combination of techniques such as XRD, Raman spectroscopy, UV-Vis spectroscopy, and steady-state and time-resolved photoluminescence spectroscopy will be employed. This crystallographic transformation may pave pathway for the development of difficult-to-access perovskite structures, which are not available via direct solution-based synthesis pathways.

2.3 References

(1) M, T. Wilhelm Conrad Röntgen and the Discovery of X-Rays. *Bulletin de l'Academie nationale de medecine* **1996**, *180* (1).

(2) Szeles, C. CdZnTe and CdTe Materials for X-Ray and Gamma Ray Radiation Detector Applications. *physica status solidi (b)* **2004**, *241* (3), 783–790. https://doi.org/10.1002/pssb.200304296.

(3) *X-Ray Detectors Market Revenue Trends and Growth Drivers*. MarketsandMarkets. https://www.marketsandmarkets.com/Market-Reports/x-ray-detectors-market-7004984.html (accessed 2023-04-21).

(4) Lin, E. C. Radiation Risk From Medical Imaging. *Mayo Clinic Proceedings* **2010**, *85* (12), 1142–1146. https://doi.org/10.4065/mcp.2010.0260.

(5) Kasap, S. Low-Cost X-Ray Detectors. *Nature Photon* **2015**, *9* (7), 420–421. https://doi.org/10.1038/nphoton.2015.108.

(6) Datta, A.; Fiala, J.; Motakef, S. 2D Perovskite-Based High Spatial Resolution X-Ray Detectors. *Sci Rep* **2021**, *11* (1), 22897. https://doi.org/10.1038/s41598-021-02378-w.

(7) Kakavelakis, G.; Gedda, M.; Panagiotopoulos, A.; Kymakis, E.; Anthopoulos, T. D.; Petridis, K. Metal Halide Perovskites for High-Energy Radiation Detection. *Advanced Science* **2020**, *7* (22), 2002098. https://doi.org/10.1002/advs.202002098.

(8) Xu, W.; Niu, M.; Yang, X.; Chen, H.; Cai, X.; Smith, T. A.; Ghiggino, K. P.; Hao, X. Chemical Vapor Deposition Growth of Phase-Selective Inorganic Lead Halide Perovskite Films for Sensitive Photodetectors. *Chinese Chemical Letters* **2021**, *32* (1), 489–492. https://doi.org/10.1016/j.cclet.2020.05.017.

(9) Liang, J.; Wang, C.; Wang, Y.; Xu, Z.; Lu, Z.; Ma, Y.; Zhu, H.; Hu, Y.; Xiao, C.; Yi, X.; Zhu, G.; Lv, H.; Ma, L.; Chen, T.; Tie, Z.; Jin, Z.; Liu, J. All-Inorganic Perovskite Solar Cells. *J. Am. Chem. Soc.* **2016**, *138* (49), 15829–15832. https://doi.org/10.1021/jacs.6b10227.

(10) Tian, C.; Wang, F.; Wang, Y.; Yang, Z.; Chen, X.; Mei, J.; Liu, H.; Zhao, D. Chemical Vapor Deposition Method Grown All-Inorganic Perovskite Microcrystals for Self-Powered Photodetectors. *ACS Appl. Mater. Interfaces* **2019**, *11* (17), 15804–15812. https://doi.org/10.1021/acsami.9b03551.

(11) Yang, Y.; Hou, C.; Liang, T.-X. Energetic and Electronic Properties of CsPbBr3 Surfaces: A First-Principles Study. *Phys. Chem. Chem. Phys.* **2021**, *23* (12), 7145–7152. https://doi.org/10.1039/D0CP04893C.

(12) Klein, C. A. Bandgap Dependence and Related Features of Radiation Ionization Energies in Semiconductors. *Journal of Applied Physics* **2003**, *39* (4), 2029–2038. https://doi.org/10.1063/1.1656484.

(13) *The critical issue of using lead for sustainable massive production ...* Open Research Europe | Open Access Publishing Platform. https://doi.org/10.12688/openreseurope.13428.2.

(14) Chai, Y.; Juan, Z.; Wu, Y.; Liu, Y.; Li, X. Suppressing the Ion Migration in Halide Perovskite Wafers for Current-Drift Free X-Ray Detectors. *ACS Appl. Electron. Mater.* **2023**, *5* (1), 544–551. https://doi.org/10.1021/acsaelm.2c01597.

(15) Kovalenko, M. V.; Protesescu, L.; Bodnarchuk, M. I. Properties and Potential Optoelectronic Applications of Lead Halide Perovskite Nanocrystals. *Science* **2017**, *358* (6364), 745–750. https://doi.org/10.1126/science.aam7093.

(16) Wang, H.-C.; Bao, Z.; Tsai, H.-Y.; Tang, A.-C.; Liu, R.-S. Perovskite Quantum Dots and Their Application in Light-Emitting Diodes. *Small* **2018**, *14* (1), 1702433. https://doi.org/10.1002/smll.201702433.

(17) Kim, Y.; Yassitepe, E.; Voznyy, O.; Comin, R.; Walters, G.; Gong, X.; Kanjanaboos, P.; Nogueira, A. F.; Sargent, E. H. Efficient Luminescence from Perovskite Quantum Dot Solids. *ACS Appl. Mater. Interfaces* **2015**, *7* (45), 25007–25013. https://doi.org/10.1021/acsami.5b09084.

(18) Shamsi, J.; Rastogi, P.; Caligiuri, V.; Abdelhady, A. L.; Spirito, D.; Manna, L.; Krahne, R. Bright-Emitting Perovskite Films by Large-Scale Synthesis and Photoinduced Solid-State Transformation of CsPbBr3 Nanoplatelets. *ACS Nano* **2017**, *11* (10), 10206–10213. https://doi.org/10.1021/acsnano.7b04761.

(19) Kim, H.-S.; Lee, C.-R.; Im, J.-H.; Lee, K.-B.; Moehl, T.; Marchioro, A.; Moon, S.-J.; Humphry-Baker, R.; Yum, J.-H.; Moser, J. E.; Grätzel, M.; Park, N.-G. Lead Iodide Perovskite Sensitized All-Solid-State Submicron Thin Film Mesoscopic Solar Cell with Efficiency Exceeding 9%. *Sci Rep* **2012**, *2* (1), 591. https://doi.org/10.1038/srep00591.

(20) Burschka, J.; Pellet, N.; Moon, S.-J.; Humphry-Baker, R.; Gao, P.; Nazeeruddin, M. K.; Grätzel, M. Sequential Deposition as a Route to High-Performance Perovskite-Sensitized Solar Cells. *Nature* **2013**, *499* (7458), 316–319. https://doi.org/10.1038/nature12340.

(21) Nie, W.; Tsai, H.; Asadpour, R.; Blancon, J.-C.; Neukirch, A. J.; Gupta, G.; Crochet, J. J.; Chhowalla, M.; Tretiak, S.; Alam, M. A.; Wang, H.-L.; Mohite, A. D. Solar Cells. High-Efficiency Solution-Processed Perovskite Solar Cells with Millimeter-Scale Grains. *Science* **2015**, *347* (6221), 522–525. https://doi.org/10.1126/science.aaa0472.

(22) Hailegnaw, B.; Kirmayer, S.; Edri, E.; Hodes, G.; Cahen, D. Rain on Methylammonium Lead Iodide Based Perovskites: Possible Environmental Effects of Perovskite Solar Cells. *J. Phys. Chem. Lett.* **2015**, *6* (9), 1543–1547. https://doi.org/10.1021/acs.jpclett.5b00504.

(23) Babayigit, A.; Duy Thanh, D.; Ethirajan, A.; Manca, J.; Muller, M.; Boyen, H.-G.; Conings, B. Assessing the Toxicity of Pb- and Sn-Based

Perovskite Solar Cells in Model Organism Danio Rerio. *Sci Rep* **2016**, *6* (1), 18721. https://doi.org/10.1038/srep18721.

(24) Lehner, A. J.; Fabini, D. H.; Evans, H. A.; Hébert, C.-A.; Smock, S. R.; Hu, J.; Wang, H.; Zwanziger, J. W.; Chabinyc, M. L.; Seshadri, R. Crystal and Electronic Structures of Complex Bismuth Iodides A3Bi2I9 (A = K, Rb, Cs) Related to Perovskite: Aiding the Rational Design of Photovoltaics. *Chem. Mater.* **2015**, *27* (20), 7137–7148. https://doi.org/10.1021/acs.chemmater.5b03147.

(25) Volonakis, G.; Filip, M. R.; Haghighirad, A. A.; Sakai, N.; Wenger, B.; Snaith, H. J.; Giustino, F. Lead-Free Halide Double Perovskites via Heterovalent Substitution of Noble Metals. *J. Phys. Chem. Lett.* **2016**, *7* (7), 1254–1259. https://doi.org/10.1021/acs.jpclett.6b00376.

(26) Keshavarz, M.; Debroye, E.; Ottesen, M.; Martin, C.; Zhang, H.; Fron, E.; Küchler, R.; Steele, J. A.; Bremholm, M.; Van de Vondel, J.; Wang, H. I.; Bonn, M.; Roeffaers, M. B. J.; Wiedmann, S.; Hofkens, J. Tuning the Structural and Optoelectronic Properties of Cs2AgBiBr6 Double-Perovskite Single Crystals through Alkali-Metal Substitution. *Advanced Materials* **2020**, *32* (40), 2001878. https://doi.org/10.1002/adma.202001878.

Chapter 3
Phase-Engineering Compact and Flexible $CsPbBr_3$ Microcrystal Films for Robust X-ray Detection

This chapter is based on a manuscript (submitted) by:

Lotte Clinckemalie, Bapi Pradhan, Heng Zhang, Jonathan Vandenwijngaerden, Roel Vanden Brande, Dirk Vandenbroucke, Mischa Bonn, Hai I. Wang, Elke Debroye**

Author contributions:

L.C. conducted most of the experiments and their analysis, and wrote the manuscript under the supervision of B.P. and E.D. J.V. completed the time-resolved spectroscopy as well as the analysis. H.Z. performed THz measurements and analysis under the supervision of H.I.W. and M.B. L.C. and D.V. performed X-ray sensitivity measurements. The research line presented in the manuscript was conceived by E.D.

Situation in this PhD Dissertation

Pb-based MHPs have shown great promise as a semiconductor material for optoelectronics. However, their stability, processability as large-area layers and eco-toxicity have hampered their commercial usage. In this PhD dissertation, we investigated several ways to conquer these problems. This chapter focusses on the stability and large-area deposition of $CsPbBr_3$ thick films.

Abstract

All-inorganic $CsPbBr_3$ perovskites have gained significant attention due to their potential in direct X-ray detection. The fabrication of stable, pinhole-free thick films remains challenging, hindering their integration in durable, large-area high-resolution devices. In this study, we propose a facile strategy using a non-conductive polymer to create a flexible, compact thick film under ambient conditions. Furthermore, we investigate the effect of introducing the 2D $CsPb_2Br_5$ phase into $CsPbBr_3$ perovskite crystals on their photophysical properties and charge transport. Upon X-ray exposure, the devices consisting of the dual-phase exhibit improved stability and more effective operation at higher voltages. The lattice distortion due to the presence of the second phase presumably increases the ion migration energy barrier, resulting in a very low dark current and hence, enhanced stability. This feature might benefit local charge extraction and, ultimately, the X-ray image resolution. These findings also suggest that introducing a second phase in the perovskite structure can be advantageous for efficient photon-to-charge carrier conversion, as applied in medical imaging.

3.1 Introduction

Metal halide perovskite semiconductor materials have attracted significant attention owing to their exceptional optoelectronic properties, such as strong light absorption,[1] high carrier mobility,[2] and long electron-hole diffusion lengths.[3] Their low-cost fabrication, in combination with the ability to tune their optical and electronic properties through their compositional and morphological flexibility, have made diverse perovskite compounds the focus of intense study for different applications such as solar cells,[4] light emission applications (LEDs)[5,6] and photo- and X-ray detection.[7,8] X-ray detection is a crucial technology in many areas, such as medical imaging, industry and security screening, and material analysis.[9,10] Over the years, the soft X-ray industry is transitioning from indirect detectors, in which a scintillator material is coupled to a photodetector, to more sensitive direct-conversion X-ray detectors.[11] Most commercially available detectors are based on a semiconductor material, such as cadmium (zinc) telluride, or amorphous selenium (a-Se), which is currently used in mammography. However, the high cost and complex fabrication processes, or operational instability of these materials in combination with the low X-ray attenuation of a-Se constitute a significant bottleneck for their commercial usage.[12–16]

All-inorganic $CsPbBr_3$ perovskite has demonstrated high potential in this field due to its high X-ray attenuation coefficient arising from the high average atomic number combined with a high defect tolerance and good charge collection efficiency.[15,17–20] It exhibits an intermediate bandgap energy, which is advantageous compared to the high bandgap of $CsPbCl_3$. Additionally, it has an improved room temperature stability compared to $CsPbI_3$, which only exhibits its photoactive perovskite phase above 350 °C.[21–23] Despite its many advantages, several challenges need to be addressed before it can be fully commercialized for X-ray detection applications. One of the main obstacles is the stability of the material, as it is sensitive to moisture and heat and prone to degradation, promoting the formation of harmful defects and sacrificing the device performance.[24–27] Furthermore, high-quality, phase-pure $CsPbBr_3$ crystals are often synthesized via complex and prolonged synthesis methods, making it difficult to produce them on a large scale.[28–30] Finally, fabricating high-quality, thick perovskite films remains a great challenge, primarily due to the presence of numerous pinholes that often occur as a result of solvent evaporation in the typical solution-based processes.[19]

In this paper, we developed a facile, room-temperature microcrystal synthesis strategy without the need of ligands and with precise control over crystal purity. Furthermore, a compact, thick film was fabricated in ambient

conditions, using a polymer binder as a stabilizer. We show that control over the phase purity is a promising route to improve the stability of $CsPbBr_3$. More specifically, we investigated how introducing a secondary phase, e.g. two-dimensional (2D) $CsPb_2Br_5$, positively affects the structural and photophysical properties. Due to the presence of the $CsPb_2Br_5$ phase, shallow defects are formed in the material. While this effect somewhat reduces the charge carrier mobility, it results in a much-enhanced charge carrier lifetime. These properties lead to improved stability and operation at higher voltage regimes, which is expected to benefit charge extraction and can ultimately improve the X-ray image resolution. These findings suggest that introducing shallow defect levels in the perovskite lattice structure can benefit energy conversion applications.

3.2 Results and Discussion

To synthesize $CsPbBr_3$ microcrystals, a stoichiometric molar ratio of CsBr (5 mmol) and $PbBr_2$ (5 mmol) is first separately dissolved in 6 mL and 4 mL of 48 w% HBr, respectively, by sonication. These solutions are then added simultaneously and dropwise over 10 minutes to 1.5 mL of 48 w% HBr under ambient conditions and constant stirring. Finally, the crystals are centrifuged (5 min, 3500 rpm), washed with ethanol and vacuum dried at 60 °C. This results in icosahedral-shaped microcrystals with an average size of ~15 µm (Figure 1a). X-ray diffraction (XRD) confirms the formation of phase-pure orthorhombic $CsPbBr_3$ crystals (Figure 1b).[28] Upon slightly changing the synthesis procedure, we discovered the formation of a secondary phase after adding demi H_2O in a 1:4 volume ratio to the precursor mixture (for details, see SI). This results in microcrystals with a non-defined shape and an average size of ~10 µm (Figure 1c). XRD identifies the dual-phase sample to be consisting of both orthorhombic $CsPbBr_3$ and 2D tetragonal $CsPb_2Br_5$ crystal phases (Figure 1d, Figure S1).[28,31]

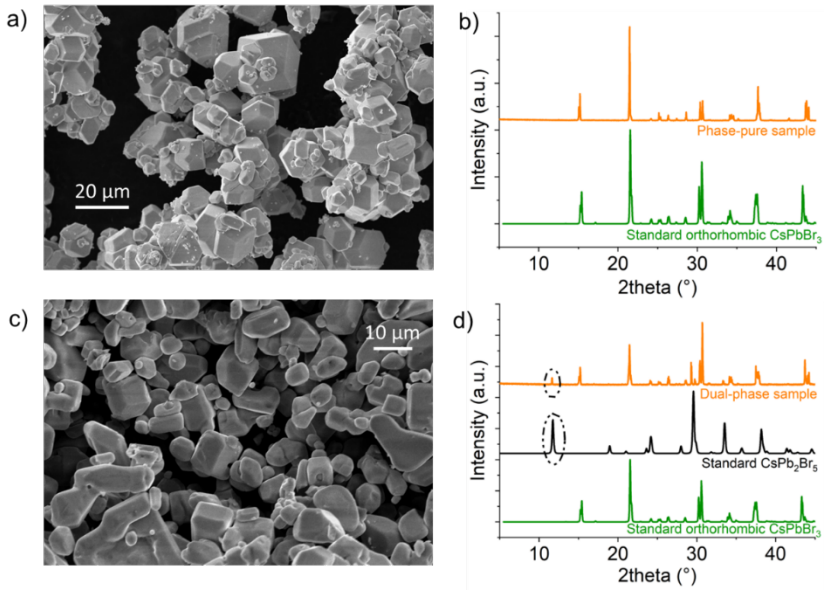

Figure 1. a) Scanning electron microscope (SEM) image of phase pure $CsPbBr_3$ microcrystals (MCs). b) XRD pattern revealing the phase-pure orthorhombic $CsPbBr_3$ crystal structure. c) SEM image of the dual-phase $CsPbBr_3$-$CsPb_2Br_5$ MCs. d) XRD pattern indicating the dual-phase $CsPbBr_3$-$CsPb_2Br_5$ crystal structure.

Towards scalable deposition for large-area X-ray detection devices, we developed a new strategy to create flexible and uniform thick films consisting of perovskite MCs. In this strategy, a non-conductive polymer is used to guarantee a dense crystal packing to assure good contact between the MC particles while inhibiting the generation of cracks. Devices of both samples are fabricated to compare their response to X-ray exposure. The sample holders are fabricated by attaching polyethylene terephthalate (PET) sheets on a conductive polyethylene naphtalate (PEN) substrate, which is precoated with indium tin oxide (ITO) to create a ~500 µm deep 1.5x1.5 cm^2 square cavity (Figure 2a). This is the desired thickness of a $CsPbBr_3$ film as it ensures that ~80% of X-ray photons with an energy of 50 keV are attenuated (Figure 2b). A 10 w% polyvinyl butyral (PVB) in isopropanol (IPA) is prepared as polymer binder solution. Next, a dispersion of 1 g of both the phase-pure and dual-phase perovskite microcrystals, 0.3 g of IPA and 0.3 g of the PVB polymer binder solution are mixed. Then, 0.3 g of this mixture is transferred into the square cavity so that it fully covers the entire surface. The films are

then allowed to harden under ambient conditions due to the partial evaporation of the solvent. Finally, the remaining solvent is removed by drying the films in an oven at 60 °C for one hour, resulting in the desired flexible, compact films with a smooth surface allowing good contact for opto-electric measurements (Figure 2a, Figure S2-S3).

As a proof-of-concept for X-ray detection, the devices are measured in PEN/ITO/perovskite/conductive silicone configuration. The distance between the X-ray source and the device is kept constant at 95 cm, mimicking a real-live X-ray imaging investigation. The generated current is probed in dark and while illuminated by an X-ray pulse (tungsten anode, 70 keV, 20 mA) under various bias voltages (V_{bias}). The photo-to-dark current (P/D) ratio is then plotted as a function of V_{bias} to determine the voltage at which the photocharges are most efficiently collected. A high P/D ratio of 750 is calculated for the phase-pure MCs at a V_{bias} of 1.6 V (Figure 2c). To assess the device performance, the detection sensitivity (R) is calculated by the following formula:

$$R = \frac{I_p - I_d}{D \cdot S}$$

Where I_p and I_d are the photocurrent and dark current, D is the X-ray dose rate and S is the effective area of the device (2.25 cm^2).[32,33] This results in a detection sensitivity of 22.05 µC Gy^{-1} cm^{-2} under a bias voltage of 4 V. The detection sensitivity is comparable to currently commercially available a-Se photodetectors.[12,34] On the other hand, the device is found to be unstable upon further increasing bias and degrades rapidly during the experiment, as highlighted by the fast decrease in P/D ratio. Due to the high energy X-ray radiation and applied voltage, a plausible scenario is that ionic defects are readily formed, resulting in prominent ion migration and, thus, an increase in dark current.[35] It has been demonstrated before that Br^- ions are released from the structure and migrate towards the positively biased electrode. This triggers degradation pathways and leads to a substantial decrease in charge collection.[36] As the increase in dark current is so dramatic, no photo-switching measurements could be performed for the phase-pure sample.

For the device fabricated out of dual-phase MCs, a sensitivity of 1.25 µC Gy^{-1} cm^{-2} at 4 V is measured. Interestingly, upon increasing the voltage to 20 V, the P/D ratio reaches 250 (Figure 2d), corresponding to a much-improved detection sensitivity of 15.42 µC Gy^{-1} cm^{-2}. While this value is slightly lower compared to the phase-pure MCs, we show that the existence of the secondary phase, belonging to the 2D $CsPb_2Br_5$, substantially enhances the operational stability and tolerance of $CsPbBr_3$ to higher voltage X-ray

detection. Working towards implementation in high-end devices, operation at higher voltages is expected to benefit charge extraction, and improved device stability in these regimes is strongly required. Moreover, charge carriers can diffuse laterally and spread over multiple device pixels, leading to information blur. By applying a higher voltage, the lateral diffusion of the charge carriers can be limited, reducing cross-talk between different pixels, and ultimately improving the X-ray image resolution.[12,37,38]

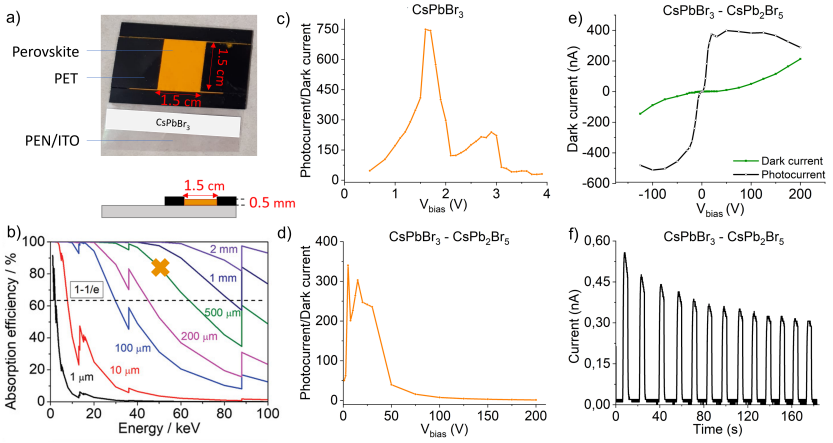

Figure 2. a) Photograph of a compact thick film fabricated by the proposed coating method on a conductive substrate (top) and a schematic diagram of the cross-section of the perovskite microcrystal film (bottom). Photo-to-dark current ratio upon X-ray exposure of b) Thickness-dependent absorption efficiency of $CsPbBr_3$ crystals.[39] c) phase-pure $CsPbBr_3$ and d) dual-phase $CsPbBr_3$-$CsPb_2Br_5$ films in function of the applied voltage. e) Dark current (green) and photocurrent (black) of the dual-phase film. f) Photo-switching measurements of the dual-phase film at an applied voltage of 5 V.

Studying the dual-phase MCs into more detail, it can be observed that the photocurrent exhibits a steep curve until a V_{bias} of 50 V, while the dark current remains low over that same range (Figure 2e). This means that even at high applied voltages, ion migration – which is the major cause of dark current – is substantially suppressed, which is generally a challenge for perovskite materials.[40,41] It has been proposed that the lattice distortion formed due to the presence of the second phase, when compared to the phase-pure $CsPbBr_3$ MCs, increases the ion migration energy barrier, resulting in a lower dark current.[42] Photo-switching measurements are performed at an applied voltage of 5 V to test the repeatability of the device response (Figure 2f). After 10 cycles, the generated photocurrent still equals 60% of the initially generated current. Notably, this is a proof-of-concept device, and further

optimization is needed to enhance the operation stability, which is beyond the scope of this work. However, this behavior confirms that the dual-phase $CsPbBr_3$-$CsPb_2Br_5$ is a promising material composite for X-ray detection with long-term operational stability, particularly at high voltages.

To comprehend the variation in X-ray response, the first crucial material property to consider is the energy required to create an electron-hole pair (W) upon X-ray illumination. This can be determined by the bandgap energy (E_g) using the equation $W = 2E_g + 1.43$.[43] To determine E_g, UV-Vis diffuse reflectance spectra of the phase-pure and dual-phase $CsPbBr_3$ MCs are measured, after which the corresponding absorbance values are calculated using the Kubelka-Munk theory. Tauc plots allow us to quantify and study the change in the bandgap energy (Figure 3). The results show that both the phase-pure and dual-phase crystals exhibit an absorption edge at 530 nm, corresponding to a direct bandgap of 2.3 eV, which agrees with the literature for phase-pure $CsPbBr_3$ crystals.[44] No clear difference between the phase-pure and dual-phase crystals can be seen at the absorption onset, as the contribution of the absorption edge and bandgap of the $CsPb_2Br_5$ phase is expected to be around 3.40 eV (365 nm) and is therefore hidden in the reflectance spectrum.[45]

Steady-state photoluminescence (PL) spectra are recorded to identify possible changes in the electronic states due to the introduction of the $CsPb_2Br_5$ phase. For the phase-pure $CsPbBr_3$ perovskite crystals, the steady-state PL spectra show two PL maxima at 530 nm (2.3 eV) and 550 nm (2.25 eV) (PLQY < 1%), with the first peak being the most intense (Figure 3a). Similar double-peak emission has already been observed in melt-grown $CsPbBr_3$ single crystals[28], as well as in solution-grown single $CsPbBr_3$ crystals[46]. The first PL peak almost coincides with the bandgap value of 2.30 eV and can therefore be attributed to near-band emission. However, the second PL peak exhibits a Stokes shift of 20 nm (0.09 eV). This can either be due to the existence of sub-bandgap states arising from defects or due to phonon-assisted processes.[47,48] For the dual-phase crystals, the same peaks can be observed, however the peak at 550 nm is more intense compared to the one at 530 nm (PLQY < 1%) (Figure 3b). This can be explained by Rashba splitting[49] or by the introduction of the second phase, which creates new defects in the perovskite lattice and therefore enhances the intensity of the second PL peak attributed to the radiative recombination through defect states.[50–52] To identify the exact cause of the PL peak splitting, further in-depth investigations are provided below.

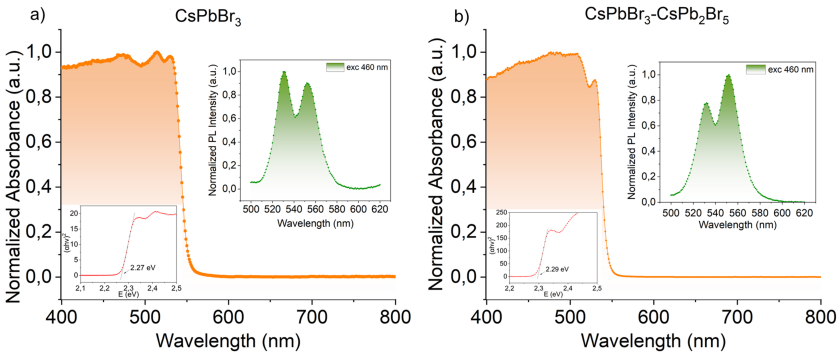

Figure 3. Absorption spectra of a) phase-pure $CsPbBr_3$ and b) dual-phase $CsPbBr_3$-$CsPb_2Br_5$. Tauc plots are shown in lower inset and steady-state PL spectra in upper inset.

The second crucial material property to consider is the charge carrier transport, as defined by the μτ-product, where μ is the carrier mobility and τ the fundamental carrier lifetime. To gain insight into the carrier lifetime, we performed time-resolved PL measurements in the ps-ns time range using time-correlated single photon counting (TCSPC) at different emission wavelengths. The PL decays of the phase-pure and dual-phase MCs (Figure 4a) can be fitted with three main components (Table S1). However, the complexity of the system does not allow us to indisputably assign each component to a specific process. Therefore, we proceed with a calculated average weighted lifetime $\langle\tau\rangle$, resulting in 1.44 ns for the phase-pure MCs and 3.28 ns for the dual-phase MCs, which is more than two times longer. For both samples, the decay associated spectra (DAS) (Figure 4b,c) show that their components contribute to the steady-state emission with different weights. In the phase-pure sample, the most dominant contribution arises from the 0.21 ns component, while the 2.16 ns component is more dominant for the dual-phase, resulting in the higher average weighted lifetime. This might be explained by the introduction of the 2D $CsPb_2Br_5$ structure, which is correlated with more defect states, as was already proposed in steady-state PL by the enhanced intensity of the second peak. Perovskite materials are generally defect tolerant, resulting in the formation of shallow (near the band edge) defect levels. These defects slow down the electron-hole recombination kinetics due to trapping and de-trapping, leading to longer lifetimes.[53–56] Furthermore, the DAS of the dual-phase MCs (Figure 4c) indicates that, over time, the relative contribution of the second peak associated with defects is decreasing, confirming the de-trapping process. We thus believe that, to some

extent, the formation of shallow defect levels in the perovskite lattice structure can be advantageous in applications for energy conversion, in particular from the perspective of charge carrier lifetime.

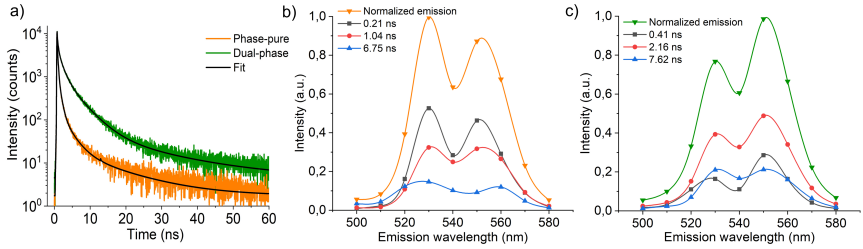

Figure 4. a) Time-resolved luminescence decay traces and their corresponding fit (black) of phase-pure MCs (orange) and dual-phase MCs (green) (λ_{exc} = 460 nm, λ_{em} = 530 nm). Decay associated spectra (DAS) resulting from TCSPC measurements of b) phase-pure MCs and c) dual-phase MCs (right).

To study the influence of the secondary phase on the electrical transport of $CsPbBr_3$ thin films, we conducted ultrafast and contact-free THz time-domain spectroscopy (THz-TDS) with sub-ps time resolution. In the optical pump-THz probe (OPTP) experiment, the perovskite thin film (with a typical thickness of 200 nm) was first photoexcited by an optical pulse (400 nm, ~100 fs pulse duration) to promote electrons from the valence band to the conduction band. Subsequently, a single-cycle THz pulse with electric field E transmits through the sample to probe the pump-induced change in the conductivity, i.e., photoconductivity $\Delta\sigma$. $\Delta\sigma$ is proportional to the relative attenuation of the THz electric field $-\Delta E/E_0$ ($\Delta E = E_{pump} - E_0$, with E_{pump} and E_0 being the transmitted THz electric field with and without photoexcitation, respectively).[57] By varying the pump-probe delay time t_P, the photoconductivity dynamics can be obtained. In principle, $\Delta\sigma$ is proportional to the product of photo-generated charge carrier density (N, N=$N_{abs}\varphi$, with N_{abs}= absorbed photon density and φ= the photon-to-free carrier quantum yield) and carrier mobility (μ), following: $\Delta\sigma = Ne\mu = (N_{abs}\varphi)e\mu$. In Figure 5a, we plot and compare the product of charge carrier mobility and photon-to-free carrier quantum yield $\varphi\mu$ (or equivalently $\Delta\sigma/(N_{abs}e)$) for both the $CsPbBr_3$ and $CsPbBr_3$- $CsPb_2Br_5$ thin films. The dual-phase MCs show ~24% decrease in the $\varphi\mu$ product when compared to that of phase-pure $CsPbBr_3$ samples. To further investigate which change (e.g., mobility or free carrier density) dominates the reduced μφ, we measured the frequency-resolved photoconductivity spectra by Fourier-transforming the time-domain THz field

$\Delta E(t)$ and $E_0(t)$, at the same incident pump fluence. The obtained spectra in Figure 5b can be adequately described by the Drude-Smith model:[58]

$$\Delta\sigma(\omega) = \frac{\omega_p^2 \varepsilon_0 \tau_s}{1 - i\omega\tau}\left(1 + \frac{c}{1 - i\omega\tau}\right)$$

This model describes the free carrier transport with a preferential backscattering from e.g. the grain boundary. Here, parameter c ($-1 < c < 0$) is introduced to account for the extent of backscattering. For $c = -1$, the charge carriers experience 100% backscattering, while for $c = 0$, the Drude-Smith model is simplified to the Drude model. ω_p is the plasma frequency which is directly related to the carrier density N through $\omega_p = \sqrt{\frac{N}{\varepsilon_0 \cdot m^*}}e$ (m^* is the effective mass), ε_0 the vacuum permittivity, τ_s the scattering time and ω the angular frequency. From the fitting, we extract nearly the same plasma frequency and parameter c for both samples (62.1 $\pm$ 1.1 THz and -0.68 $\pm$ 0.01 for $CsPbBr_3$, 60.7 $\pm$ 3.6 THz and -0.69 $\pm$ 0.01 for $CsPbBr_3$-$CsPb_2Br_5$), while the scattering time of $CsPbBr_3$-$CsPb_2Br_5$ (51 $\pm$ 5 fs) is ~30% lower than that of $CsPbBr_3$ (73 $\pm$ 2 fs). When considering the mobility at the dc limit ($\mu = \frac{e\tau}{m^*}(1 + c)$), the reduction of charge mobility in $CsPbBr_3$-$CsPb_2Br_5$ mainly originates from the enhanced scattering rate (=1/scattering time).

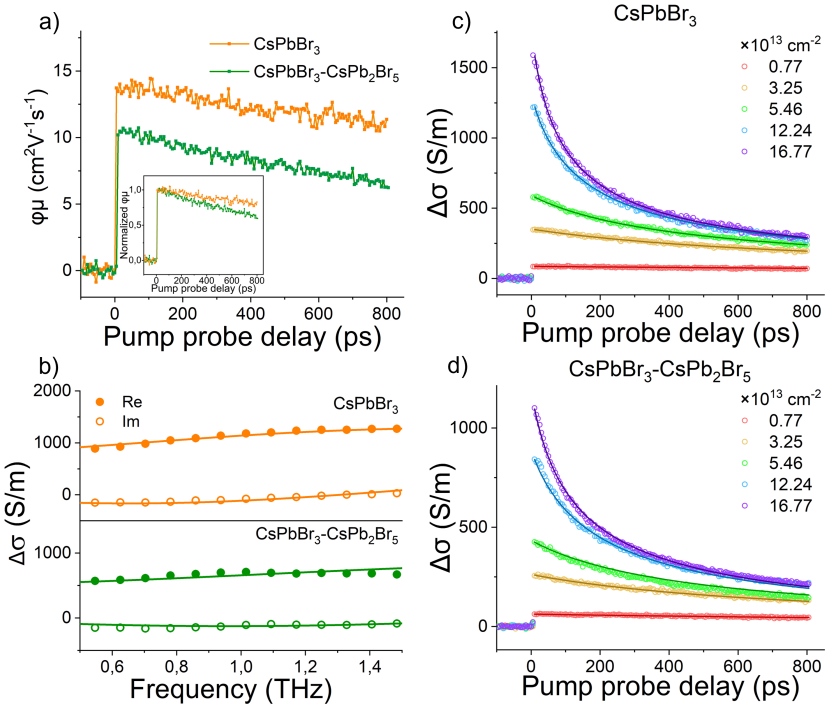

Figure 5. a) Comparison of photoconductivity dynamics at an incident pump photon density of 0.77×10^{13} cm^{-2}. Inset shows the normalized dynamics. b) Frequency-resolved photoconductivity spectra for the phase-pure and dual-phase MCs, measured at pump-probe delay time of 5 ps and at the incident pump photon density of 1×10^{14} cm^{-2}. Fluence-dependent OPTP dynamics of c) phase-pure and d) dual-phase MCs. All the measurements are conducted using an excitation wavelength of 400 nm at room temperature in dry nitrogen atmosphere.

Table 1. Recombination rate constants of phase-pure and dual-phase MCs.

Sample	k_1 (s^{-1})	k_2 (cm^3s^{-1})	k_3 (cm^6s^{-1})
$CsPbBr_3$	4.09×10^{7}	3.70×10^{-10}	6.75×10^{-28}
$CsPbBr_3$ - $CsPb_2Br_5$	2.30×10^{8}	4.57×10^{-10}	6.75×10^{-28}

To gain further insights on the charge transport properties, we conducted fluence-dependent OPTP dynamics for both samples, and globally fitted them by the coupled rate equation for recombinations:[59]

$$\frac{dn(t)}{dt} = -k_1 \cdot n - k_2 \cdot n^2 - k_3 \cdot n^3$$

in which $n(t)$ is the time-dependent carrier density. Here we assume the decay in the photoconductivity stems from the recombination, e.g. decay in the charge carrier population *n*, which should be valid for beyond-ps dynamics where charge carriers are expected to relax to the band edge. k_1 is the monomolecular recombination rate constant which arises from charge trapping; k_2 represents the bimolecular recombination rate constant which represents the free electron-hole pair recombination, and k_3 stands for the Auger recombination rate constant. The first-order recombination is expected to strongly depend on the phase composition, and to increase for less pure phases, due to the likely reduced domain sizes and introduced defect states. The higher-order recombinations, on the other hand, mostly depend on local charge carrier densities, and are therefore much less susceptible to the details of the sample composition. Indeed, as shown in Table 1, k_2 and k_3 are comparable for both samples, however, a significant difference in k_1 is observed, suggesting a higher density of defect states in $CsPbBr_3$-$CsPb_2Br_5$. In line with our speculation and both static and time-resolved PL, introducing a lower dimensional side phase ($CsPb_2Br_5$) seems to induce additional shallow defect states, contributing to a prolonged lifetime, while to some extent reducing the charge mobility. This can be advantageous in high-voltage X-ray detection as it prevents excess charges from accumulating at the selective contacts.[60] Furthermore, the dual-phase MCs exhibit a low dark current in X-ray detection measurements, suggesting a suppressed ion migration by increasing the ion migration energy barrier.[42] All these aspects avoid the building up of unwanted polarization in the device configuration,[36] resulting in an improved local charge extraction.

3.3 Conclusion

In this work, we have demonstrated a scalable deposition method for creating uniform, crack-free, and flexible films consisting of perovskite MCs. Furthermore, we investigated how the implementation of the 2D $CsPb_2Br_5$ phase into $CsPbBr_3$ microcrystals affects their structural and optical properties. Corresponding proof-of-concept devices were tested for

sensitivity upon X-ray illumination, and it was found that the dual-phase sample demonstrated improved X-ray detection at higher voltage regimes. This improved stability provides a promising avenue for future improvements in fast, local charge extraction and X-ray image resolution. Time-resolved photoluminescence measurements revealed a prolonged lifetime of the dual-phase sample due to the presence of shallow defects that slow down electron-hole recombination kinetics. THz measurements confirmed the presence of additional defects, as indicated by the slightly reduced carrier mobility. This is beneficial at higher voltages as it prevents the accumulation of an excess of charges at the contacts. Moreover, the dual-phase $CsPbBr_3$-$CsPb_2Br_5$ MCs exhibit a much lower dark current, linked to suppressed ion migration, which, in combination with the formed defect states, prevents the building up of polarization in the device configuration. These findings suggest that the introduction of shallow defects may not be as detrimental as expected and could potentially serve as an effective means to optimize X-ray detection, as well as other high-voltage demanding energy conversion applications.

This PhD chapter proves that the mixed $CsPbBr_3$-$CsPb_2Br_5$ is an excellent material for X-ray detection. Furthermore, it can easily be fabricated in a thick, large-area layer using a newly proposed polymer-based deposition method. However, research on polymer-free deposition methods is still highly preferable, as polymers might hamper charge extraction. Therefore, exploring the potential of chemical vapor deposition could be an interesting pathway to pursue, which is will be the main focus in Chapter 4.

3.4 Supporting Information

3.4.1 Experimental Section

Material synthesis: All precursor chemicals were obtained commercially from either Alfa Aesar (CsBr, 99%), Thermo Scientific (HBr, pure, 48 w%) or Sigma-Aldrich ($PbBr_2$, 98%) without any further purification. The $CsPbBr_3$-$CsPb_2Br_5$ microcrystals are synthesized by first separately dissolving a stoichiometric molar ratio of CsBr (5 mmol) and $PbBr_2$ (5 mmol) in respectively 1 mL of demi H_2O and 4 mL of 48 w% HBr by sonication. The Cs-H_20 solution is then dropwise added over 10 minutes to the Pb-HBr solution under ambient conditions and constant stirring. Finally, the crystals are centrifuged (5 min, 3500 rpm), washed with ethanol and vacuum dried at 60 °C.

Thin films for THz measurements were prepared by spin-coating a 0.5 M DMSO solution of both the dual-phase and phase-pure MCs. The solutions were prepared by dissolving 0.290 g of the MCs in 1 mL of dry DMSO at around 70 °C. The solution was then filtered with a 0.20 µL pore PTFE hydrophilic filter. For obtaining the thin film, 70 µL of the perovskite solution was spin-coated on the fused silica glass, in a glovebox. Subsequent spin-coating at 1000 rpm for 10 s, followed by 60 s at 3000 rpm, with the addition of 125 µL of chlorobenzene 35 s before the end of the program, resulted in the desired thin film after solvent evaporation (for 10 min on a hot plate at 60 °C). Both of the films were annealed outside the glovebox for 30 min at 150 °C. The films were stored in the dark under an inert atmosphere until further measurements.

3.4.2 Material Characterization

Scanning electron microscopy (SEM) was used to obtain images of the crystals. They were recorded on a FEI-Q FEG250 instrument.

X-ray diffraction (XRD) patterns were obtained on a Malvern PANalytical Empyrean diffractometer, equipped with a PIXcel3D solid-state detector using a Cu anode (Cu $K_{\alpha1}$: 1.5406 Å; Cu $K_{\alpha2}$: 1.5444 Å). The powder samples were loaded onto a 96-well sample holder and X-ray diffractograms were recorded at room temperature in a transmission geometry within a 1.3 – 45° 2θ range using a step size of 0.013°.

X-ray detection measurements were performed by exposing the devices for 30 seconds to a Pantak-Seifert X-ray source with tungsten anode (maximum X-ray photon energy 70 keV, peak intensity 30 keV) in the configuration of PEN/ITO/perovskite/conductive silicone. The X-ray spot size was about 3 mm and the X-ray dose rate was carefully calibrated with a RaySafe Model Solo R/F dosimeter. A Keithley 2000 was used to apply the bias voltage and to record both the dark- and response current. All the X-ray response characterization was conducted in the dark.

***In situ* UV–Vis Diffuse Reflectance** data were recorded between 400 and 800 nm with a step of 1 nm via a PerkinElmer Lambda 950 UV−vis spectrophotometer equipped with an integrating sphere at ambient temperature. $BaSO_4$ powder was used as reference. The diffused reflectance (R) was converted to F(R) using the Kubelka−Munk function: $F(R) = (1 - R)^2/2R$.

Steady-state photoluminescence (PL) excitation-emission maps were measured with an excitation range between 250 nm and 600 nm with a step of 5 nm and an emission range between 300 and 800 nm with a step of 5 nm via an Edinburgh FLS980 fluorimeter.

Time-correlated single photon counting (TCSPC) was used to determine the fluorescence decay times at the nanosecond time scale. The frequency-tripled output (266 nm, 8.18 MHz, 2 ps FWHM) of a mode-locked Ti:Sapphire laser (Tsunami, Spectra Physics) was used as excitation source. The linearly polarized excitation light was rotated to a vertical direction by the use of a Berek compensator (New Focus) in combination with a polarization filter and directed onto the samples. The samples in powder form were placed in a quartz cuvette (1 mm path length), sealed by a Teflon stopper, and then mounted on the device. The emission was collected under 90° with respect to the incident light and guided through a polarization filter that was set at the magic angle (54.7°) with respect to the polarization of the excitation beam. The fluorescence was spectrally resolved by a monochromator (Sciencetech 9030, 100 nm focal length, wave- length accuracy 0.3 nm), and detected by a microchannel plate photomultiplier tube (MCP-PMT, R3809U-51, Hamamatsu). A time-correlated single photon timing PC module (SPC 830, Becker & Hickl) was used to obtain the fluorescence decay histogram in 4096 channels. The decays were recorded with 10000 counts in the peak channel, in time windows of 12 ns corresponding to 2.92 ps per channel and analyzed individually with a time-resolved fluorescence analysis (TRFA) software based on iterative reconvolution of the data with the instrumental response function (IRF). The full width at half- maximum (FWHM) of the IRF was typically in the order of 42 ps.

Terahertz photoconductivity measurements provide a contact-free means for photoconductivity measurements. Using an ultrashort visible laser pulse (400 nm, FWHM ≈ 50 fs), charge carriers were optically injected into the conduction bands. Subsequently, the conductivity of the photogenerated charge carrier was probed by freely propagating single-cycle THz electromagnetic transients with 1–2 ps duration. The quickly oscillating terahertz field E(t) accelerated the charges, which, in turn, modifies the terahertz pulse. The relative modification $-\Delta E/E(t)$ of the THz field can be directly measured and related to the photoconductivity σ. The analysis was typically performed in the frequency domain by Fourier transformation, that is, $\sigma(\omega) \approx -\Delta E/E(\omega)$. The photoconductivity as a function of time delay t_d between excitation and THz pulse $\sigma(\omega;t_d)$ was a complex value, and its real part, $Re[\sigma(\omega;t_d)]$, corresponding to the changes in the peak intensity of THz

pulse following photoexcitation, was directly related to the macroscopic transport parameters in electrical measurements, by $Re[\sigma(\omega ; t_d)] = N_{pump} \times e \times \mu(\omega ; t_d)$ where N_{pump} and $\mu(\omega; t_d)$ were the time-dependent carrier density and mobility following photoexcitation, respectively. Terahertz spectroscopy thus provides information on charge carrier dynamics on a timescale complementary to that obtained using time-resolved PL measurements (sub-ps versus ns).

3.4.3 Supporting Information for Results and Discussion

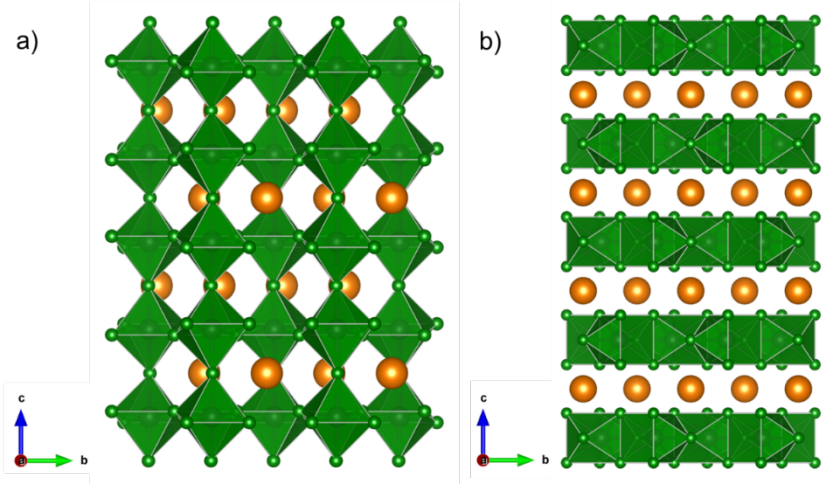

Figure S1. Illustration of the crystal structures of a) orthorhombic $CsPbBr_3$ and b) (2D) tetragonal $CsPb_2Br_5$.

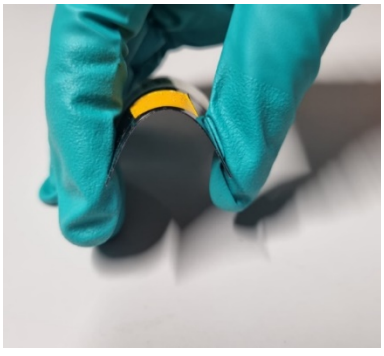

Figure S2. Photograph of a compact thick film fabricated in the lab, showing its flexibility.

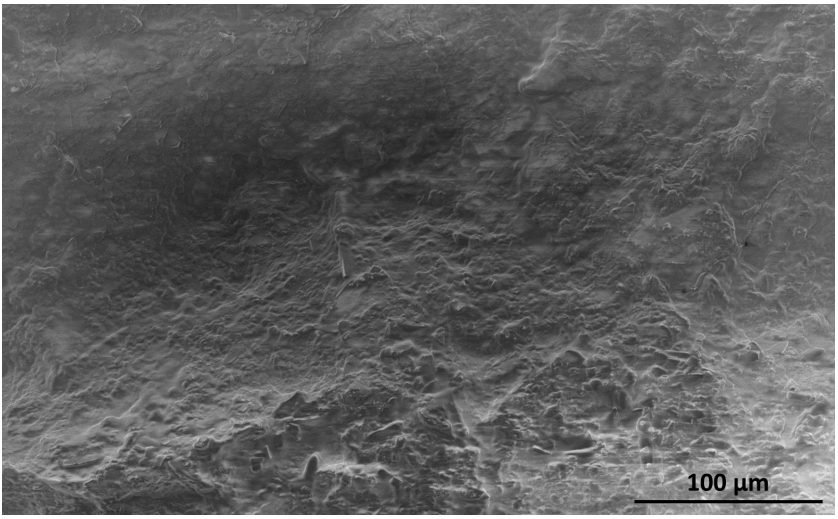

Figure S3. Scanning electron microscopy (SEM) image of the compact $CsPbBr_3$ film.

Table S1. Time components of the luminescence decay (λ_{exc} = 460 nm, λ_{em} = 530 nm) of the phase-pure and dual-phase MCs as fitted by a global analysis. It should be noted that the value of τ_1 (0.030 ns) is lower than the resolution of the instrument (0.042 ns) and is thus disregarded during further examination of the decays.

Time components	Phase-pure MCs	Dual-phase MCs
τ_1	0.030 ns	0.030 ns
τ_2	0.21 ns (**52.8%** contribution)	0.41 ns (21.4% contribution)
τ_3	1.04 ns (32.5% contribution)	2.16 ns (**51.2%** contribution)
τ_4	6.75 ns (14.7% contribution)	7.62 ns (27.4% contribution)

3.5 References

(1) Liu, D.; Kelly, T. L. Perovskite Solar Cells with a Planar Heterojunction Structure Prepared Using Room-Temperature Solution Processing Techniques. *Nature Photon* **2014**, *8* (2), 133–138. https://doi.org/10.1038/nphoton.2013.342.

(2) Wei, H.; Fang, Y.; Mulligan, P.; Chuirazzi, W.; Fang, H.-H.; Wang, C.; Ecker, B. R.; Gao, Y.; Loi, M. A.; Cao, L.; Huang, J. Sensitive X-Ray Detectors Made of Methylammonium Lead Tribromide Perovskite Single Crystals. *Nature Photonics* **2016**, *10* (5), 333–340. https://doi.org/10.1038/NPHOTON.2016.41.

(3) Jiang, Q.; Zhang, L.; Wang, H.; Yang, X.; Meng, J.; Liu, H.; Yin, Z.; Wu, J.; Zhang, X.; You, J. Enhanced Electron Extraction Using SnO2 for High-Efficiency Planar-Structure HC(NH2)2PbI3-Based Perovskite Solar Cells. *Nature Energy* **2017**, *2*, 16177. https://doi.org/10.1038/nenergy.2016.177.

(4) Mahmud, M. A.; Duong, T.; Peng, J.; Wu, Y.; Shen, H.; Walter, D.; Nguyen, H. T.; Mozaffari, N.; Tabi, G. D.; Catchpole, K. R.; Weber, K. J.; White, T. P. Origin of Efficiency and Stability Enhancement in High-Performing Mixed Dimensional 2D-3D Perovskite Solar Cells: A Review. *Advanced Functional Materials* **2022**, *32* (3), 2009164. https://doi.org/10.1002/adfm.202009164.

(5) Bhatia, H.; Ghosh, B.; Debroye, E. Colloidal FAPbBr3 Perovskite Nanocrystals for Light Emission: What's Going On? *J. Mater. Chem. C* **2022**. https://doi.org/10.1039/D2TC01373H.

(6) Van Le, Q.; Jang, H. W.; Kim, S. Y. Recent Advances toward High-Efficiency Halide Perovskite Light-Emitting Diodes: Review and Perspective. *Small Methods* **2018**, *2* (10), 1700419. https://doi.org/10.1002/smtd.201700419.

(7) Clinckemalie, L.; Valli, D.; Roeffaers, M. B. J.; Hofkens, J.; Pradhan, B.; Debroye, E. Challenges and Opportunities for CsPbBr3 Perovskites in Low- and High-Energy Radiation Detection. *ACS Energy Lett.* **2021**, *6* (4), 1290–1314. https://doi.org/10.1021/acsenergylett.1c00007.

(8) Wang, H.; Kim, D. H. Perovskite-Based Photodetectors: Materials and Devices. *Chem. Soc. Rev.* **2017**, *46* (17), 5204–5236. https://doi.org/10.1039/C6CS00896H.

(9) Pennicard, D.; Pirard, B.; Tolbanov, O.; Iniewski, K. Semiconductor Materials for X-Ray Detectors. *MRS Bulletin* **2017**, *42* (6), 445–450. https://doi.org/10.1557/mrs.2017.95.

(10) Spahn, M. X-Ray Detectors in Medical Imaging. *Nuclear Instruments and Methods in Physics Research Section A: Accelerators, Spectrometers, Detectors and Associated Equipment* **2013**, *731*, 57–63. https://doi.org/10.1016/j.nima.2013.05.174.

(11) Datta, A.; Zhong, Z.; Motakef, S. A New Generation of Direct X-Ray Detectors for Medical and Synchrotron Imaging Applications. *Sci Rep* **2020**, *10* (1), 20097. https://doi.org/10.1038/s41598-020-76647-5.

(12) Kasap, S.; Frey, J. B.; Belev, G.; Tousignant, O.; Mani, H.; Greenspan, J.; Laperriere, L.; Bubon, O.; Reznik, A.; DeCrescenzo, G.; Karim, K. S.; Rowlands, J. A. Amorphous and Polycrystalline Photoconductors for Direct Conversion Flat Panel X-Ray Image Sensors. *Sensors* **2011**, *11* (5), 5112–5157. https://doi.org/10.3390/s110505112.

(13) Kasap, S. Low-Cost X-Ray Detectors. *Nature Photon* **2015**, *9* (7), 420–421. https://doi.org/10.1038/nphoton.2015.108.

(14) Datta, A.; Fiala, J.; Motakef, S. 2D Perovskite-Based High Spatial Resolution X-Ray Detectors. *Sci Rep* **2021**, *11* (1), 22897. https://doi.org/10.1038/s41598-021-02378-w.

(15) Kakavelakis, G.; Gedda, M.; Panagiotopoulos, A.; Kymakis, E.; Anthopoulos, T. D.; Petridis, K. Metal Halide Perovskites for High-Energy Radiation Detection. *Advanced Science* **2020**, *7* (22), 2002098. https://doi.org/10.1002/advs.202002098.

(16) Kasap, S.; Frey, J. B.; Belev, G.; Tousignant, O.; Mani, H.; Laperriere, L.; Reznik, A.; Rowlands, J. A. Amorphous Selenium and Its Alloys from Early Xeroradiography to High Resolution X-Ray Image Detectors and Ultrasensitive Imaging Tubes. *physica status solidi (b)* **2009**, *246* (8), 1794–1805. https://doi.org/10.1002/pssb.200982007.

(17) Kang, J.; Wang, L.-W. High Defect Tolerance in Lead Halide Perovskite CsPbBr3. *J. Phys. Chem. Lett.* **2017**, *8* (2), 489–493. https://doi.org/10.1021/acs.jpclett.6b02800.

(18) Peng, J.; Xia, C. Q.; Xu, Y.; Li, R.; Cui, L.; Clegg, J. K.; Herz, L. M.; Johnston, M. B.; Lin, Q. Crystallization of CsPbBr3 Single Crystals in Water for X-Ray Detection. *Nat Commun* **2021**, *12* (1), 1531. https://doi.org/10.1038/s41467-021-21805-0.

(19) Pan, W.; Yang, B.; Niu, G.; Xue, K.-H.; Du, X.; Yin, L.; Zhang, M.; Wu, H.; Miao, X.-S.; Tang, J. Hot-Pressed CsPbBr3 Quasi-Monocrystalline Film for Sensitive Direct X-Ray Detection. *Advanced Materials* **2019**, *31* (44), 1904405. https://doi.org/10.1002/adma.201904405.

(20) Zhao, H.; Qiu, J.; Hou, B.; Yi, L.; Qin, X.; Liu, X. Flexible Perovskite X-Ray Detectors through Interfacial Modification with Perylene Diimide. *Advanced Optical Materials* n/a (n/a), 2202668. https://doi.org/10.1002/adom.202202668.

(21) Liang, J.; Wang, C.; Wang, Y.; Xu, Z.; Lu, Z.; Ma, Y.; Zhu, H.; Hu, Y.; Xiao, C.; Yi, X.; Zhu, G.; Lv, H.; Ma, L.; Chen, T.; Tie, Z.; Jin, Z.; Liu, J. All-Inorganic Perovskite Solar Cells. *J. Am. Chem. Soc.* **2016**, *138* (49), 15829–15832. https://doi.org/10.1021/jacs.6b10227.

(22) Hoffman, J. B.; Schleper, A. L.; Kamat, P. V. Transformation of Sintered CsPbBr3 Nanocrystals to Cubic CsPbI3 and Gradient CsPbBrxI3–x

through Halide Exchange. *J. Am. Chem. Soc.* **2016**, *138* (27), 8603–8611. https://doi.org/10.1021/jacs.6b04661.

(23) Gualdrón-Reyes, Andrés. F.; Yoon, S. J.; Barea, E. M.; Agouram, S.; Muñoz-Sanjosé, V.; Meléndez, Á. M.; Niño-Gómez, M. E.; Mora-Seró, I. Controlling the Phase Segregation in Mixed Halide Perovskites through Nanocrystal Size. *ACS Energy Lett.* **2019**, *4* (1), 54–62. https://doi.org/10.1021/acsenergylett.8b02207.

(24) Kovalenko, M. V.; Protesescu, L.; Bodnarchuk, M. I. Properties and Potential Optoelectronic Applications of Lead Halide Perovskite Nanocrystals. *Science* **2017**, *358* (6364), 745–750. https://doi.org/10.1126/science.aam7093.

(25) Wang, H.-C.; Bao, Z.; Tsai, H.-Y.; Tang, A.-C.; Liu, R.-S. Perovskite Quantum Dots and Their Application in Light-Emitting Diodes. *Small* **2018**, *14* (1), 1702433. https://doi.org/10.1002/smll.201702433.

(26) Kim, Y.; Yassitepe, E.; Voznyy, O.; Comin, R.; Walters, G.; Gong, X.; Kanjanaboos, P.; Nogueira, A. F.; Sargent, E. H. Efficient Luminescence from Perovskite Quantum Dot Solids. *ACS Appl. Mater. Interfaces* **2015**, *7* (45), 25007–25013. https://doi.org/10.1021/acsami.5b09084.

(27) Shamsi, J.; Rastogi, P.; Caligiuri, V.; Abdelhady, A. L.; Spirito, D.; Manna, L.; Krahne, R. Bright-Emitting Perovskite Films by Large-Scale Synthesis and Photoinduced Solid-State Transformation of CsPbBr3 Nanoplatelets. *ACS Nano* **2017**, *11* (10), 10206–10213. https://doi.org/10.1021/acsnano.7b04761.

(28) Stoumpos, C. C.; Malliakas, C. D.; Peters, J. A.; Liu, Z.; Sebastian, M.; Im, J.; Chasapis, T. C.; Wibowo, A. C.; Chung, D. Y.; Freeman, A. J.; Wessels, B. W.; Kanatzidis, M. G. Crystal Growth of the Perovskite Semiconductor CsPbBr3: A New Material for High-Energy Radiation Detection. *Crystal Growth & Design* **2013**, *13* (7), 2722–2727. https://doi.org/10.1021/cg400645t.

(29) Zhai, W.; Lin, J.; Li, C.; Hu, S.; Huang, Y.; Yu, C.; Wen, Z.; Liu, Z.; Fang, Y.; Tang, C. Solvothermal Synthesis of Cesium Lead Halide Perovskite Nanowires with Ultra-High Aspect Ratios for High-Performance Photodetectors. *Nanoscale* **2018**, *10* (45), 21451–21458. https://doi.org/10.1039/C8NR05683H.

(30) Chen, J.; Fu, Y.; Samad, L.; Dang, L.; Zhao, Y.; Shen, S.; Guo, L.; Jin, S. Vapor-Phase Epitaxial Growth of Aligned Nanowire Networks of Cesium Lead Halide Perovskites (CsPbX3, X = Cl, Br, I). *Nano Lett.* **2017**, *17* (1), 460–466. https://doi.org/10.1021/acs.nanolett.6b04450.

(31) Drushliak, V.; Szafrański, M. Thermodynamic Stability, Structure, and Optical Properties of Perovskite-Related CsPb2Br5 Single Crystals under Pressure. *Inorg. Chem.* **2022**, *61* (36), 14389–14396. https://doi.org/10.1021/acs.inorgchem.2c02253.

(32) Zhang, H.; Gao, Z.; Liang, R.; Zheng, X.; Geng, X.; Zhao, Y.; Xie, D.; Hong, J.; Tian, H.; Yang, Y.; Wang, X.; Ren, T.-L. X-Ray Detector Based on All-Inorganic Lead-Free Cs2AgBiBr6 Perovskite Single Crystal. *IEEE Transactions on Electron Devices* **2019**, *66* (5), 2224–2229. https://doi.org/10.1109/TED.2019.2903537.

(33) Keshavarz, M.; Debroye, E.; Ottesen, M.; Martin, C.; Zhang, H.; Fron, E.; Küchler, R.; Steele, J. A.; Bremholm, M.; Van de Vondel, J.; Wang, H. I.; Bonn, M.; Roeffaers, M. B. J.; Wiedmann, S.; Hofkens, J. Tuning the Structural and Optoelectronic Properties of Cs2AgBiBr6 Double-Perovskite Single Crystals through Alkali-Metal Substitution. *Advanced Materials* **2020**, *32* (40), 2001878. https://doi.org/10.1002/adma.202001878.

(34) Zhang, H.; Wang, F.; Lu, Y.; Sun, Q.; Xu, Y.; Zhang, B.-B.; Jie, W.; Kanatzidis, M. G. High-Sensitivity X-Ray Detectors Based on Solution-Grown Caesium Lead Bromide Single Crystals. *J. Mater. Chem. C* **2020**, *8* (4), 1248–1256. https://doi.org/10.1039/C9TC05490A.

(35) Chai, Y.; Juan, Z.; Wu, Y.; Liu, Y.; Li, X. Suppressing the Ion Migration in Halide Perovskite Wafers for Current-Drift Free X-Ray Detectors. *ACS Appl. Electron. Mater.* **2023**, *5* (1), 544–551. https://doi.org/10.1021/acsaelm.2c01597.

(36) Sakhatskyi, K.; John, R. A.; Guerrero, A.; Tsarev, S.; Sabisch, S.; Das, T.; Matt, G. J.; Yakunin, S.; Cherniukh, I.; Kotyrba, M.; Berezovska, Y.; Bodnarchuk, M. I.; Chakraborty, S.; Bisquert, J.; Kovalenko, M. V. Assessing the Drawbacks and Benefits of Ion Migration in Lead Halide Perovskites. *ACS Energy Lett.* **2022**, *7* (10), 3401–3414. https://doi.org/10.1021/acsenergylett.2c01663.

(37) Takahashi, T.; Watanabe, S.; Kouda, M.; Sato, G.; Okada, Y.; Kubo, S.; Kuroda, Y.; Onishi, M.; Ohno, R. High-Resolution CdTe Detector and Applications to Imaging Devices. *IEEE Transactions on Nuclear Science* **2001**, *48* (3), 287–291. https://doi.org/10.1109/23.940067.

(38) Tsai, H.; Liu, F.; Shrestha, S.; Fernando, K.; Tretiak, S.; Scott, B.; Vo, D. T.; Strzalka, J.; Nie, W. A Sensitive and Robust Thin-Film x-Ray Detector Using 2D Layered Perovskite Diodes. *Science Advances* **2020**, *6* (15), eaay0815. https://doi.org/10.1126/sciadv.aay0815.

(39) He, Y.; Hadar, I.; De Siena, M. C.; Klepov, V. V.; Pan, L.; Chung, D. Y.; Kanatzidis, M. G. Sensitivity and Detection Limit of Spectroscopic-Grade Perovskite CsPbBr3 Crystal for Hard X-Ray Detection. *Advanced Functional Materials* **2022**, *32* (24), 2112925. https://doi.org/10.1002/adfm.202112925.

(40) J. O'Kane, S. E.; Richardson, G.; Pockett, A.; G. Niemann, R.; M. Cave, J.; Sakai, N.; E. Eperon, G.; J. Snaith, H.; M. Foster, J.; J. Cameron, P.; B. Walker, A. Measurement and Modelling of Dark Current Decay Transients in Perovskite Solar Cells. *Journal of Materials Chemistry C* **2017**, *5* (2), 452–462. https://doi.org/10.1039/C6TC04964H.

(41) Duijnstee, E. A.; Le Corre, V. M.; Johnston, M. B.; Koster, L. J. A.; Lim, J.; Snaith, H. J. Understanding Dark Current-Voltage Characteristics in Metal-Halide Perovskite Single Crystals. *Phys. Rev. Appl.* **2021**, *15* (1), 014006. https://doi.org/10.1103/PhysRevApplied.15.014006.

(42) Wang, Z.; Zeng, L.; Zhu, T.; Chen, H.; Chen, B.; Kubicki, D. J.; Balvanz, A.; Li, C.; Maxwell, A.; Ugur, E.; dos Reis, R.; Cheng, M.; Yang, G.; Subedi, B.; Luo, D.; Hu, J.; Wang, J.; Teale, S.; Mahesh, S.; Wang, S.; Hu, S.; Jung, E.; Wei, M.; Park, S. M.; Grater, L.; Aydin, E.; Song, Z.; Podraza, N. J.; Lu, Z.-H.; Huang, J.; Dravid, V. P.; De Wolf, S.; Yan, Y.; Grätzel, M.; Kanatzidis, M.; Sargent, E. Suppressed Phase Segregation for Triple-Junction Perovskite Solar Cells. *Nature* **2023**, 1–3. https://doi.org/10.1038/s41586-023-06006-7.

(43) Devanathan, R.; Corrales, L. R.; Gao, F.; Weber, W. J. Signal Variance in Gamma-Ray Detectors—A Review. *Nuclear Instruments and Methods in Physics Research Section A: Accelerators, Spectrometers, Detectors and Associated Equipment* **2006**, *565* (2), 637–649. https://doi.org/10.1016/j.nima.2006.05.085.

(44) Nikl, M.; Nitsch, K.; Mihóková, E.; Polák, K.; Fabeni, P.; Pazzi, G. P.; Gurioli, M.; Santucci, S.; Phani, R.; Scacco, A.; Somma, F. Luminescence of CsPbBr3-like Quantum Dots in CsBr Single Crystals. *Physica E: Low-dimensional Systems and Nanostructures* **1999**, *4* (4), 323–331. https://doi.org/10.1016/S1386-9477(99)00016-8.

(45) Wu, X.; Zhang, X.; Yu, W.; Zhou, Y.; Wong, W.; He, W.; Ping Loh, K.; Jiang, X.-F.; Xu, Q.-H. Indirect-to-Direct Bandgap Transition in Layered Metal Halide Perovskite – CsPb 2 Br 5. *Journal of Materials Chemistry A* **2023**. https://doi.org/10.1039/D2TA06697A.

(46) Zhang, H.; Liu, X.; Dong, J.; Yu, H.; Zhou, C.; Zhang, B.; Xu, Y.; Jie, W. Centimeter-Sized Inorganic Lead Halide Perovskite CsPbBr3 Crystals Grown by an Improved Solution Method. *Crystal Growth & Design* **2017**, *17* (12), 6426–6431. https://doi.org/10.1021/acs.cgd.7b01086.

(47) Steele, J. A.; Puech, P.; Keshavarz, M.; Yang, R.; Banerjee, S.; Debroye, E.; Kim, C. W.; Yuan, H.; Heo, N. H.; Vanacken, J.; Walsh, A.; Hofkens, J.; Roeffaers, M. B. J. Giant Electron–Phonon Coupling and Deep Conduction Band Resonance in Metal Halide Double Perovskite. *ACS Nano* **2018**, *12* (8), 8081–8090. https://doi.org/10.1021/acsnano.8b02936.

(48) Shi, M.; Li, G.; Tian, W.; Jin, S.; Tao, X.; Jiang, Y.; Pidko, E. A.; Li, R.; Li, C. Understanding the Effect of Crystalline Structural Transformation for Lead-Free Inorganic Halide Perovskites. *Advanced Materials* **2020**, *32* (31), 2002137. https://doi.org/10.1002/adma.202002137.

(49) Wu, B.; Yuan, H.; Xu, Q.; Steele, J. A.; Giovanni, D.; Puech, P.; Fu, J.; Ng, Y. F.; Jamaludin, N. F.; Solanki, A.; Mhaisalkar, S.; Mathews, N.; Roeffaers, M. B. J.; Grätzel, M.; Hofkens, J.; Sum, T. C. Indirect Tail States Formation by Thermal-Induced Polar Fluctuations in Halide

Perovskites. *Nat Commun* **2019**, *10* (1), 484. https://doi.org/10.1038/s41467-019-08326-7.

(50) Shi, Y.; Zhao, W.; Ma, Z.; Xiao, G.; Zou, B. Self-Trapped Exciton Emission and Piezochromism in Conventional 3D Lead Bromide Perovskite Nanocrystals under High Pressure. *Chemical Science* **2021**, *12* (44), 14711–14717. https://doi.org/10.1039/D1SC04987A.

(51) Pan, F.; Li, J.; Ma, X.; Nie, Y.; Liu, B.; Ye, H. Free and Self-Trapped Exciton Emission in Perovskite CsPbBr 3 Microcrystals. *RSC Advances* **2022**, *12* (2), 1035–1042. https://doi.org/10.1039/D1RA08629D.

(52) Zhou, Y.-Q.; Xu, J.; Liu, J.-B.; Liu, B.-X. Green Emission Induced by Intrinsic Defects in All-Inorganic Perovskite CsPb2Br5. *J. Phys. Chem. Lett.* **2019**, *10* (20), 6118–6123. https://doi.org/10.1021/acs.jpclett.9b02367.

(53) Brandt, R. E.; Poindexter, J. R.; Gorai, P.; Kurchin, R. C.; Hoye, R. L. Z.; Nienhaus, L.; Wilson, M. W. B.; Polizzotti, J. A.; Sereika, R.; Žaltauskas, R.; Lee, L. C.; MacManus-Driscoll, J. L.; Bawendi, M.; Stevanović, V.; Buonassisi, T. Searching for "Defect-Tolerant" Photovoltaic Materials: Combined Theoretical and Experimental Screening. *Chem. Mater.* **2017**, *29* (11), 4667–4674. https://doi.org/10.1021/acs.chemmater.6b05496.

(54) deQuilettes, D. W.; Koch, S.; Burke, S.; Paranji, R. K.; Shropshire, A. J.; Ziffer, M. E.; Ginger, D. S. Photoluminescence Lifetimes Exceeding 8 Ms and Quantum Yields Exceeding 30% in Hybrid Perovskite Thin Films by Ligand Passivation. *ACS Energy Lett.* **2016**, *1* (2), 438–444. https://doi.org/10.1021/acsenergylett.6b00236.

(55) Qin, L.; Wu, L.; Kattel, B.; Li, C.; Zhang, Y.; Hou, Y.; Wu, J.; Chan, W.-L. Using Bulk Heterojunctions and Selective Electron Trapping to Enhance the Responsivity of Perovskite–Graphene Photodetectors. *Advanced Functional Materials* **2017**, *27* (47), 1704173. https://doi.org/10.1002/adfm.201704173.

(56) Shi, H.; Zhang, X.; Sun, X.; Chen, R.; Zhang, X. Direct and Indirect Recombination and Thermal Kinetics of Excitons in Colloidal All-Inorganic Lead Halide Perovskite Nanocrystals. *J. Phys. Chem. C* **2019**, *123* (32), 19844–19850. https://doi.org/10.1021/acs.jpcc.9b04532.

(57) Ulbricht, R.; Hendry, E.; Shan, J.; Heinz, T. F.; Bonn, M. Carrier Dynamics in Semiconductors Studied with Time-Resolved Terahertz Spectroscopy. *Rev. Mod. Phys.* **2011**, *83* (2), 543–586. https://doi.org/10.1103/RevModPhys.83.543.

(58) Zhang, H.; Debroye, E.; Zheng, W.; Fu, S.; Virgilio, L. D.; Kumar, P.; Bonn, M.; Wang, H. I. Highly Mobile Hot Holes in Cs2AgBiBr6 Double Perovskite. *Science Advances* **2021**, *7* (52), eabj9066. https://doi.org/10.1126/sciadv.abj9066.

(59) Zhang, H.; Debroye, E.; Steele, J. A.; Roeffaers, M. B. J.; Hofkens, J.; Wang, H. I.; Bonn, M. Highly Mobile Large Polarons in Black Phase

CsPbI3. *ACS Energy Lett.* **2021**, *6* (2), 568–573. https://doi.org/10.1021/acsenergylett.0c02482.

(60) Cohen, B.-E.; Wierzbowska, M.; Etgar, L. High Efficiency and High Open Circuit Voltage in Quasi 2D Perovskite Based Solar Cells. *Advanced Functional Materials* **2017**, *27* (5), 1604733. https://doi.org/10.1002/adfm.201604733.

Chapter 4
Fabrication of High-Quality $CsPbBr_3$ Perovskite Films Using Chemical Vapor Deposition

This chapter is a manuscript in preparation.

*Lotte Clinckemalie[#], Samir Al-Hilfi[#], Donato Valli, Lei Gao, Roel Vanden Brande, Athina Papadopoulou, Jan Genoe, Mischa Bonn, Hai I. Wang, Johan Hofkens, Elke Debroye**

Author contributions:

[#]L.C. and S.A. contributed equally to the manuscript L.C. wrote the manuscript under the supervision of J.H. and E.D. L.C., S.A., D.V. and R.V.B. optimized the synthesis method. L.C. and D.V. measured XRD, SEM, UV-Vis transmission and PL spectra. L.G. performed THz measurements and analysis under the supervision of H.I.W. and M.B. A.P. analyzed the photodetector devices.

Situation in this PhD Dissertation

Pb-based MHPs have shown great promise as a semiconductor material for optoelectronics. However, their stability, processability as large-area layers and eco-toxicity have hampered their commercial usage. In this PhD dissertation, we investigated several ways to conquer these problems. This chapter focusses on the large-area deposition of $CsPbBr_3$ thin films.

Abstract

While metal halide perovskite (MHP) single crystals have demonstrated high performance as single-pixel X-ray and photodetectors, a controlled deposition of layers is necessary for application in large-area detector devices. However, the creation of smooth, high-quality, and pinhole-free films exhibiting long-term stability remains challenging. This work presents the successful fabrication of phase-pure, uniform, and pinhole-free $CsPbBr_3$ thin films by rationally tuning experimental parameters during chemical vapor deposition. Advanced THz spectroscopy studies indicate that the charge carrier mobility can be influenced by the amount of $CsPb_2Br_5$ side phase and the grain size. To boost the photodetector performance, Rb-doping was performed, leading to a more stable and improved external quantum efficiency (EQE) of 25% at an applied bias of -2 V and a responsivity (R) of 0.258 AW^{-1} at 2 V, which is competitive with current literature reports. This study demonstrates that CVD is a key approach that offers high-quality perovskite films with high stoichiometric precision, high phase-purity, and with very controllable uniformity and thickness.

4.1 Introduction

Metal halide perovskites (MHPs) have emerged as a promising new class of semiconductor materials for optoelectronics in the last decade. They have demonstrated remarkable success in the field of photovoltaics, achieving record performances in solar cells[1,2] as well as in light emitting diodes (LEDs)[3,4]. Additionally, MHPs have shown to exhibit a high performance in X-ray and photodetectors.[5,6] While MHP single crystals have demonstrated high performance as single-pixel X-ray and photodetectors, a controlled deposition of layers is necessary for application in large-area detector devices. It is crucial to maintain the high quality and stability achieved with single crystals during the development of perovskite films. However, the conventional method of preparing MHP thin films by spin-coating precursor solutions often leads to polycrystalline films with pinholes and a high defect density.[7–9] As defects can act as traps for photogenerated charge carriers (electrons and holes), their high density hinders further improvements in device efficiency.[10,11] Therefore, the fabrication of smooth, high-quality, and pinhole-free films remains an important challenge.

This challenge can be tackled by applying chemical vapor deposition (CVD), which is known for its potential to produce films of excellent quality.[12,13] As CVD does not require the use of solvents, this method offers several advantages over conventional solution-based deposition procedures. It eliminates solvent-related issues that can affect the crystal structure and film uniformity, such as the limited solubility of precursors leading to stoichiometric imbalances in the final product.[14] Additionally, residual solvents in solution-processed films can induce electronic defects in the crystal.[12,15,16] Finally, CVD reduces the cost of fabrication by eliminating the need for expensive solvents and simultaneously decreases the harmful impact on health and environment.[17]

A typical CVD setup (Figure 1) consists of a tube with multiple heating zones. In the first furnace, solid precursors are heated in a reduced pressure environment, causing them to evaporate into the gas phase. Guided by the flow of an inert carrier gas (N_2 or Ar), the precursor gases are transported to a cooler zone downstream in furnace 2, where the material will be deposited on or near the substrate due to the decrease in temperature. During the CVD process, the desired material can be formed by two different processes: the precursor gases can either reach the substrate first, where they react with each other to form the desired material (Figure 1, process 1-3), or they can

react in the gas phase and then be deposited on the substrate as the final product (Figure 1, process 4-6).[13,18,19] Since the precursor molecules are evaporated into reactive fragments, most CVD processes occur in the gas phase.[18]

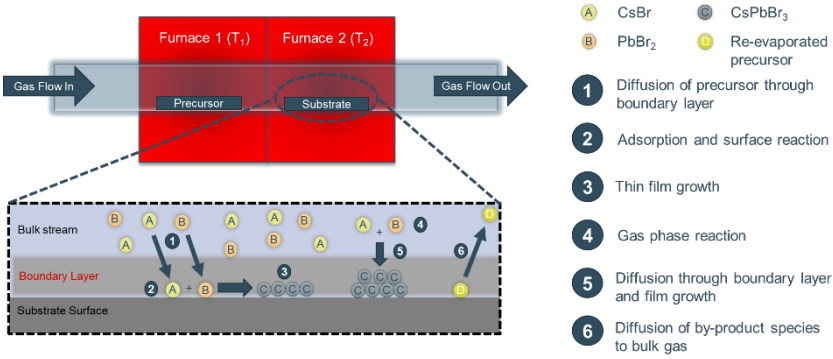

Figure 1. Scheme of a typical chemical vapor deposition setup and the possible chemical reactions, resulting in the deposition of the desired material.

The gas flow thus has a significant impact on the CVD process. It is typically laminar, meaning that the gas flows in parallel layers at different velocities. The laminar flow is maintained by controlling the velocity and direction of the gas flow.[13,19] As the gas flows over the substrate, a stagnant boundary layer is formed due to the frictional force between the gas stream and the substrate. The boundary layer is a thin layer of gas with a velocity significantly slower than the main gas stream, and its thickness depends on the velocity of the main gas flow and the properties of the substrate surface.[18,20] In CVD, the boundary layer plays a crucial role in determining the rate and quality of film growth as it is generally considered that all the chemical reactions of importance to the CVD process take place in the boundary layer and on the substrate surface.[18] The thickness and composition of the film can be affected by the diffusion of material gases through the boundary layer and their subsequent deposition on the substrate surface.[18,20] By optimizing the key parameters such as furnace temperatures, flow rate, pressure, reaction time, substrate thickness, material (additives), and the precursor ratio, the deposition of MHP films can be judiciously controlled and high-quality films can be fabricated with fine-tuned physical and chemical properties.[13,21,22]

This work demonstrates the successful fabrication of phase-pure $CsPbBr_3$ thin films using chemical vapor deposition, with a focus on controlling the composition and quality of the films. We found that the thickness and coverage of the films can be precisely adjusted by controlling the temperature of the second oven. The interplay between film thickness, grain size, phase purity and surface coverage was examined by probing the structural and optical properties by established characterization tools such as X-ray diffraction (XRD), UV-Vis and photoluminescence (PL) spectroscopy. Furthermore, the impact on the carrier transport properties was investigated through advanced THz spectroscopy and finally, the photodetector performance was validated. To further enhance the detection performance, Rb-doping was performed, resulting in an improved EQE of 25% at an applied bias of -2 V and an R of 0.258 AW^{-1} at 2 V, compared to an EQE of 20% and an R of 0.0442 AW^{-1} for the pristine $CsPbBr_3$ thin films.

4.2 Results and Discussion

In order to control the chemical vapor deposition (CVD) process, and thus the quality of the resulting film, it is essential to regulate the nucleation and growth rate of the thin film. This is mostly influenced by the evaporation (T_1) and substrate temperature (T_2) and the background pressure of the CVD chamber.[23] For instance, the presence of numerous pinholes in the film indicates a fast and uncontrolled deposition due to a high growth and nucleation rate. The pinhole density can be decreased by adjusting T_1 and T_2 to control the heat path that delivers the vapor.[24] Another option is to increase the pressure, which slows down the evaporation rate of the precursor, resulting in a slower and more controlled arrival of the material to the substrate. This leads to a slowed down nucleation and promotes crystal growth.[25] Additionally, other crucial factors such as the amount of precursor and gas flow rate can affect the chemical reaction and thus the properties of the deposited film.[26] Therefore, optimizing all these parameters is necessary to enhance the perovskite film quality.

To synthesize the $CsPbBr_3$ films, a stoichiometric molar ratio of CsBr and $PbBr_2$ is first carefully mixed together until a yellow-orange color is observed. The CVD reactor chamber is then loaded with this precursor material, after which it is evacuated to vacuum (~0.7 mbar) and flushed three times with inert Ar gas to remove the residual O_2. Afterwards, the precursor material is heated to the desired temperature ranging from 525 °C to 600 °C to evaporate it. With

the help of Ar as a carrier gas, the evaporated precursor reaches the substrate into the second furnace (temperature ranging from RT to 250 °C), where the $CsPbBr_3$ thin film is deposited onto a glass substrate. As a result, a thin film with a thickness of around 200 nm is fabricated, exhibiting a grain size up to 1.5 µm (Figure 2a) (see Table 1 for synthesis parameters). However, it should be noted that the grains are not uniform and pinholes are present, potentially as a result of a fast growth rate. In an attempt to lower this rate, the evaporation temperature is decreased to 525 °C and the pressure is increased to 0.9 mbar. This approach resulted in a densely packed, pinhole-free film with more uniform grains of around 0.5 µm (Figure 2b). The smaller grain size could be attributed to the higher substrate temperature, as we experienced that it ensures that more material is delivered to the substrate, which encourages the formation of more nucleation sites. To increase the grain sizes, the temperature of the second furnace (T_2) is decreased to room temperature, allowing for a slowed down nucleation rate, followed by growth. This successfully resulted in a significantly increased grain size with a diameter of around 5 µm and a very low pinhole density (Figure 2c). It has to be noted that the residual material on top of the film is related to the early deposition of $CsPbBr_3$ crystals before a stable T_1 is reached. This might be avoided by covering the substrate until T_1 is reached. Finally, based on earlier experience on enhanced photodetector performance upon Rb substitution[27], we doped the precursor material by replacing 5% of CsBr by RbBr. Later, the influence of Rb on the film properties such as the conductivity was extensively studied. Similar synthesis parameters as the second film (Figure 2b) are used, resulting in a similar pinhole-free film with slightly bigger grain sizes of around 1 µm (Figure 2d). To quantify the doping ratio, inductively coupled plasma optical emission spectrometry (ICP-OES) analysis is performed, revealing a ~2% substitution of the Cs^+ ion for Rb^+ (Table S1).

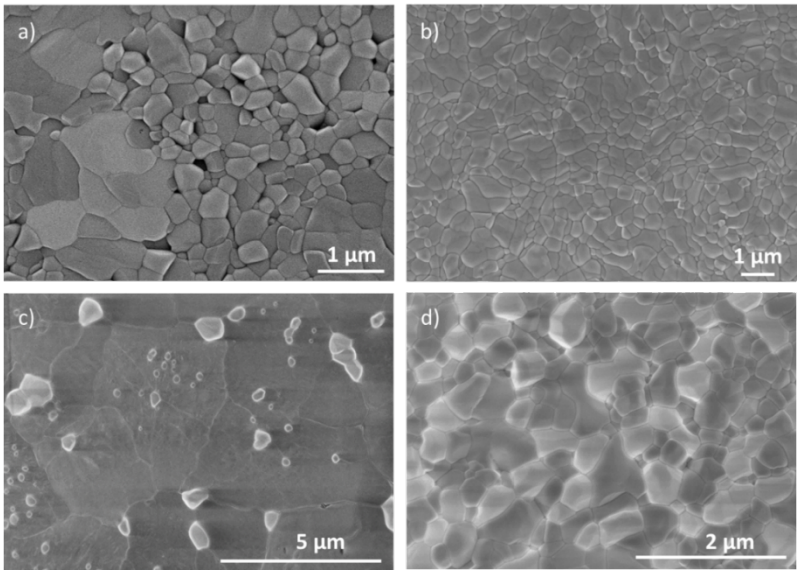

Figure 2. a-c) Grain size and morphology dependency of CVD synthesis parameters as analyzed by scanning electron microscopy (SEM). d) SEM image of Rb-doped $CsPbBr_3$ films.

Table 1. Synthesis parameters during CVD growth of different $CsPbBr_3$ perovskite films.

Sample	T_1 (°C)	T_2 (°C)	P (mbar)	T (min)
Figure 2a	600	RT	0.68	20
Figure 2b	525	150	0.9	20
Figure 2c	525	RT	0.9	20
Figure 2d (Rb-doping)	525	150	0.9	40

Furthermore, we found that not only the coverage, but also the thickness of the films can be controlled by tuning T_2 (Figure 3a). At temperatures ranging from room temperature to 150 °C, film thicknesses of 100 to 400 nm are achieved. As previously explained, a lower temperature range encourages a slower nucleation, which afterwards promotes growth of the grains. As a result, the grain size is larger and the film thickness lower. When temperatures higher than 150 °C are used, a thicker sample is produced due to a high

nucleation site density, resulting in the formation of many smaller $CsPbBr_3$ crystals. However, since nucleation is promoted over growth, the time for crystal formation is limited and the grains are unable to nicely connect to one another. These faster dynamics at higher substrate temperature result in the formation of pinholes and an incomplete coverage of the sample.

To verify the crystal structure of the target material, X-ray diffraction (XRD) measurements are conducted. For all samples with thicknesses ranging from 200 nm up to 1500 µm, XRD shows the formation of orthorhombic $CsPbBr_3$ crystals (Figure 3b).[28] However, it is important to note that not all films are phase-pure as some show a small amount of $CsPb_2Br_5$ as a side phase (Figure S1). Post-treatment by annealing might be a promising approach to reduce this side phase formation as inspired by Tong *et al.* They demonstrated that $CsPb_2Br_5$ films grown via vacuum vapor deposition can be converted into $CsPbBr_3$ by annealing. The combination of the high-temperature instability of $CsPb_2Br_5$ and the volatile nature of $PbBr_2$ promotes the chemical reaction $CsPb_2Br_5 \rightarrow CsPbBr_3 + PbBr_2$, resulting in the formation of phase-pure $CsPbBr_3$ films.[29] For the Rb-doped film, a small shift of the XRD peaks toward a higher 2θ angle is observed compared to the pristine films, suggesting a lattice shrink as a result of the incorporation of the smaller Rb^+ ion (Figure S2).[30]

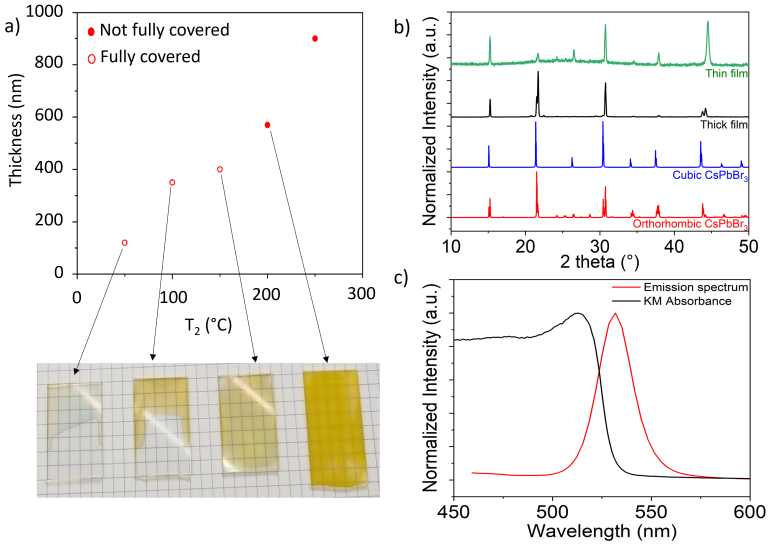

Figure 3. a) Impact of the substrate temperature (T_2) on the film thickness and surface coverage. b) Structural characterization of the CVD-grown samples by X-ray diffraction. c) Optical characterization by UV-VIS (black) and PL spectroscopy (red).

UV-Vis transmission spectra of the films are measured to examine the interplay between the grain size, film thickness and surface coverage on the optical properties (Figure 3c). Tauc plots are generated to quantify and study the change in the bandgap energy (Figure S3). The results indicate that even though these properties slightly differ, all films exhibit similar absorption edges, located at 520 nm, corresponding to a direct bandgap of 2.35 eV, which is in agreement with literature for phase-pure $CsPbBr_3$ crystals.[31,32] Presumably, there is no significant difference in the absorption edge or bandgap between the pristine films and the films with a small amount of side phase or Rb-doping, as the contribution of the impurity is small and therefore negligible.

For the CVD-grown $CsPbBr_3$ films, a green emission is detected in the steady-state photoluminescence (PL) spectra with a maximum intensity at 530 nm (Figure 3c) which is consistent with literature.[31,32] Similar to what is observed during UV-VIS measurements, comparable PL behavior is observed for the Rb-doped samples. Interestingly, the thickness of the film can influence the emission properties due to quantum-size effects. An increased or decreased Stokes shift, indicated by a redshift of 5 nm or blueshift of 2 nm in the PL peak, can be observed, corresponding to the increased or decreased thickness of the sample respectively (Figure S4).[33]

Ultrafast and contact-free THz time-domain spectroscopy (THz-TDS) studies with sub-ps time resolution are applied on a selected set of samples to probe the impact of the different film properties on the electrical transport. In the optical pump-THz probe (OPTP) experiment, an optical pulse (400 nm, ~100 fs pulse duration) is first used to excite electrons of the perovskite thin film from the valence band to the conduction band. Next, a single-cycle THz pulse with electric field $E(t)$ transmits collinearly through the sample, probing the photoexcitation-induced change of the conductivity, i.e., photoconductivity $\Delta\sigma$ (Figure 4a). In the thin film approximation, $\Delta\sigma$ is proportional to the relative attenuation of the THz electric field, $-\Delta E/E_0$ ($\Delta E = E_{pump} - E_0$, with E_{pump} and E_0 being the transmitted THz electric field with and without photoexcitation, respectively).[34] By varying the pump probe delay time t_P, the photoconductivity dynamics for the different CVD grown samples can be obtained and compared.

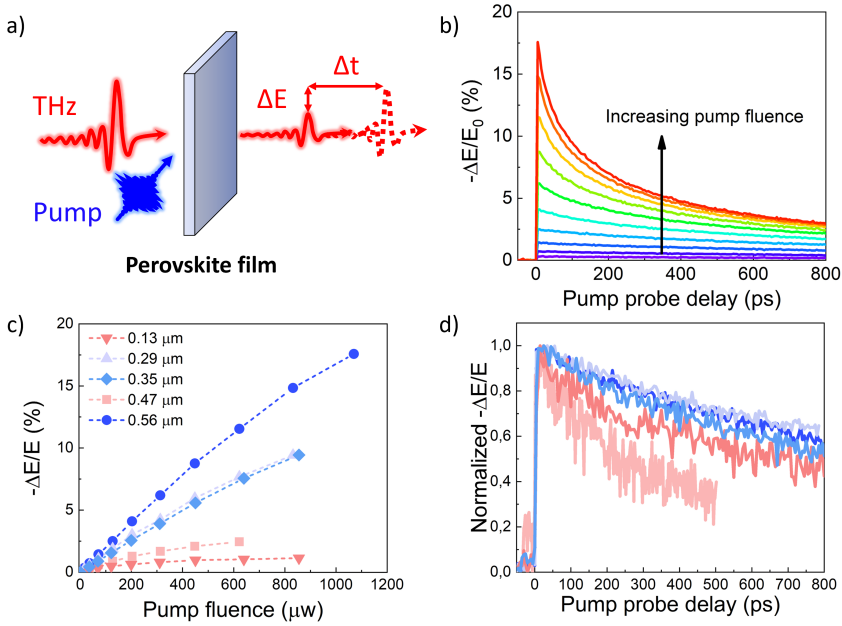

Figure 4. a) Schematic of the OPTP experiment on a perovskite thin film. b) Pump fluence dependent OPTP results of the CVD grown sample. The pump energy is 3.1 eV. c) Pump fluence dependent intensity of the photoconductivity of films with different average grain sizes. d) Normalized OPTP results of the perovskites with different grain sizes. The pump energy is 3.1 eV and the carrier kinetics are excited at the same pump fluence (36.3 μW/mm²).

First, we conducted fluence-dependent OPTP dynamics for samples with different grain sizes, and an example of a grain size of 0.57 μm can be seen in Figure 4b. To investigate the effect of the grain size on the conductivity, we compared the peak intensity of $-\Delta E/E$, which is proportional to $\Delta\sigma$, at different pump fluences after excitation by 3.1 eV light (Figure 4c). It is clear that the peak intensity of $-\Delta E/E$ increases with the enhancement of excitation power, which can be explained by the incremental photoinjected carriers. Furthermore, in contradiction to what is expected, the peak intensity of $-\Delta E/E$ not only depends on the grain size of the films. This indicates that the grain size is not the sole contributor to the change in mobility in $CsPbBr_3$ perovskites. On the other hand, we observe a strong correlation between the amplitude of the photoconductivity (Figure 4c) and the carrier lifetime (Figure 4d). This result indicates that the increased mobility can be attributed to a reduced contribution from defect scattering. This, in turn, suggests that

besides the grain size, other parameters can play a significant role in influencing defect density and, consequently, the photophysical properties of the material.

Next to the grain size, the contribution of the $CsPb_2Br_5$ side phase needs to be taken into account as it might also influence the mobility. Therefore, Rietveld refinement was performed on the XRD patterns to quantify the amount of side phase in each sample with different grain size (Table S3). As a result, it can clearly be seen that the side phase has a pronounced role in tuning the conductivity. In short, we conclude that both grain size and the side phase impact the photoconductivity of the samples. Deeper investigation is needed and currently ongoing to determine and understand the interplay between the grain size, amount of side phase and the mobility.

We then investigate and compare the pristine $CsPbBr_3$ film with the Rb-doped one, and observe a slight increase in mobility upon Rb-doping. This is expected as the incorporation of Rb results in a shrinkage of the crystal lattice, causing enhanced orbital interactions between Pb and Br. As a result, fewer traps are formed due to the less mobile ions, leading to an enhancement of carrier transport of the Rb-doped perovskite.[30,35] To further investigate this effect, we measured the frequency-resolved photoconductivity spectrum by Fourier transforming the time-domain THz field $\Delta E(t)$ and $E_0(t)$. The obtained spectrum in Figure 5a can be adequately fitted by the Drude-Smith model with Lorentz line shape:[36]

$$\sigma(\omega) = \frac{\omega_p^2 \varepsilon_0 \tau_s}{1 - i\omega\tau}\left(1 + \frac{c}{1 - i\omega\tau}\right) + \sum_m \frac{g_m \omega}{i(\omega_m^2 - \omega^2) + \gamma_m \omega}$$

This model describes the free carrier transport with preferential backscattering from, e.g., the grain boundaries. Here, parameter c $(-1 < c < 0)$ is introduced to account for the different extent of backscattering. For $c = -1$, the charge carriers are going through 100% backscattering, while for $c = 0$, the Drude-Smith model is simplified to the Drude model. ω_p is the plasma frequency which is directly related to the carrier density N by $\omega_p = \sqrt{\frac{N}{\varepsilon_0 \cdot m^*}}\, e$ (m^* is the effective mass), ε_0 the vacuum permittivity, τ_s the scattering time and ω the angular frequency. The second term of the equation represents the Lorentzian component, which is associated with the contribution of phonon modes in perovskites. The oscillator strength, fullwidth at half-maximum, and THz angular frequency of the optical phonon modes are denoted as g_m, γ_m, and ω_m, respectively. When comparing the conductivity of the pristine and Rb-doped $CsPbBr_3$ perovskite

in Figure 5b and c, it indicates that doping with Rb can effectively elevate the dc conductivity (shown in Figure 5b after removing the phonon contributions) and the photoconductivity of the perovskite by a similar percentage of ~20%. This observation suggests that the enhanced photoconductivity primarily originates from the improved electrical conductivity within the perovskite structures, rather than being primarily attributed to phonon response. As earlier mentioned, this enhancement can be attributed to the passivation of trap states within the perovskite films.[30,35]

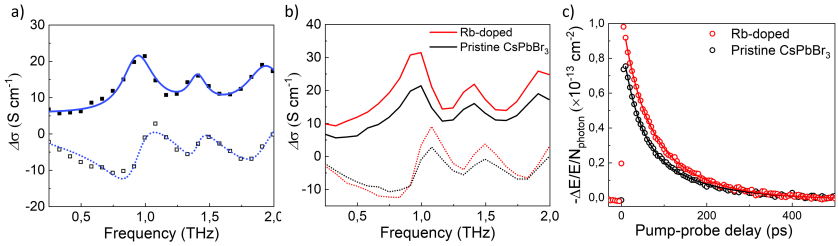

Figure 5. a) Drude-Smith-Lorentz fitting result (blue) of the complex photoconductivity (black) in pristine CVD grown $CsPbBr_3$. b) The photoconductivity spectrum of the pristine (black) and Rb-doped (red) $CsPbBr_3$, respectively. The photoconductivity was measured at 10 ps after the pump. c) OPTP results of the pristine (black) and Rb-doped $CsPbBr_3$ (red) respectively, normalized to the photon density.

Photodetector devices based on the pristine $CsPbBr_3$ film and the Rb-doped film exhibiting similar grain size are fabricated and characterized. First, the films are grown on a glass-ITO substrate with NiO as hole-transport layer during the CVD process. Subsequently, C60 is deposited on top as electron-transport layer, and finally, aluminum is evaporated to serve as the contact electrode. Current-voltage (I-V) measurements are then performed in dark and under AM 1.5G illumination (Figure 6a,b). For all CVD-grown perovskite samples, negligible hysteresis is observed, indicating good stability of the devices as mobile ions are not generated and did not influence the measurement. When comparing the pristine film-based device with the Rb-doped device, it is evident that doping decreases the dark current (Figure 6a). This is not surprising, since current leaking is mostly induced by defects acting as charge traps. As previously mentioned, the Rb-doped sample exhibits a better orbital overlapping, minimizing ion migration and thereby resulting in the improved low dark current.[30] Furthermore, starting from 1 V, the photocurrent is also increased upon Rb-doping as a consequence of the improved film quality (Figure 6b). When measuring the EQE of these devices, this results in an increased EQE of 25% at an applied bias of -2 V for the

Rb-doped device (Figure 6d), compared to 20% for the pristine device (Figure 6c). To assess the performance of the pristine and Rb-doped devices, the responsivity (R) was calculated by the following formula:

$$R = \frac{I_p}{P}$$

Where I_p is the photocurrent and P is the incident light power (100 mW/cm^2).[37] This resulted in a R of 0.0442 and 0.258 AW^{-1} under a bias voltage of 2 V for the pristine and Rb-doped device respectively. Even though these are preliminary results and further optimization of the device layers is necessary, these values are competitive with current literature reports on $CsPbBr_3$ single crystals and thin films (Table S2). This indicates that CVD is a key approach that offers high-quality perovskite films with high stoichiometric precision, high phase-purity, and with very controllable uniformity and thickness. Ultimately, this approach can be extended toward the deposition of other (lead-free) perovskite materials in high-performance optoelectronic devices.

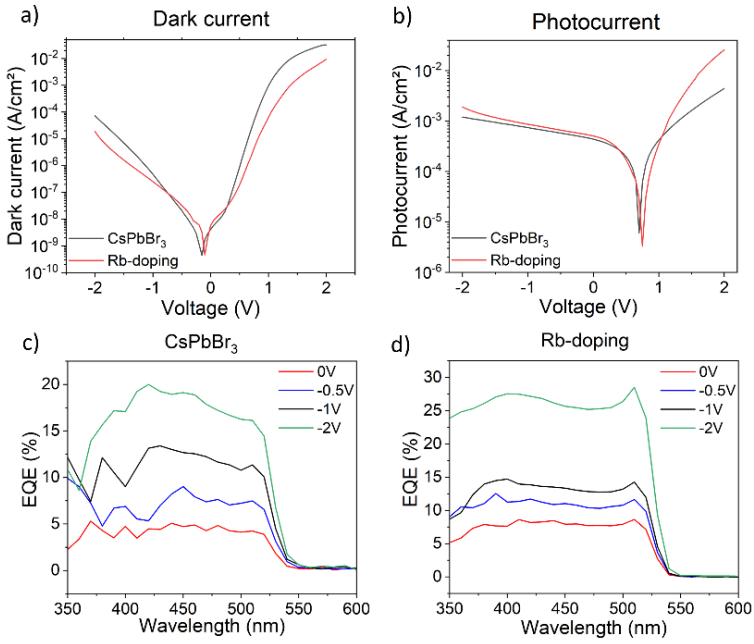

Figure 6. Current-voltage (I-V) curves of the pristine $CsPbBr_3$ (black) and Rb-doped (red) devices measured in a) dark and b) under AM 1.5 G illumination. EQE spectra under different applied bias of a c) pristine $CsPbBr_3$ and d) Rb-doped device.

Based on this knowledge, we optimized a home-built setup at KU Leuven (Figure S5) by implementing several adjustments to ensure a reproducible synthesis method. Firstly, a new vacuum pump is installed to achieve a deeper vacuum, resulting in an improved evaporation regime and the improved removal of oxygen and water impurities. Secondly, the first oven is reprogrammed to reach a higher evaporation temperature with a maximum of 600 °C. Next, a ball valve is mounted between the pump and the setup to allow the installation to remain under vacuum and prevent air contamination, even when the pump is not running. For safety reasons, an overpressure relief valve is also installed to prevent the pressure from getting too high when the ball valve is closed. Furthermore, to prevent contamination, the carrier gas is switched from nitrogen to more pure and inert argon. Finally, to bypass the problem of the significant difference in evaporation temperatures of CsBr and $PbBr_2$, the handling of the precursors is drastically changed by pre-grinding or pre-melting them so that $CsPbBr_3$ powder is already formed before the reaction, leading to a more uniform evaporation.

As each setup is different (e.g. different diameter and length of tube), the parameters are adjusted for this specific customized setup. A CsBr/$PbBr_2$ ratio of 1/1.2 is pre-melted for 10 minutes prior to the CVD synthesis. The synthesis is then conducted with T_1 and T_2 temperatures set at 520 °C and 220 °C, respectively, and at a pressure of 0.96 mbar with a reaction time of 15 minutes. This results in a smooth thin film that exhibits similar optical properties to the earlier mentioned films (Figure 7a). However, it should be noted that the absorption edge is less sharp due to slightly lower material uniformity and quality. The absorption edge is observed at 515 nm, corresponding to a direct bandgap of 2.3 eV, and by using steady-state PL, a green emission is detected with a maximum intensity at 525 nm. The film exhibits large grains up to 10 µm in size, but the grains are not uniform and pinholes are present as a result of a fast growth rate (Figure 7b). XRD analysis confirms the formation of orthorhombic $CsPbBr_3$ (Figure 7c). However, it is clear that the film contains a $CsPbBr_3$-$CsPb_2Br_5$ mixed phase, which explains the 5 nm blue shift in the maximum PL intensity compared to the earlier mentioned CVD grown $CsPbBr_3$ thin films.[38] Even though this sample appears promising, it is clear that the optimized parameters for this specific setup still need to be determined, which unfortunately did not fit within my PhD project timeline.

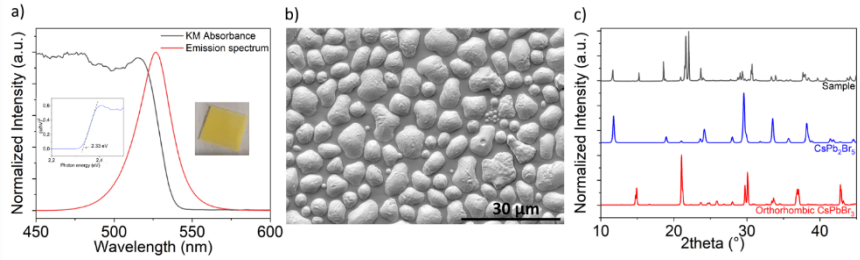

Figure 7. Characterization of a $CsPbBr_3$ sample fabricated on our home-built setup. a) Optical characterization by UV-VIS (black) and PL spectroscopy (red), inset shows the bandgap energy calculation (blue) and a picture of the fabricated film. b) SEM image of the film, showing barely interconnected grains. c) XRD pattern (black) indicating a $CsPbBr_3$-$CsPb_2Br_5$ mixed phase.

4.3 Conclusion and Outlook

In conclusion, controlling the chemical vapor deposition process is crucial for regulating the material nucleation and growth rate and achieving the desired composition and quality of the film. This work has demonstrated the successful fabrication of phase-pure, uniform, and pinhole-free $CsPbBr_3$ thin films using chemical vapor deposition. We found that the thickness and coverage of the films can be precisely adjusted by controlling the substrate temperature. Furthermore, the impact of the grain size and $CsPb_2Br_5$ side phase on the carrier transport properties was also examined through THz spectroscopy, indicating that the interplay between both parameters influences the mobility. To boost the performance of the films as photodetectors, Rb-doping was performed, resulting in a more stable and improved EQE of 25%. Finally, the knowledge gained from this work was used to optimize a home-built setup. This ongoing project further aims to reduce the side-phase formation and to further investigate the impact of dopants on film properties, such as the photocarrier lifetime and conductivity. By rationally adjusting all parameters, it is possible to optimize the deposition process of perovskite films and achieve better performance in large-area optoelectronic devices. Ultimately, this study can be translated to the development of high-performance optoelectronic devices based on lead-free perovskite materials in the near future.

This PhD chapter demonstrates that CVD is a synthesis method that provides a viable option for rapid and large-scale deposition of high-quality thin films.

Furthermore, being solvent-free, it represents a significant step towards more eco-friendly perovskite synthesis methods. However, the preference for lead-free alternatives persists to further mitigate toxicity. Therefore, the exploration of lead-free alternatives remains a topic of interest. Consequently, the primary focus of Chapter 5 is a novel synthesis pathway to further improve the well-known lead-free double perovskites.

4.4 Supporting Information

4.4.1 Experimental Section

Material synthesis: All precursor chemicals were obtained commercially from either Alfa Aesar (CsBr, 99%) or Sigma-Aldrich ($PbBr_2$, 98%; RbBr, 99.9%) without any further purification.

4.4.2 Material Characterization

Scanning electron microscopy (SEM) was used to obtain images of the crystals. They were recorded on a FEI-Q FEG250 instrument.

X-ray diffraction (XRD) patterns were recorded with a Malvern PANalytical Empyrean diffractometer with Bragg–Brentano geometry using a PIXcel3D solid-state detector and a Cu anode. The diffractogram was recorded in the 2θ range from 5 to 50° with a step size of 0.0131° and an integration time of 108 s/step.

***In situ* UV–Vis Transmission** data were recorded between 400 and 800 nm with a step of 1 nm via a PerkinElmer Lambda 950 UV–vis spectrophotometer equipped with an integrating sphere at ambient temperature. $BaSO_4$ powder was used as reference

Steady-state photoluminescence (PL) excitation-emission maps were measured with an excitation range between 250 nm and 600 nm with a step of 5 nm and an emission range between 450 and 800 nm with a step of 5 nm via an Edinburgh FLS980 fluorimeter.

Terahertz photoconductivity measurements provide a contact-free means for photoconductivity measurements. Using an ultrashort visible laser pulse (400 nm, FWHM ≈ 50 fs), charge carriers were optically injected into the conduction bands. Subsequently, the conductivity of the photogenerated

charge carrier was probed by freely propagating single-cycle THz electromagnetic transients with 1–2 ps duration. The quickly oscillating terahertz field E(t) accelerated the charges, which, in turn, modifies the terahertz pulse. The relative modification $-\Delta E/E(t)$ of the THz field can be directly measured and related to the photoconductivity σ. The analysis was typically performed in the frequency domain by Fourier transformation, that is, $\sigma(\omega) \approx -\Delta E/E(\omega)$. The photoconductivity as a function of time delay t_d between excitation and THz pulse $\sigma(\omega;t_d)$ was a complex value, and its real part, $Re[\sigma(\omega;t_d)]$, corresponding to the changes in the peak intensity of THz pulse following photoexcitation, was directly related to the macroscopic transport parameters in electrical measurements, by $Re[\sigma(\omega ; t_d)] = N_{pump} \times e \times \mu(\omega ; t_d)$ where N_{pump} and $\mu(\omega; t_d)$ were the time-dependent carrier density and mobility following photoexcitation, respectively. Terahertz spectroscopy thus provides information on charge carrier dynamics on a timescale complementary to that obtained using time-resolved PL measurements (sub-ps versus ns).

EQE Measurements: Spectral response measurements were performed using an in-house built setup. A light beam from a Xenon/Quartz halogen source (Bemtham 610) was coupled into a monochromator (MSH-300), giving a coverage over the spectral range of 350 – 1800 nm. The light was chopped using a mechanical wheel (Bemtham 418) and the signal from the photodetectors were collected by using a current preamplifier (SR570) and a lock-in amplifier (SR810). A Si photodiode with a known responsivity was used for calibration. The samples were placed in a hermetically sealed holder to avoid their exposure to the ambient environment during measurements.

Current-Voltage Characterization: I-V sweeps were carried out in N_2, in a dark box environment using a Keithley 2400 source-meter. For the measurements performed under 1 sun (100 mW/cm^2) illumination, a class A Abet Sun 2000 solar simulator generating an AM1.5G spectrum was used. The light source of the solar simulator was calibrated using a Fraunhofer ISE certified silicon reference cell with KG3 filter.

4.4.3 Supporting Information for Results and Discussion

Table S1. ICP-OES characterization indicating the actual Rb doping ratio.

Sample	Pb (mmol)	Rb (mmol)	Rb/Pb ratio (%)
Rb-doped	7.14×10^{-2}	1.29×10^{-3}	1.8

Table S2. Summary of competitive literature reports on photodetectors based on $CsPbBr_3$ single crystals and thin films.

Material	Device structure	Responsivity (R) (light source, intensity, bias)	External quantum efficiency (EQE)	Ref
Single crystal	$Au/CsPbBr_3/Au$	2 AW^{-1} (535 nm, 5 V)	460%	39
Single crystal	$Au/CsPbBr_3/Au$	0.028 AW^{-1} (450 nm, 1 mW, 5 V)	7.00%	40
Single crystal	$Au/CsPbBr_3/Au$	2.5 AW^{-1}	6.2%	41
Single crystal	$Pt/CsPbBr_3/Au$	28 x 10^{-3} AW^{-1} (550 nm)	6%	42
Thin film	$Au/CsPbBr_3/Au$	0.18 AW^{-1}	41% (531 nm, 10 V)	43
Thin film	$Au/CsPbBr_3/Au$	55 AW^{-1}	16700%	31
Thin film	$NiO_x/CsPbBr_3/TiO_2$	0.22 AW^{-1}	-	44
Thin film	$Cr/Au/CsPbBr_3$	0.1072 AW^{-1}	25.4%	45
Thin film	$Au/CsPbBr_3/Au$ /Polyimide	0.1519 AW^{-1} (405 nm, 2 µW cm^{-2}, 0 V)	7.98% (405 nm, 0 V)	46

Table S3. Determination of the grain size and the phase purity of $CsPbBr_3$ films with $CsPb_2Br_5$ side phase and their influence on the mobility.

Grain size (µm)	Amount of $CsPbBr_3$ (%)	Amount of $CsPb_2Br_5$ (%)	Normalized Mobility
0.13	3	83	0.36
0.29	35.5	64.5	0.90
0.35	24	75.3	0.71
0.47	71	29	0.65
0.56	47	53	1
0.57	55.4	41	0.53

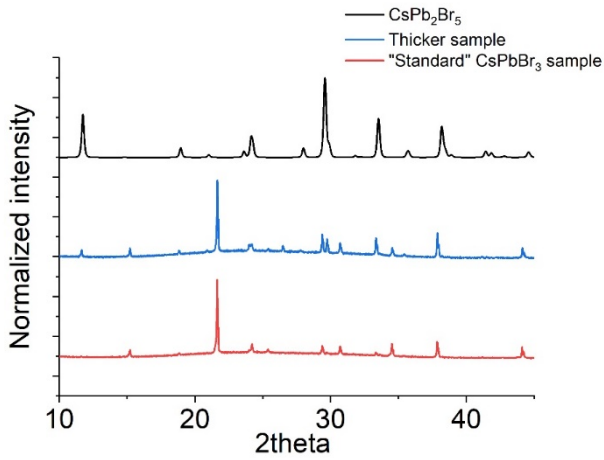

Figure S1. X-ray diffraction pattern (XRD) of a CVD grown sample, indicating the formation of orthorhombic $CsPbBr_3$ with a small amount of $CsPb_2Br_5$ as a side phase.

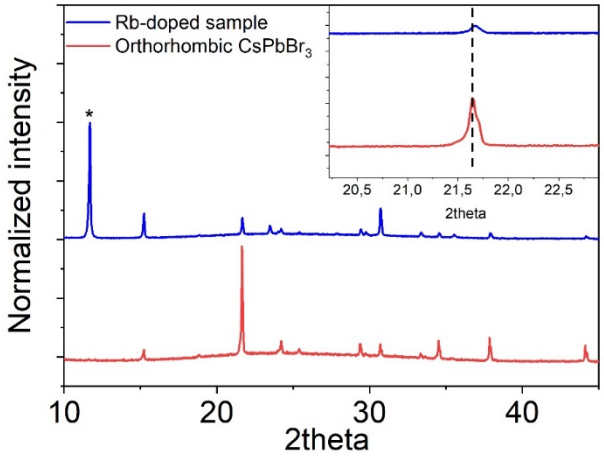

Figure S2. XRD pattern of the Rb-doped sample, indicating a small shift towards higher angles. Peaks arising from the $CsPb_2Br_5$ side phase are marked by *.

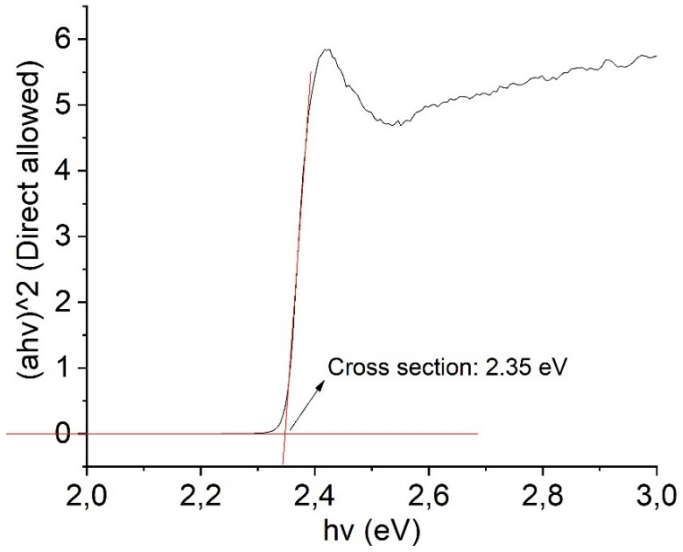

Figure S3. Tauc plot of a CVD-grown $CsPbBr_3$ sample, indicating a direct bandgap of 2.35 eV.

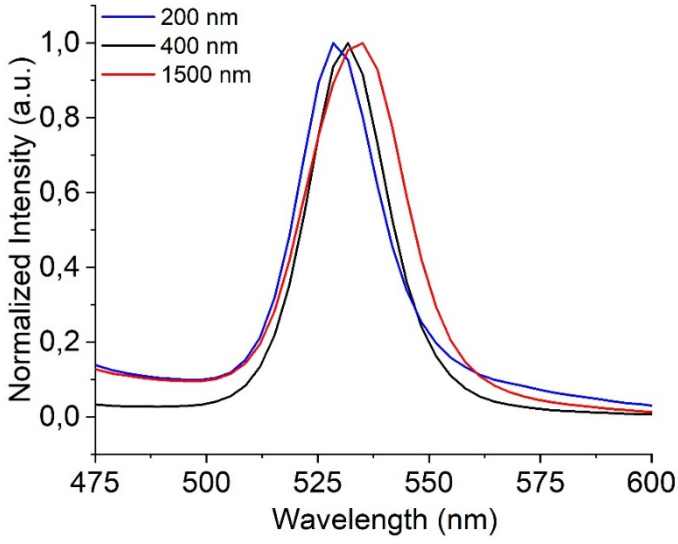

Figure S4. Red or blue shift in the photoluminescence depending on the increased or decreased thickness of the $CsPbBr_3$ film, respectively.

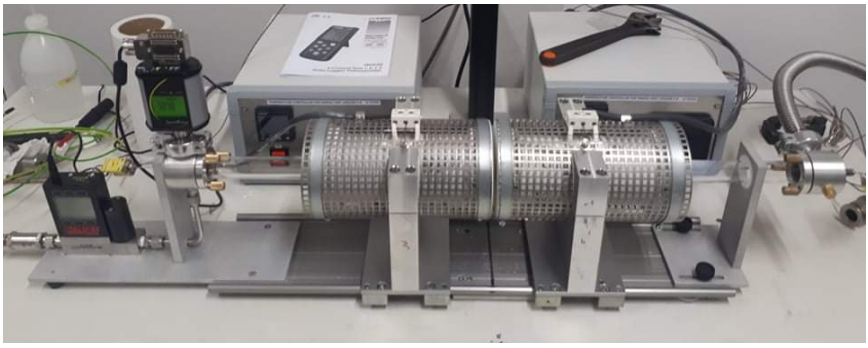

Figure S5. Home-built CVD setup at KU Leuven.

4.5 References

(1) Mahmud, M. A.; Duong, T.; Peng, J.; Wu, Y.; Shen, H.; Walter, D.; Nguyen, H. T.; Mozaffari, N.; Tabi, G. D.; Catchpole, K. R.; Weber, K. J.; White, T. P. Origin of Efficiency and Stability Enhancement in High-Performing Mixed Dimensional 2D-3D Perovskite Solar Cells: A Review. *Advanced Functional Materials* **2022**, *32* (3), 2009164. https://doi.org/10.1002/adfm.202009164.

(2) Bati, A. S. R.; Zhong, Y. L.; Burn, P. L.; Nazeeruddin, M. K.; Shaw, P. E.; Batmunkh, M. Next-Generation Applications for Integrated Perovskite Solar Cells. *Commun Mater* **2023**, *4* (1), 1–24. https://doi.org/10.1038/s43246-022-00325-4.

(3) Bhatia, H.; Ghosh, B.; Debroye, E. Colloidal FAPbBr3 Perovskite Nanocrystals for Light Emission: What's Going On? *J. Mater. Chem. C* **2022**. https://doi.org/10.1039/D2TC01373H.

(4) Van Le, Q.; Jang, H. W.; Kim, S. Y. Recent Advances toward High-Efficiency Halide Perovskite Light-Emitting Diodes: Review and Perspective. *Small Methods* **2018**, *2* (10), 1700419. https://doi.org/10.1002/smtd.201700419.

(5) Clinckemalie, L.; Valli, D.; Roeffaers, M. B. J.; Hofkens, J.; Pradhan, B.; Debroye, E. Challenges and Opportunities for CsPbBr3 Perovskites in Low- and High-Energy Radiation Detection. *ACS Energy Lett.* **2021**, *6* (4), 1290–1314. https://doi.org/10.1021/acsenergylett.1c00007.

(6) Wang, H.; Kim, D. H. Perovskite-Based Photodetectors: Materials and Devices. *Chem. Soc. Rev.* **2017**, *46* (17), 5204–5236. https://doi.org/10.1039/C6CS00896H.

(7) Kim, H.-S.; Lee, C.-R.; Im, J.-H.; Lee, K.-B.; Moehl, T.; Marchioro, A.; Moon, S.-J.; Humphry-Baker, R.; Yum, J.-H.; Moser, J. E.; Grätzel, M.; Park, N.-G. Lead Iodide Perovskite Sensitized All-Solid-State Submicron Thin Film Mesoscopic Solar Cell with Efficiency Exceeding 9%. *Sci Rep* **2012**, *2* (1), 591. https://doi.org/10.1038/srep00591.

(8) Burschka, J.; Pellet, N.; Moon, S.-J.; Humphry-Baker, R.; Gao, P.; Nazeeruddin, M. K.; Grätzel, M. Sequential Deposition as a Route to High-Performance Perovskite-Sensitized Solar Cells. *Nature* **2013**, *499* (7458), 316–319. https://doi.org/10.1038/nature12340.

(9) Yu, J. C.; Hong, J. A.; Jung, E. D.; Kim, D. B.; Baek, S.-M.; Lee, S.; Cho, S.; Park, S. S.; Choi, K. J.; Song, M. H. Highly Efficient and Stable Inverted Perovskite Solar Cell Employing PEDOT:GO Composite Layer as a Hole Transport Layer. *Sci Rep* **2018**, *8* (1), 1070. https://doi.org/10.1038/s41598-018-19612-7.

(10) Nie, W.; Tsai, H.; Asadpour, R.; Blancon, J.-C.; Neukirch, A. J.; Gupta, G.; Crochet, J. J.; Chhowalla, M.; Tretiak, S.; Alam, M. A.; Wang, H.-L.; Mohite, A. D. Solar Cells. High-Efficiency Solution-Processed

Perovskite Solar Cells with Millimeter-Scale Grains. *Science* **2015**, *347* (6221), 522–525. https://doi.org/10.1126/science.aaa0472.

(11) Yuan, H.; Debroye, E.; Janssen, K.; Naiki, H.; Steuwe, C.; Lu, G.; Moris, M.; Orgiu, E.; Uji-i, H.; De Schryver, F.; Samorì, P.; Hofkens, J.; Roeffaers, M. Degradation of Methylammonium Lead Iodide Perovskite Structures through Light and Electron Beam Driven Ion Migration. *J. Phys. Chem. Lett.* **2016**, *7* (3), 561–566. https://doi.org/10.1021/acs.jpclett.5b02828.

(12) Mo, X.; Li, X.; Dai, G.; He, P.; Sun, J.; Huang, H.; Yang, J. All-Inorganic Perovskite CsPbBr3 Microstructures Growth via Chemical Vapor Deposition for High-Performance Photodetectors. *Nanoscale* **2019**, *11* (44), 21386–21393. https://doi.org/10.1039/C9NR06682A.

(13) Chemical Vapor Deposition. In *Handbook of Nanophase and Nanostructured Materials*; Wang, Z. L., Liu, Y., Zhang, Z., Eds.; Springer US: Boston, MA, 2002; pp 102–144. https://doi.org/10.1007/0-387-23814-X_5.

(14) Nasi, L.; Calestani, D.; Mezzadri, F.; Mariano, F.; Listorti, A.; Ferro, P.; Mazzeo, M.; Mosca, R. All-Inorganic CsPbBr3 Perovskite Films Prepared by Single Source Thermal Ablation. *Frontiers in Chemistry* **2020**, *8*.

(15) Wang, S.; Ono, L. K.; Leyden, M. R.; Kato, Y.; Raga, S. R.; Lee, M. V.; Qi, Y. Smooth Perovskite Thin Films and Efficient Perovskite Solar Cells Prepared by the Hybrid Deposition Method. *J. Mater. Chem. A* **2015**, *3* (28), 14631–14641. https://doi.org/10.1039/C5TA03593G.

(16) Zhou, Y.; Fernando, K.; Wan, J.; Liu, F.; Shrestha, S.; Tisdale, J.; Sheehan, C. J.; Jones, A. C.; Tretiak, S.; Tsai, H.; Huang, H.; Nie, W. Millimeter-Size All-Inorganic Perovskite Crystalline Thin Film Grown by Chemical Vapor Deposition. *Advanced Functional Materials* **2021**, *31* (23), 2101058. https://doi.org/10.1002/adfm.202101058.

(17) Babayigit, A.; Ethirajan, A.; Muller, M.; Conings, B. Toxicity of Organometal Halide Perovskite Solar Cells. *Nature Mater* **2016**, *15* (3), 247–251. https://doi.org/10.1038/nmat4572.

(18) Pedersen, H.; Elliott, S. D. Studying Chemical Vapor Deposition Processes with Theoretical Chemistry. *Theor Chem Acc* **2014**, *133* (5), 1476. https://doi.org/10.1007/s00214-014-1476-7.

(19) Carlsson, J.-O.; Martin, P. M. Chapter 7 - Chemical Vapor Deposition. In *Handbook of Deposition Technologies for Films and Coatings (Third Edition)*; Martin, P. M., Ed.; William Andrew Publishing: Boston, 2010; pp 314–363. https://doi.org/10.1016/B978-0-8155-2031-3.00007-7.

(20) Sabzi, M.; Mousavi Anijdan, S. H.; Shamsodin, M.; Farzam, M.; Hojjati-Najafabadi, A.; Feng, P.; Park, N.; Lee, U. A Review on Sustainable Manufacturing of Ceramic-Based Thin Films by Chemical Vapor Deposition (CVD): Reactions Kinetics and the Deposition Mechanisms.

Coatings **2023**, *13* (1), 188. https://doi.org/10.3390/coatings13010188.

(21) Leyden, M. R.; Jiang, Y.; Qi, Y. Chemical Vapor Deposition Grown Formamidinium Perovskite Solar Modules with High Steady State Power and Thermal Stability. *J. Mater. Chem. A* **2016**, *4* (34), 13125–13132. https://doi.org/10.1039/C6TA04267H.

(22) Sanders, S.; Simkus, G.; Riedel, J.; Ost, A.; Schmitz, A.; Muckel, F.; Bacher, G.; Heuken, M.; Vescan, A.; Kalisch, H. Showerhead-Assisted Chemical Vapor Deposition of CsPbBr3 Films for LED Applications. *Journal of Materials Research* **2021**, *36* (9), 1813–1823. https://doi.org/10.1557/s43578-021-00239-w.

(23) Nagel, S. R.; MacChesney, J. B.; Walker, K. L. An Overview of the Modified Chemical Vapor Deposition (MCVD) Process and Performance. *IEEE TRANSACTIONS ON MICROWAVE THEORY AND TECHNIQUES* **1982**, No. 4.

(24) Park, J.-H.; Sudarshan, T. S. *Chemical Vapor Deposition*; ASM International, 2001.

(25) Hersee, S. D.; Duchemin, J. P. Low-Pressure Chemical Vapor Deposition. *Annual Review of Materials Science* **1982**, *12* (1), 65–80. https://doi.org/10.1146/annurev.ms.12.080182.000433.

(26) A. Raiford, J.; T. Oyakhire, S.; F. Bent, S. Applications of Atomic Layer Deposition and Chemical Vapor Deposition for Perovskite Solar Cells. *Energy & Environmental Science* **2020**, *13* (7), 1997–2023. https://doi.org/10.1039/D0EE00385A.

(27) Keshavarz, M.; Debroye, E.; Ottesen, M.; Martin, C.; Zhang, H.; Fron, E.; Küchler, R.; Steele, J. A.; Bremholm, M.; Van de Vondel, J.; Wang, H. I.; Bonn, M.; Roeffaers, M. B. J.; Wiedmann, S.; Hofkens, J. Tuning the Structural and Optoelectronic Properties of Cs2AgBiBr6 Double-Perovskite Single Crystals through Alkali-Metal Substitution. *Advanced Materials* **2020**, *32* (40), 2001878. https://doi.org/10.1002/adma.202001878.

(28) Stoumpos, C. C.; Malliakas, C. D.; Peters, J. A.; Liu, Z.; Sebastian, M.; Im, J.; Chasapis, T. C.; Wibowo, A. C.; Chung, D. Y.; Freeman, A. J.; Wessels, B. W.; Kanatzidis, M. G. Crystal Growth of the Perovskite Semiconductor CsPbBr3: A New Material for High-Energy Radiation Detection. *Crystal Growth & Design* **2013**, *13* (7), 2722–2727. https://doi.org/10.1021/cg400645t.

(29) Tong, G.; Jiang, M.; Son, D.-Y.; Qiu, L.; Liu, Z.; Ono, L. K.; Qi, Y. Inverse Growth of Large-Grain-Size and Stable Inorganic Perovskite Micronanowire Photodetectors. *ACS Appl. Mater. Interfaces* **2020**, *12* (12), 14185–14194. https://doi.org/10.1021/acsami.0c01056.

(30) Li, J.; Du, X.; Niu, G.; Xie, H.; Chen, Y.; Yuan, Y.; Gao, Y.; Xiao, H.; Tang, J.; Pan, A.; Yang, B. Rubidium Doping to Enhance Carrier Transport in CsPbBr3 Single Crystals for High-Performance X-Ray Detection. *ACS*

Appl. Mater. Interfaces **2020**, *12* (1), 989–996. https://doi.org/10.1021/acsami.9b14772.

(31) Li, Y.; Shi, Z.-F.; Li, S.; Lei, L.-Z.; Ji, H.-F.; Wu, D.; Xu, T.-T.; Tian, Y.-T.; Li, X.-J. High-Performance Perovskite Photodetectors Based on Solution-Processed All-Inorganic CsPbBr3 Thin Films. *J. Mater. Chem. C* **2017**, *5* (33), 8355–8360. https://doi.org/10.1039/C7TC02137B.

(32) Nikl, M.; Nitsch, K.; Mihóková, E.; Polák, K.; Fabeni, P.; Pazzi, G. P.; Gurioli, M.; Santucci, S.; Phani, R.; Scacco, A.; Somma, F. Luminescence of CsPbBr3-like Quantum Dots in CsBr Single Crystals. *Physica E: Low-dimensional Systems and Nanostructures* **1999**, *4* (4), 323–331. https://doi.org/10.1016/S1386-9477(99)00016-8.

(33) Protesescu, L.; Yakunin, S.; Bodnarchuk, M. I.; Krieg, F.; Caputo, R.; Hendon, C. H.; Yang, R. X.; Walsh, A.; Kovalenko, M. V. Nanocrystals of Cesium Lead Halide Perovskites (CsPbX3, X = Cl, Br, and I): Novel Optoelectronic Materials Showing Bright Emission with Wide Color Gamut. *Nano Lett.* **2015**, *15* (6), 3692–3696. https://doi.org/10.1021/nl5048779.

(34) Ulbricht, R.; Hendry, E.; Shan, J.; Heinz, T. F.; Bonn, M. Carrier Dynamics in Semiconductors Studied with Time-Resolved Terahertz Spectroscopy. *Rev. Mod. Phys.* **2011**, *83* (2), 543–586. https://doi.org/10.1103/RevModPhys.83.543.

(35) Zhang, Y.; Gao, L.; Wei, X.; Zhao, W.; Wang, W.; Wang, M.; Zheng, T.; Liu, H.; Lu, J.; Ni, Z. Spectroscopic Perception of Trap States on the Performance of Methylammonium and Formamidinium Lead Iodide Perovskite Solar Cells. *Adv Mater* **2021**, *33* (38), e2102241. https://doi.org/10.1002/adma.202102241.

(36) Zhang, H.; Debroye, E.; Zheng, W.; Fu, S.; Virgilio, L. D.; Kumar, P.; Bonn, M.; Wang, H. I. Highly Mobile Hot Holes in Cs2AgBiBr6 Double Perovskite. *Science Advances* **2021**, *7* (52), eabj9066. https://doi.org/10.1126/sciadv.abj9066.

(37) Zhao, Y.; Li, C.; Shen, L. Recent Advances on Organic-Inorganic Hybrid Perovskite Photodetectors with Fast Response. *InfoMat* **2019**, *1* (2), 164–182. https://doi.org/10.1002/inf2.12010.

(38) Zhang, Z.; Zhu, Y.; Wang, W.; Zheng, W.; Lin, R.; Huang, F. Growth, Characterization and Optoelectronic Applications of Pure-Phase Large-Area CsPb2Br5 Flake Single Crystals. *J. Mater. Chem. C* **2018**, *6* (3), 446–451. https://doi.org/10.1039/C7TC04834C.

(39) Song, J.; Cui, Q.; Li, J.; Xu, J.; Wang, Y.; Xu, L.; Xue, J.; Dong, Y.; Tian, T.; Sun, H.; Zeng, H. Ultralarge All-Inorganic Perovskite Bulk Single Crystal for High-Performance Visible–Infrared Dual-Modal Photodetectors. *Advanced Optical Materials* **2017**, *5* (12), 1700157. https://doi.org/10.1002/adom.201700157.

(40) Ding, J.; Du, S.; Zuo, Z.; Zhao, Y.; Cui, H.; Zhan, X. High Detectivity and Rapid Response in Perovskite CsPbBr3 Single-Crystal Photodetector.

J. Phys. Chem. C **2017**, *121* (9), 4917–4923. https://doi.org/10.1021/acs.jpcc.7b01171.

(41) Yang, Z.; Xu, Q.; Wang, X.; Lu, J.; Wang, H.; Li, F.; Zhang, L.; Hu, G.; Pan, C. Large and Ultrastable All-Inorganic CsPbBr3 Monocrystalline Films: Low-Temperature Growth and Application for High-Performance Photodetectors. *Advanced Materials* **2018**, *30* (44), 1802110. https://doi.org/10.1002/adma.201802110.

(42) Saidaminov, M. I.; Haque, M. A.; Almutlaq, J.; Sarmah, S.; Miao, X.-H.; Begum, R.; Zhumekenov, A. A.; Dursun, I.; Cho, N.; Murali, B.; Mohammed, O. F.; Wu, T.; Bakr, O. M. Inorganic Lead Halide Perovskite Single Crystals: Phase-Selective Low-Temperature Growth, Carrier Transport Properties, and Self-Powered Photodetection. *Advanced Optical Materials* **2017**, *5* (2), 1600704. https://doi.org/10.1002/adom.201600704.

(43) Li, X.; Yu, D.; Cao, F.; Gu, Y.; Wei, Y.; Wu, Y.; Song, J.; Zeng, H. Healing All-Inorganic Perovskite Films via Recyclable Dissolution–Recyrstallization for Compact and Smooth Carrier Channels of Optoelectronic Devices with High Stability. *Advanced Functional Materials* **2016**, *26* (32), 5903–5912. https://doi.org/10.1002/adfm.201601571.

(44) Ji, Z.; Cen, G.; Su, C.; Liu, Y.; Zhao, Z.; Zhao, C.; Mai, W. All-Inorganic Perovskite Photodetectors with Ultrabroad Linear Dynamic Range for Weak-Light Imaging Applications. *Advanced Optical Materials* **2020**, *8* (23), 2001436. https://doi.org/10.1002/adom.202001436.

(45) Bao, C.; Peng, X.; Ying, L.; Mei, Y.; Zhang, B.; Long, H. Two-Step Spin Coating $CsPbBr_3$ Thin Films and Photodetectors in the Atmosphere. *Opt. Lett., OL* **2023**, *48* (9), 2472–2475. https://doi.org/10.1364/OL.485858.

(46) Zhao, Z.; Tang, W.; Zhang, S.; Ding, Y.; Zhao, X.; Yuan, G. Flexible Self-Powered Vertical Photodetectors Based on the [001]-Oriented CsPbBr3 Film. *J. Phys. Chem. C* **2023**, *127* (10), 4846–4852. https://doi.org/10.1021/acs.jpcc.2c08845.

Chapter 5
Transformation of $Cs_3Bi_2Br_9$ to $Cs_2AgBiBr_6$ Lead-Free Perovskite Microcrystals Through Cation Exchange

This chapter is based on: *Adv Opt. Mater.* 2023, 2300578

Lotte Clinckemalie, Rafikul Ali Saha, Donato Valli, Eduard Fron, Maarten B.J. Roeffaers, Johan Hofkens, Bapi Pradhan and Elke Debroye**

Copyright © 2023 Wiley-VCH GmbH

Reproduced with permission according to the Copyright Transfer Agreement

Author contributions:

L.C. conducted most of the experiments and their analysis, and wrote the manuscript under the supervision of J.H., B.P. and E.D. L.C. and D.V. measured In-situ UV-Vis diffuse reflectance spectra. R.A.S. performed X-ray diffraction analysis and refinement under the supervision of M.B.J.R. D.V. conducted the Raman experiments and fabricated and analyzed the photodetector devices. E.F. completed the time-resolved spectroscopy as well as the analysis. The research line presented in the manuscript was conceived by M.B.J.R., J.H., B.P. and E.D.

Situation in this PhD Dissertation

Pb-based MHPs have shown great promise as a semiconductor material for optoelectronics. However, their stability, processability as large-area layers and eco-toxicity have hampered their commercial usage. In this PhD dissertation, we investigated several ways to conquer these problems. This chapter focusses on the eco-toxicity by opening a new synthesis pathway to easily fabricate high-quality $Cs_2AgBiBr_6$ lead-free perovskite microcrystals.

Abstract

All-inorganic lead-free $Cs_2AgBiBr_6$ double perovskites have gained significant attention due to their potential as stable and nontoxic photoactive semiconductors. Currently, it remains challenging to synthesize homogeneous microcrystals exhibiting excellent properties, which are necessary for large-area device integration. In this work, we propose a two-step synthesis approach involving the introduction of a foreign silver cation to transform the 0D layered $Cs_3Bi_2Br_9$ to 3D $Cs_2AgBiBr_6$ perovskite structure. We have studied the cation exchange transformation mechanism by isolating intermediates to be able to follow the evolution of the crystal lattice as well as the structural and optical properties over time. Moreover, complete cation exchange resulted in phase-pure, highly crystalline $Cs_2AgBiBr_6$ microcrystals exhibiting excellent photonic properties, superior to their counterparts synthesized by anti-solvent precipitation. Our findings highlight the potential of cation exchange-induced transformation as a means of synthesizing novel, stable perovskites.

5.1 Introduction

Metal halide perovskites have gained considerable attraction as promising semiconductors, since they exhibit exceptional optoelectronic properties such as a high visible absorption,[1] high carrier mobility[2] and long electron-hole diffusion lengths.[3] Due to their interesting properties and the easy compositional and morphological tunability, different perovskite compounds are being intensively studied in different applications such as solar cells,[4] light emission applications (LEDs),[5] photocatalytic hydrogen evolution and CO_2 reduction[6] and even X-ray and photodetection.[7]

Bi-based lead-free perovskites not only avoid the use of the toxic element Pb, but also exhibit much improved air and moisture stability.[8,9] This increase in stability arises from the better defined cubic phase of the corresponding perovskite structure and the high dielectric constant of Bi^{III}, which ensures efficient screening of charged defects within the material.[10] Initially, $Cs_3Bi_2Br_9$ was intensely studied and revealed interesting properties such as strong exciton-phonon coupling[11] and excellent photocatalytic performance.[12] However, the wide bandgap inherent to the material limits further optoelectronic applications.

The double perovskite (DP), $Cs_2AgBiBr_6$, has been found to be a promising material, as single crystals have been demonstrated to exhibit a high X-ray sensitivity and low detection limit.[13–16] Currently, it is still challenging to synthesize homogeneous microcrystals with a dimension of ~10-20 µm exhibiting similar properties as the single crystal counterparts. Such microcrystals are necessary for the implementation in thin, or compact thick film (~100 µm) devices. Therefore, it is necessary to keep exploring new synthesis routes to obtain the required high-quality crystals with dimensions which, depending on the application, are in the nano- or micrometer range.

To expand the synthetic range of ionic perovskites, structural transformation by the introduction of a foreign ion can be a promising approach. This slower, two-step synthesis procedure enables more control over the synthesis process compared to faster, direct synthesis pathways.[17] Moreover, control over the crystal structure is an important strategy for tuning the chemical and physical properties of perovskite materials. Ultimately, this transformation process can offer pathways to the discovery and development of difficult-to-access perovskite structures. However, more research is necessary to understand the critical factors that control the crystal structure transformation.

In this paper, it is shown that structural transformation via ion exchange is a promising route for overcoming current shortcomings in quality control by direct synthetic routes. So far, MHPs are mostly anion exchanged to tune the bandgap and photoluminescence (PL)[18,19] and only a few reports deal with the effect of cation exchange (CE).[20–22] We investigated how exposure of the 0D layered $Cs_3Bi_2Br_9$ to silver ions induces the transformation to the 3D $Cs_2AgBiBr_6$ perovskites. The crystal lattice transformation was followed through the synthesis of intermediates, which allows for an in-depth study of the changes in structural and optical properties over time. Moreover, this resulted in phase-pure, highly crystalline $Cs_2AgBiBr_6$ microcrystals with excellent photonic properties. This crystallographic transformation may pave pathway for the development of novel halide perovskites, which are not available via direct solution-based synthesis pathways.

5.2 Results and Discussion

The $Cs_3Bi_2Br_9$ microcrystals are synthesized using a solution-processed method.[23] A stoichiometric molar ratio of CsBr (1 mmol) and $BiBr_3$ (0.66 mmol) is separately dissolved in respectively 1 mL and 2 mL of 48 w% HBr by sonication, after which the two solutions are simultaneously added to 4 mL of 48 w% HBr under ambient conditions and constant stirring. This results in the immediate formation of cubic-shaped $Cs_3Bi_2Br_9$ perovskite microcrystals with an average size of approx. 10 µm (Figure 1a).

The crystal structure of $Cs_3Bi_2Br_9$ was determined by performing a Rietveld refinement[24] of the obtained X-ray diffraction (XRD) pattern, as shown in Figure 1b. The corresponding lattice parameters, atomic positions, site occupancy and reduced χ^2 values indicating the fitting accuracy, are listed in Table S1. The XRD pattern of $Cs_3Bi_2Br_9$ has been fitted by considering a trigonal crystal phase system with a P-*3m1* space group, containing one formula unit per unit cell. It forms a layered structure where Cs and Bi are in cuboctahedron and octahedron coordination respectively, as seen in Figure 1c.

A 2x molar ratio (1 mmol) of Ag^+ ions, in the form of AgBr, are added to the preformed $Cs_3Bi_2Br_9$ microcrystals, which induces a gradual color change from yellow to dark orange (Figure S1). SEM imaging of the final product shows a morphology transformation from cubic-shaped towards octahedral-shaped crystals, suggesting the formation of the $Cs_2AgBiBr_6$ double perovskite (Figure 1d). The XRD pattern of the final product confirms phase purity, and structural refinement has been performed by considering a cubic crystal

structure with a F*m-3m* space group, which is consistent with literature (Figure 1e).[25,26] The refined structural parameters, including lattice constants, atomic positions, site occupancy, along with the reduced χ^2 values are listed in Table S2. The refined crystal structure shows corner-shared $BiBr_6$ and $AgBr_6$ octahedra, forming the well-known rock-salt ordering (Figure 1f).

This confirms that the introduction of Ag^+ to $Cs_3Bi_2Br_9$ induces the cation exchange transformation towards the double perovskite via following reaction (Scheme S1):

$$2\ Cs_3Bi_2Br_9 + 3\ Ag^+ \rightarrow 3\ Cs_2AgBiBr_6 + Bi^{3+}$$

Different quantities of AgBr (0.75 mmol, 1 mmol and 1.5 mmol) are added to the mixture (See experimental section for more details) to study the amount of required Ag^+ to fully convert the ternary to quaternary double perovskite phase. Throughout this manuscript, we use the introduction of 1 mmol AgBr as a reference and study it in detail. Furthermore, a higher (1.5 mmol) and a lower (0.75 mmol) amount are used to reveal the relation between the amount of Ag^+ ions and the phase transformation kinetics. The conversion after adding 0.75 mmol, 1 mmol and 1.5 mmol of AgBr is complete after 60 min, 30 min and 15 min, respectively.

In order to study the evolution of the structural and optical characteristics during the transformation, intermediates are isolated by stopping the reaction at several time intervals. This is achieved by filtering out the solvent and then vacuum drying the resulting powder at room temperature. When the intermediates are dried under vacuum (~50 mbar) at 60 °C, the color of powder changes from yellow to orange. This implies that the CE transformation on the solid-state powders of these ionic compounds can be thermally re-activated.

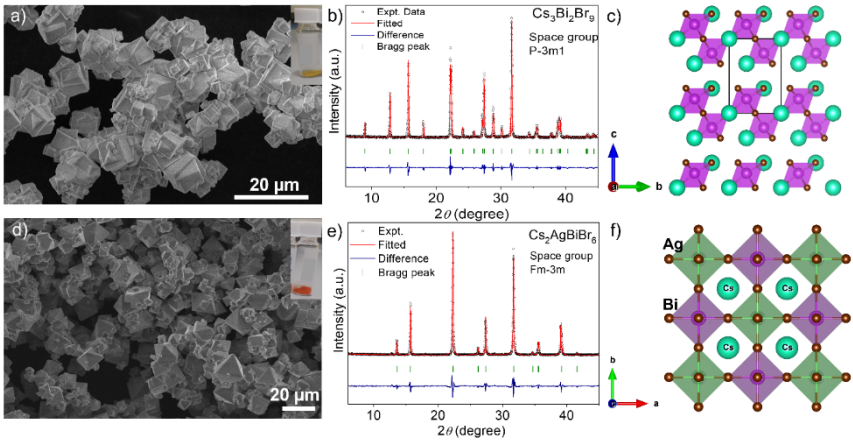

Figure 1. a) Scanning electron microscope (SEM) images of the $Cs_3Bi_2Br_9$ perovskite. b) Rietveld refinement on powder X-ray diffraction (XRD) pattern, revealing that $Cs_3Bi_2Br_9$ exhibits a trigonal crystal phase. c) Corresponding layered structure of the trigonal $Cs_3Bi_2Br_9$ perovskite. d) SEM images of the $Cs_2AgBiBr_6$ double perovskite. e) Rietveld refinement on XRD pattern, revealing the cubic crystal structure of the $Cs_2AgBiBr_6$ perovskite. f) Corresponding cubic crystal structure of the $Cs_2AgBiBr_6$ perovskite.

An in-depth study of the evolution of the crystal lattice upon Ag cation addition was performed through the analysis of the powder XRD patterns of all intermediates (Figure S2). From the peak evolution in the pattern, it can be concluded that the transition from the trigonal to the cubic phase occurs and that the cubic crystal lattice is formed without the formation of side phases. Analysis of the intermediates of the transformations with different quantities of Ag^+ ions revealed that when a lower amount of AgBr (0.75 mmol) is used, the phase transition is not complete due to the low amount of Ag^+ ions present in solution. However, when more Ag^+ is added (1 mmol and 1.5 mmol), a complete and homogeneous transformation from a trigonal $Cs_3Bi_2Br_9$ to a cubic $Cs_2AgBiBr_6$ crystal lattice can be observed.

During the homogeneous transformation for 1 mmol and 1.5 mmol of AgBr, all intermediate samples are studied using Rietveld refinement analysis, considering both the trigonal and cubic crystal phase. This revealed changes in the crystal lattice parameters and quantified the relative percentage of each crystal structure at each intermediate stage of the transformation process. For the trigonal crystal phase of the $Cs_3Bi_2Br_9$ crystals, only small changes in the lattice parameters can be observed until 10 minutes (Figure 2a-b). This can be

expected since after 10 minutes, the crystals still exhibit around 85% of the trigonal phase and only 15% of the cubic phase is formed (Figure S3). It can thus be concluded that for this reaction, the initial growth rate is slow in the first 10 minutes. This can be explained by the "all-or-nothing" behavior, described by De Trizio *et al.*[21], in which first intercalation of Ag^+ into the layered $Cs_3Bi_2Br_9$ takes place.[27,28] Once a critical number of Ag^+ ions (~15%) is incorporated in the structure, it activates the crystals for further transformation via CE and an abrupt phase transformation towards the double perovskite phase is observed. As a result, the rate of transformation to the cubic phase increases after 10 minutes and the contribution of the cubic phase increases from 15% to 95%. A solid-state reaction was also performed by homogeneously grinding the precursor agents (for more details, see SI) to further confirm the cation exchange-induced transformation (Figure S4). In this experiment, a (partial) transition towards the double perovskite MCs was observed, indicating that the CE transition can happen without the presence of solvent. However, dissolution-recrystallization cannot be ruled out completely, given that both cation exchange and recrystallization occur at the same timescale.[29] During the transformation, the trigonal unit cell expands in the a and b directions, while contracting in the c direction. At the same time, the unit cell of the cubic phase expands as a logical consequence of the formation of the cubic $Cs_2AgBiBr_6$ double perovskite crystals (Figure 2d). An anomaly can be observed at around 15 min in both the time dependent lattice parameters as well as in the unit cell volume variations (Figure 2c). This behavior is considered to be a consequence of the phase conversion, in which the growth of the second phase is in competition with the suppression of the first.[30,31]

The graph of the degree of phase transformation (Figure 2f) is fitted using the Avrami equation to extract the growth kinetics parameters during the phase transformation at a fixed temperature:

$$y = 1 - \exp[-Kt^n]$$

where K is the conversion rate constant, t is the reaction time and n is the Avrami exponent. The value n reflects the nature of the transformation, more specifically, it determines the dimensionality of growth and the nature of the nucleation (homogeneous or heterogeneous).[32,33] However, in this case, the fitting results in n = 4 (3+1), which indicates that the ternary to quaternary perovskite nucleation is spherulitic (3-dimensional) and homogeneous.[34] Furthermore, the calculated kinetic rate corresponds to K = 10^{-6} min^{-4} and 10^{-4} min^{-4} for a lower (1 mmol) and higher (1.5 mmol) amount of AgBr, respectively. It can thus be stated that the phase transformation continues to

happen homogeneously (n~4) in 3 dimensions, but significantly faster (K) with a higher number of Ag^+ ions. Powder XRD thus reveals that the amount of Ag^+ controls the kinetics of the reaction, as well as whether the phase transformation is complete and homogeneous.

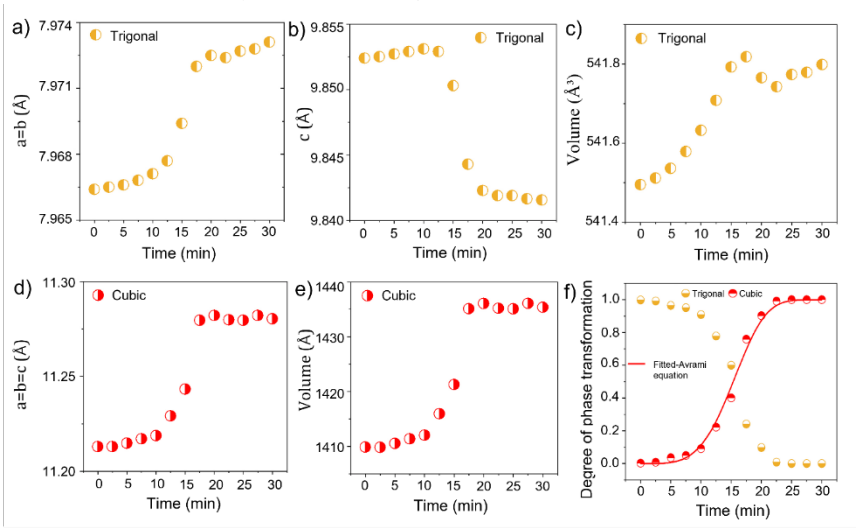

Figure 2. XRD analysis of the transformation via intermediates. a-b) Evolution in the time-dependent lattice parameters of the trigonal crystal phase. c) Variations in the unit cell volume of the trigonal crystal phase. d) Evolution in the time-dependent lattice parameters of the cubic crystal phase. e) Variations in the unit cell volume of the cubic crystal phase. f) Graph of the degree of phase transformation, fitted with the Avrami equation to extract the growth kinetics at a fixed temperature of 25 °C.

Raman spectroscopic analysis of the starting, intermediate and end products further confirms that the phase evolution consists of a transformation from pure $Cs_3Bi_2Br_9$ to pure $Cs_2AgBiBr_6$ upon the addition of AgBr. The spectra recorded on all intermediates show that the peaks assigned to the $Cs_3Bi_2Br_9$ perovskite gradually disappear, while the newly emerging peaks, belonging to the $Cs_2AgBiBr_6$ double perovskite, are the only remaining peaks in the final compound (Figure 3a). At the beginning of the conversion, five peaks can be observed in the Raman spectrum. Based on previous literature reports, these peaks can be assigned to vibrational modes from the sublattice consisting of the $BiBr_6$ octahedra in the trigonal crystal structure of $Cs_3Bi_2Br_9$.[35,36] The lower energy peaks belong to the bending modes, while the higher energy ones belong to the A_{1g} (165 cm^{-1}) and E_g (190 cm^{-1}) stretching modes of these $BiBr_6$ octahedra. Only for the higher energy part of the spectrum, clear

assignments of the peaks with their relative symmetries were reported (Figure 3a, dotted outline). Since this coincides with the region where we observe the largest differences with time, we will focus on that part of the Raman spectra. The conversion process clearly evolves to, as expected, a decrease in the intensities of the peaks related to the $Cs_3Bi_2Br_9$ phase, while the ones due to the double perovskite lattice vibrations start to appear. It is particularly visible that the A^{1g} (176 cm^{-1}) and E_g (133 cm^{-1}) stretching modes due to the $AgBr_6$ octahedra in the double perovskite structure are the dominating modes toward the end of the conversion process.[37]

Therefore, the results from the time-dependent Raman spectroscopy analysis are in line with the pXRD data and it has been confirmed that the transformation does not occur via any side phase. Furthermore, both techniques demonstrate that it takes some time to reach a critical point (~15% Ag^+ incorporation, Figure S3), after which the double perovskites starts to form. With the help of XRD, we attributed this to the time required for a significant number of Ag ions to incorporate to form the double perovskite structure, after which the complete conversion reaction happens almost instantaneously.

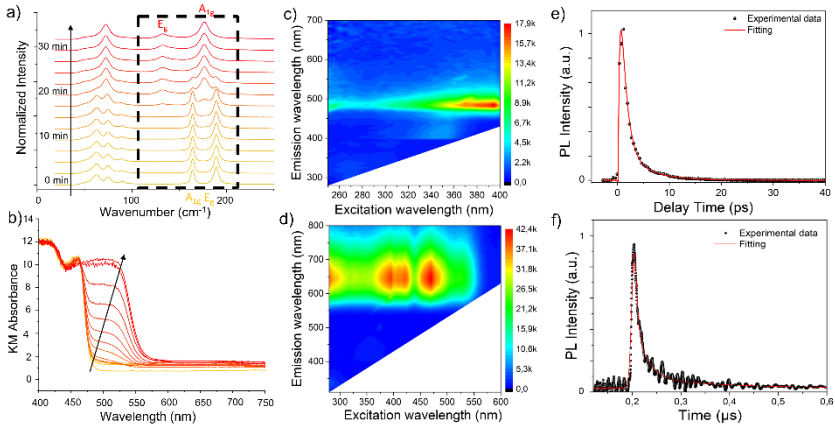

Figure 3. Time-dependent a) Raman spectra and b) UV-Vis diffuse reflectance spectra during the transformation from 0 to 30 min. c) PL emission map of the $Cs_3Bi_2Br_9$ perovskite. d) PL emission map of the $Cs_2AgBiBr_6$ perovskite. e) fs fluorescence up-conversion decay trace (black) and the corresponding fit (red) of $Cs_2AgBiBr_6$ (λ_{exc} = 400 nm, λ_{em} = 650 nm) and f) Luminescence decay trace (black) of $Cs_2AgBiBr_6$ and the corresponding fit (red) (λ_{exc} = 410 nm, λ_{em} = 650 nm).

In-situ UV-Vis diffuse reflectance spectra are measured, after which the corresponding absorbance values are calculated by using the Kubelka-Munk theory (Figure 3b). Furthermore, Tauc plots are made to quantify and study the change in the bandgap energy (Figure S5). Initially, the absorption edge of the $Cs_3Bi_2Br_9$ crystals is observed at 465 nm, corresponding to a direct bandgap of 2.60 eV, which is in agreement with literature.[11,38] After the transformation, the absorption edge shifts to 525 nm, corresponding to an indirect bandgap of 2.20 eV, indicating the formation of $Cs_2AgBiBr_6$.[15] The intermediate samples exhibit the presence of both bandgaps. It should be emphasized that there is no appearance of an intermediate bandgap value, which is another indication that no side phases are formed.

Steady state and time-resolved photoluminescence (PL) spectra are recorded to investigate the difference in PL and photogenerated carrier properties. For the $Cs_3Bi_2Br_9$ perovskite crystals, steady state PL spectra show a PL maximum at 480 nm (2.6 eV) (PLQY < 1%) (Figure 3c), after which it redshifts to a PL maximum of 650 nm (1.9 eV) for the $Cs_2AgBiBr_6$ compound (PLQY < 1%) (Figure 3d), in line with literature.[38,39] The PL peak of $Cs_3Bi_2Br_9$ almost coincides with the bandgap value of 2.60 eV, so it can be attributed to near band emission. However, the PL peak of the final $Cs_2AgBiBr_6$ exhibits a significant Stokes shift relative to the bandgap value of 2.20 eV. This can either be due to the existence of a sub-bandgap due to defect states or due to phonon-assisted processes.[37,40]

To gain insight on the excited state dynamics and, indirectly, on the change in charge carrier dynamics induced by the cation exchange process, we carried out time-resolved luminescence in the fs-to-µs time range. In the beginning of the reaction, the luminescence of $Cs_3Bi_2Br_9$ is quenched by the presence of defects and exhibits a very fast decay of 180 fs, suggesting an ultrafast trap-assisted charge recombination process (Figure S6). Upon the formation of the double perovskite phase, the fs luminescence decay can be fitted with three time constants (τ_1 = 300 fs, τ_2 = 1.1 ps, τ_3 = 4.9 ps) (Figure 3e). The 300-fs component appears as a rise (negative amplitude), indicating the formation of an emitting species, most likely excitons. The formed excitons further undergo two relaxation processes on the ps time scale (1.1 and 4.9 ps) and populate electronic states characterized by longer lifetimes, giving a first hint to a decreased quenching. Since the bandgap of this material is indirect and recombination of the exciton happens in a slightly larger timescale due to carrier-phonon interactions, only few photons can be detected in the 100-fs time window (optical gate window).[37] However, the luminescent decay of these species have been observed with a different setup, suitable for

acquiring luminescence signal in the ns-µs range. Using this setup, the luminescence was found to decay with two time constants; a short (τ_4 = 22.5 ns, 86% contribution) and a long one (τ_5 = 160 ns, 14% contribution) (Figure 3f). The presence of such long lifetimes clearly suggests that the recombination dynamics are dramatically slowed down as a result of lower trap density and potentially a beneficial shielding of the charge carriers (e.g. by polaron formation).[41,42] The carrier lifetime improvement is rather substantial when compared to $Cs_3Bi_2Br_9$ where no or very limited carriers could be generated. Furthermore, these results are consistent with literature,[43] indicating the quality and purity of the formed ternary and quaternary perovskites. Moreover, considering the low intensity luminescence observed in the steady-state experiments, free carriers form the dominant species generated upon excitation. We believe that boosting the fraction of photogenerated charge carriers is advantageous in applications for energy conversion and for sensors. A deeper investigation of the involved photophysical processes is currently ongoing and expected to shed more light on the efficiency of the charge carrier generation.

Finally, proof-of-concept photodetector devices are fabricated and characterized to compare the performance of the microcrystals obtained by the proposed two-step CE synthesis to those obtained by a direct one-step synthesis method. Therefore, the cation exchanged $Cs_2AgBiBr_6$ MCs are compared with $Cs_2AgBiBr_6$ MCs which are synthesized directly via an antisolvent precipitation method (see experimental section). They exhibit a similar octahedral shape and are slightly smaller than the CE MCs (Figure S7). For the preparation of the films, a simple spin-coating method was used.[42,44] First, the MCs from the two different synthesis procedures are dissolved in DMSO to get 0.5 M clear solutions. 100 µL of these solutions are spin-coated in a glovebox on clean and ozonized glass substrates. The resulting thin films are then dried for 20 min under inert atmosphere at 80 °C and annealed for 5 min in a furnace at 285 °C. Finally, interdigitated gold contacts are evaporated on top. Upon applying a bias voltage, the generated current is probed in dark and under white light illumination (Figure 4a,b). A 6.7 signal-to-noise (S/N) ratio was calculated for the cation exchanged film compared to a 1.6 S/N ratio for the film based on directly synthesized DP MCs. This is a 4-fold enhancement for the newly proposed synthesis method, reflecting the better controlled stoichiometry in the cation exchanged material. To further highlight the improved response of the cation exchanged film over the direct synthesis, we have conducted photo-switching measurements at an applied voltage of 30 V (Figure 4c). Similar rise and decay times smaller than 1s can be inferred from the graph. Furthermore, it can be

seen that the ON/OFF ratio of the cation exchanged film is higher compared to the solution-based synthesized film. This indicates a stronger sensitivity and improved quality of the crystals synthesized by the two-step cation exchange process.

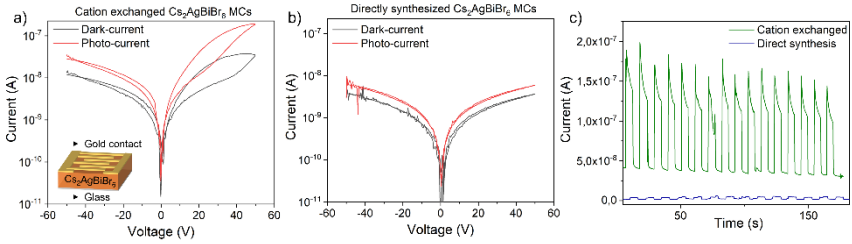

Figure 4. The current-voltage (I-V) curves of the devices fabricated with a) cation exchanged $Cs_2AgBiBr_6$ MCs and b) directly synthesized $Cs_2AgBiBr_6$ MCs in dark and under white light (power density: 180 mW/cm^2). Inset shows the device configuration. c) Photo-switching measurements at 30 V of the devices based on cation-exchanged (green) and directly precipitated (blue) $Cs_2AgBiBr_6$ MCs.

5.3 Conclusion

In this work, the reaction mechanism from ternary $Cs_3Bi_2Br_9$ to quaternary $Cs_2AgBiBr_6$ lead-free perovskite structures has been studied. This research provides, for the first time, a complete chemical conversion of perovskite materials via cation exchange. A combination of techniques was used, including powder X-ray diffraction (XRD), Raman spectroscopy, UV-Vis diffuse reflectance and photoluminescence spectroscopy to understand the phase evolution as well as the changes in structural and optical properties of the materials at different stages of the reaction. By analyzing the XRD patterns of intermediate samples, the degree of phase transformation could be identified at each time step and the growth kinetics of the reaction were quantitatively exacted. The Raman patterns indicated a homogeneous shift with periodic intensity changes, which confirmed that the transformation proceeded in all directions, as supported by the spherulitic (3-dimensional) and homogeneous growth derived from the Avrami equation. Furthermore, a proof-of-concept photodetector device indicated that the $Cs_2AgBiBr_6$ microcrystals obtained by cation exchange exhibit improved photoresponse when compared to those obtained by the direct antisolvent precipitation synthesis method. This work demonstrated that the cation exchange process is a promising path towards

homogenous perovskite materials, and that a further in-depth study of the conversion reaction across intermediates could also provide more insights into the growth mechanism of ultrapure end compounds for the application in high-end optoelectronics.

5.4 Supporting Information

5.4.1 Experimental Section

Materials: All precursor chemicals were obtained commercially from either Alfa Aesar (CsBr, 99%), Thermo Scientific ($BiBr_3$, 97% and HBr, pure, 48 w%), Chem-Lab (AgBr, 99+%) without any further purification.

Synthesis of $Cs_3Bi_2Br_9$ crystals at room temperature: 0.213 g (1 mmol) of CsBr was dissolved in 1 mL of 48 w% HBr and 0.296 g (0.66 mmol) of $BiBr_3$ in 2 mL of 48 w% HBr by sonication. Next, they were mixed in 4 mL 48 w% HBr under ambient conditions upon constant stirring, which results in yellow precipitation, indicating the formation of $Cs_3Bi_2Br_9$.

Cation exchange into $Cs_2AgBiBr_6$ crystals: different amounts 0.141 g (0.75 mmol), 0.188 g (1 mmol) and 0.282 g (1.5 mmol) of AgBr were weighed and dissolved in 3, 4, and 6 mL of 48 w% HBr respectively by sonication. They were then added to the previously made $Cs_3Bi_2Br_9$ suspension and reacted for 60, 30 and 15 min respectively upon constant stirring, resulting in the formation of dark orange, double perovskite microcrystals. To investigate the transformation, the reactions were stopped at a 2.5 min interval by vacuum filtration, after which the resulting powders were vacuum dried at room temperature.

Directly synthesized $Cs_2AgBiBr_6$ MCs via anti-solvent precipitation: a precursor solution was prepared by dissolving 0.426 g (2 mmol) of CsBr, 0.449 g (1 mmol) of $BiBr_3$ and 0.188 g (1 mmol) of AgBr in 10 mL of 48 w% HBr while stirring at 120 °C. Next, 4 mL of this solution was added to 50 mL of isopropanol upon vigorous stirring at room temperature for 2 hours. This resulted in an orange precipitation, which was then separated by centrifugation at 3000 rpm for 5 min. Finally, the powder was vacuum dried at 60 °C.

Fabrication of photodetector devices: the $Cs_2AgBiBr_6$ MCs were first dissolved in DMSO to get 0.5 M clear solutions. 100 µl of this solution was then spin coated (8 rotations per second (rps) for 5'', 66 rps for 30'') in a glovebox on a

clean and ozonized glass substrate. The resulting thin film was then dried for 20 min under inert atmosphere at 80 °C and annealed at 285 °C for 5 min in a furnace. Finally, interdigitated gold contacts were evaporated on top.

5.4.2 Material Characterization

Scanning electron microscopy (SEM) was used to obtain images of the crystals. They were recorded on a FEI-Q FEG250 instrument.

X-ray diffraction (XRD) patterns were obtained using a Malvern PANalytical Empyrean diffractometer with Cu as the anode of the X-ray source (Cu $K_{\alpha1}$: 1.5406 Å; Cu $K_{\alpha2}$: 1.5444 Å) and a PIXcel3D solid-state detector. The powder samples were measured in transmission geometry at room temperature within a 2θ range of 5 – 45° and a step size of 0.013°.

Raman spectroscopy measurements were carried out using a confocal Raman microscope (MonoVista CRS+). An excitation wavelength of 785 nm (0.871 mW laser power) was chosen for all the samples and was directed on the samples through a 10X objective with a numerical aperture of 0.3.

***In situ* UV–Vis Diffuse Reflectance** measurements were performed using a PerkinElmer Lambda 950 UV-Vis spectrophotometer with an integrating sphere. The data was acquired at room temperature between 400 and 750 nm with a 1 nm step. The reference material to calibrate the baseline was $BaSO_4$ powder. Finally, the Kubelka-Munk function was utilized to convert the diffused reflectance (R) into F(R) according to the equation F(R) = (1 − R)2/2R.

Steady state photoluminescence (PL) excitation-emission maps were measured with an excitation range between 250 nm and 600 nm with a step of 5 nm and an emission range between 300 and 800 nm with a step of 5 nm via an Edinburgh FLS980 fluorimeter.

Femtosecond Fluorescence Up-Conversion was measured and analyzed as was described by Grandjean *et al.*[45] The powder samples were measured in a quartz cuvette and by a laser pulse of 400 nm with a power of 2 μW. The fluorescence light originating from the samples was efficiently collected after it is filtered by a 430-nm long pass filter to eliminate scattered light. Fluorescence gating was carried out under magic angle conditions within time windows of 6 and 50 ps. To prevent photoconversion or photodegradation, the samples continuously moved during the measurements. In order to enhance the signal to noise ratio, each measurement was averaged 15 times

at 128 delay positions. Here, a delay position refers to the time interval between the arrival of the pump and gate pulses at the sample position.

Nanosecond to Millisecond Time-resolved Luminescence spectra were obtained using the setup as was described by Grandjean *et al.*[45] Initially, a 355-nm laser pulse (8 ns, 10 Hz) was generated by a pulsed Nd:YAG laser, which was used to pump an Optical Parametric Amplifier (OPO, BasiScan/120 GWU-Lasertechnik Vertriebsgesselshaft m.b.h). The OPO was employed to tune the wavelength of the generated pulses and used to excite the samples. By using a 300-mm focal length lens, the excitation light was focused on the sample and a small part of this light was sent to a fast photodiode to generate a reference signal. The powder samples were measured in a quartz cuvette in the right angle configuration and a time window of 2 μs was used to perform the experiments.

Photoconductivity I–V measurements in dark and under nature light (power density: 180 mW/cm^2) were measured with a Keithley 2400 source meter. The photo-switching measurements were performed by manually pass or block the incoming light onto the device with the use of a slab.

5.4.3 Supporting Information for Results and Discussion

Rietveld refinement

Table S1a. Rietveld refinement parameters for $Cs_3Bi_2Br_9$ with space group P-*3m1*.

Sample	a=b (Å)	c (Å)	α = β	γ	Volume (Å^3)	χ^2
$Cs_3Bi_2Br_9$	7.964(1)	9.849(8)	90	120	541.038(8)	3.43

Table S1b. Rietveld refinement parameters for $Cs_3Bi_2Br_9$ with space group P-*3m1*.

Cation-Br	Bond length (Å)	Br-Cation-Br	Bond angle (°)
Cs1-Br1	3.982	Br1-Bi1-Br2	172.2
Cs1-Br2	4.043	Br1-Bi1-Br1	83.78
Cs2-Br1	4.008	Br1-Bi1-Br2	90.43
Cs2-Br2	3.982 and 3.973	Br2-Bi1-Br2	94.8
Bi-Br1	2.982		
Bi-Br2	2.660		

Table S2a. Rietveld refinement parameters for $Cs_2AgBiBr_6$ with space group P*m-3m*.

Sample	a=b=c (Å)	α = β = γ	Volume (Å^3)	χ^2
$Cs_2AgBiBr_6$	11.280(3)	90	1435.373(9)	3.92

Table S2b. Rietveld refinement parameters for $Cs_2AgBiBr_6$ with space group P*m-3m*.

Cation-Br	Bond length (Å)	Br-Cation-Br	Bond angle (°)
Cs-Br	3.988	Br-Bi-Br	180
Bi-Br	2.806	Br-Bi-Br	90
Ag-Br	2.834	Br-Ag-Br	180
		Br-Ag-Br	90

Synthesis

Scheme S1. Scheme of the cation exchange process from $Cs_3Bi_2Br_9$ to $Cs_2AgBiBr_6$.

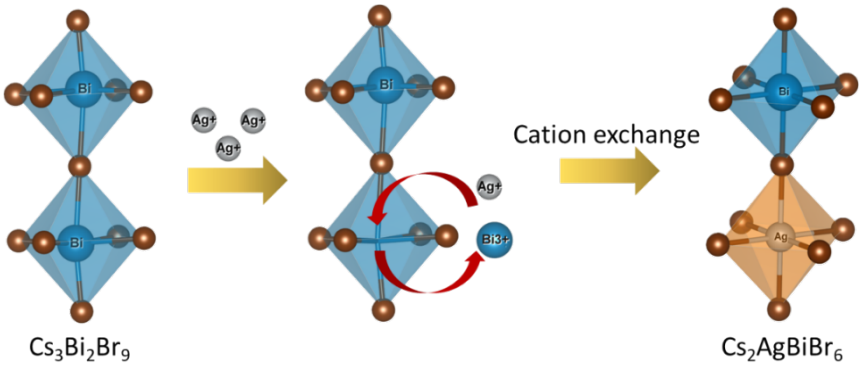

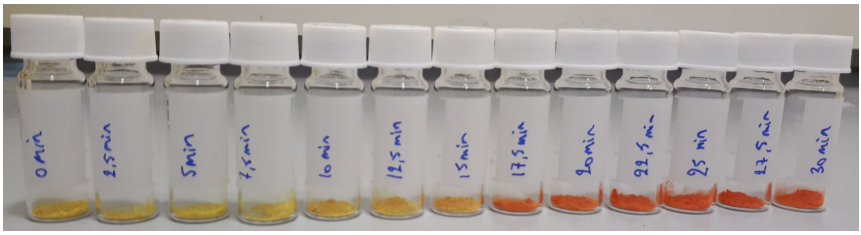

Figure S1. Gradual color change during the transformation from $Cs_3Bi_2Br_9$ (0 min) to $Cs_2AgBiBr_6$ (30 min).

X-ray diffraction

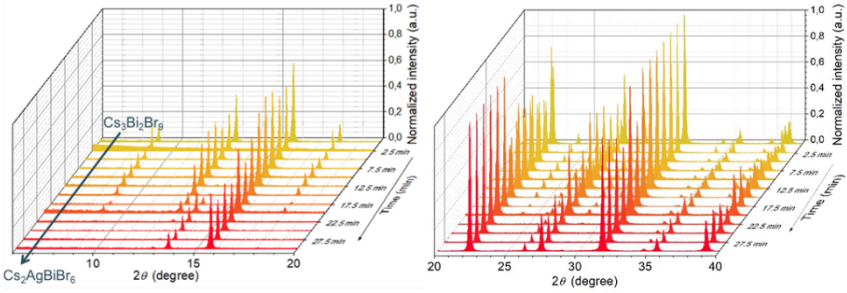

Figure S2. X-ray diffraction (XRD) patterns of all intermediates of the transformation upon addition of 1 mmol of AgBr.

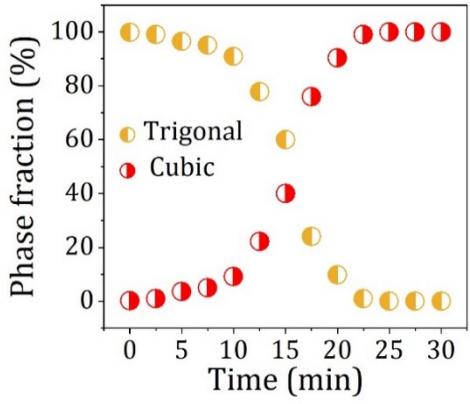

Figure S3. Relative percentages of both the trigonal (yellow) and cubic (orange) crystal structures of all intermediates of the transformation upon addition of 1 mmol of AgBr.

Solid state reaction

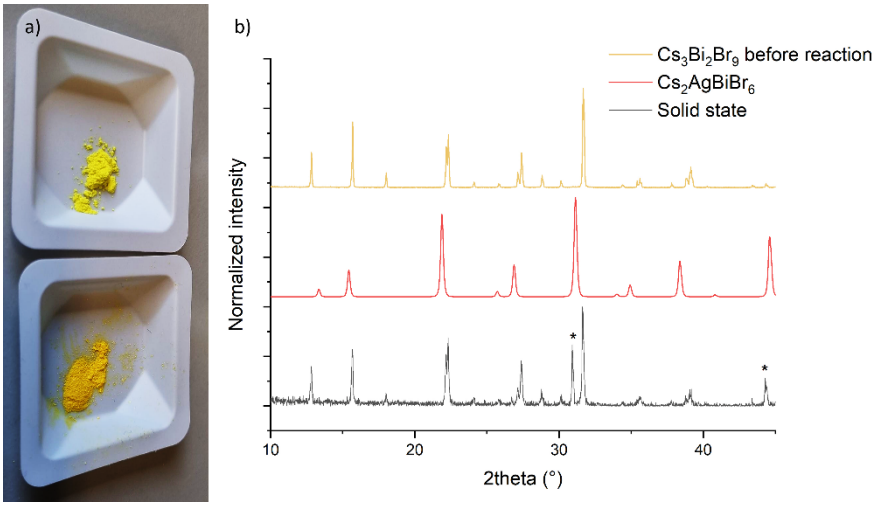

Figure S4. a) Color change during a solid state reaction, performed by grinding earlier prepared and vacuum dried $Cs_3Bi_2Br_9$ crystals together with AgBr. Afterwards, they are heated at 60 °C in a vacuum oven and a (partial) transition towards an orange color can be observed after 6 days. This confirms that the transition towards the double perovskite can happen without the presence of solvent. However, the possibility of recrystallization cannot be ruled out completely. b) XRD pattern after the solid state reaction, indicating peaks from the cubic $Cs_2AgBiBr_6$ structure start to appear at 30.9 and 44.3°.

Tauc plot

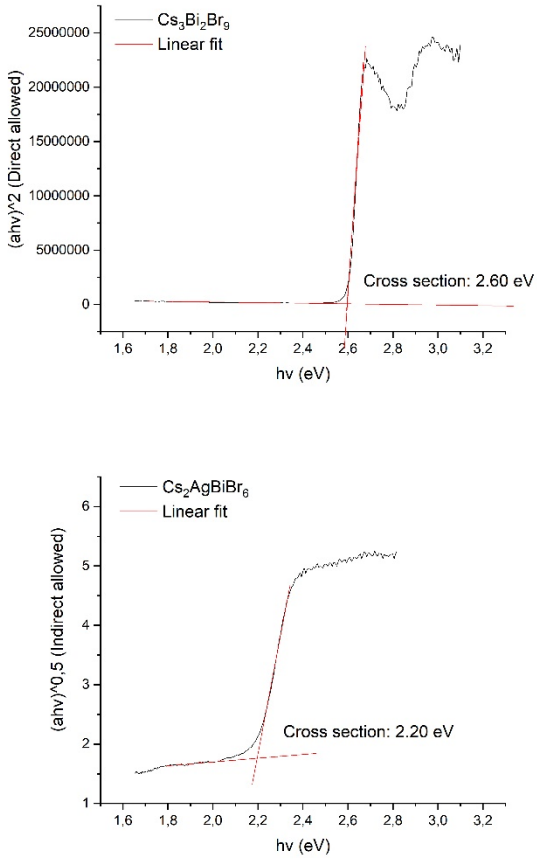

Figure S5. Tauc plots, indicating a direct bandgap of 2.60 eV for $Cs_3Bi_2Br_9$ (left) and an indirect bandgap of 2.20 eV for $Cs_2AgBiBr_6$ (right).

Steady-state photoluminescence

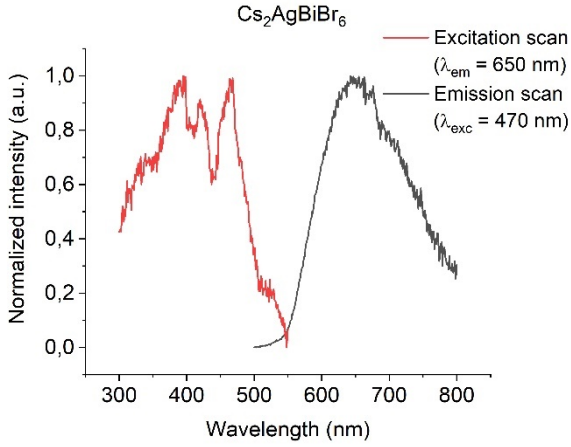

Figure S6. Excitation-emission spectra of $Cs_2AgBiBr_6$ microcrystals prepared by cation exchange.

Fs fluorescence up-conversion

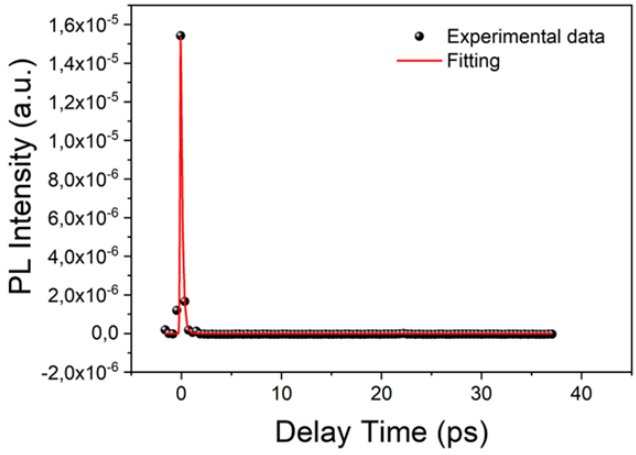

Figure S7. Fs fluorescence up-conversion decay trace (black) and the corresponding fit (ref) of $Cs_3Bi_2Br_9$ (λ_{exc} = 400 nm, λ_{em} = 480 nm).

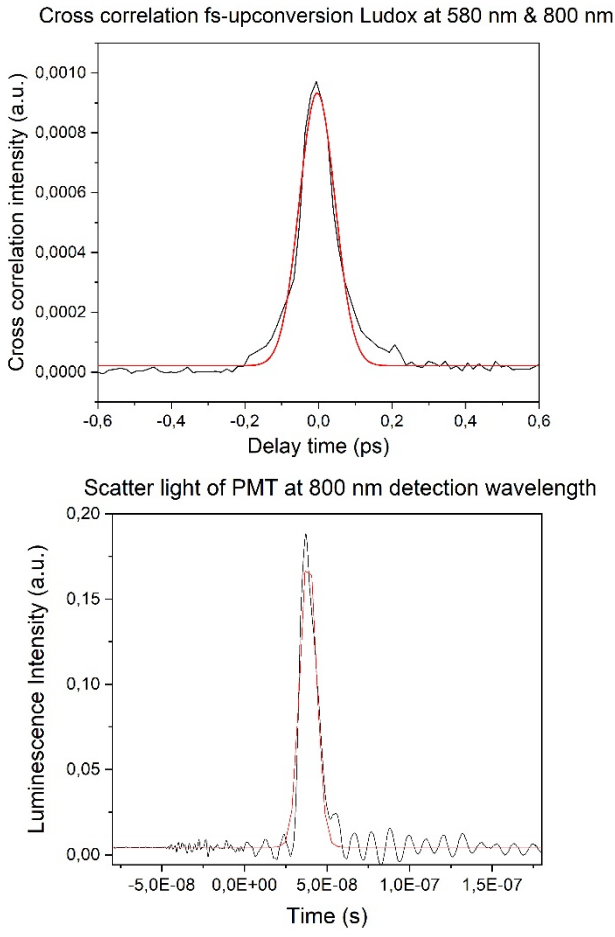

Figure S8. Pulse profiles of the fs up-conversion (left) and ns-ms luminescence setups (right).

Directly synthesized $Cs_2AgBiBr_6$ microcrystals

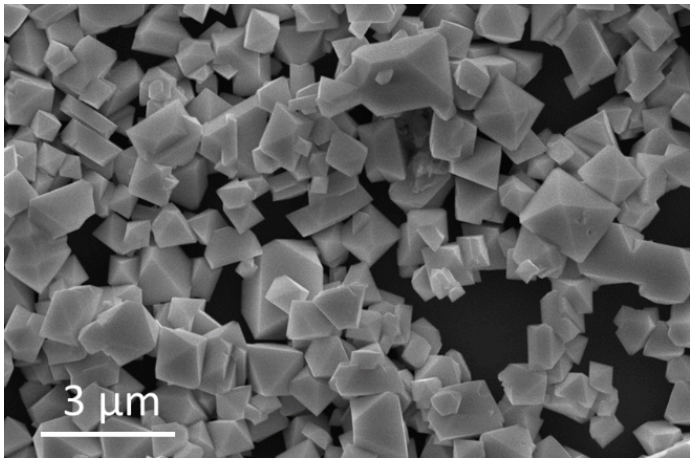

Figure S9. Scanning electron microscope (SEM) image of the $Cs_2AgBiBr_6$ perovskite as prepared by the direct synthesis method.

5.5 References

(1) Liu, D.; Kelly, T. L. Perovskite Solar Cells with a Planar Heterojunction Structure Prepared Using Room-Temperature Solution Processing Techniques. *Nature Photon* **2014**, *8* (2), 133–138. https://doi.org/10.1038/nphoton.2013.342.

(2) Wei, H.; Fang, Y.; Mulligan, P.; Chuirazzi, W.; Fang, H.-H.; Wang, C.; Ecker, B. R.; Gao, Y.; Loi, M. A.; Cao, L.; Huang, J. Sensitive X-Ray Detectors Made of Methylammonium Lead Tribromide Perovskite Single Crystals. *Nature Photonics* **2016**, *10* (5), 333–340. https://doi.org/10.1038/NPHOTON.2016.41.

(3) Jiang, Q.; Zhang, L.; Wang, H.; Yang, X.; Meng, J.; Liu, H.; Yin, Z.; Wu, J.; Zhang, X.; You, J. Enhanced Electron Extraction Using SnO2 for High-Efficiency Planar-Structure HC(NH2)2PbI3-Based Perovskite Solar Cells. *Nature Energy* **2017**, *2*, 16177. https://doi.org/10.1038/nenergy.2016.177.

(4) Mahmud, M. A.; Duong, T.; Peng, J.; Wu, Y.; Shen, H.; Walter, D.; Nguyen, H. T.; Mozaffari, N.; Tabi, G. D.; Catchpole, K. R.; Weber, K. J.; White, T. P. Origin of Efficiency and Stability Enhancement in High-Performing Mixed Dimensional 2D-3D Perovskite Solar Cells: A Review. *Advanced Functional Materials* **2022**, *32* (3), 2009164. https://doi.org/10.1002/adfm.202009164.

(5) Bhatia, H.; Ghosh, B.; Debroye, E. Colloidal FAPbBr3 Perovskite Nanocrystals for Light Emission: What's Going On? *J. Mater. Chem. C* **2022**. https://doi.org/10.1039/D2TC01373H.

(6) Huang, H.; Verhaeghe, D.; Weng, B.; Ghosh, B.; Zhang, H.; Hofkens, J.; Steele, J. A.; Roeffaers, M. B. J. Metal Halide Perovskite Based Heterojunction Photocatalysts. *Angewandte Chemie* **2022**, *134* (24), e202203261. https://doi.org/10.1002/ange.202203261.

(7) Clinckemalie, L.; Valli, D.; Roeffaers, M. B. J.; Hofkens, J.; Pradhan, B.; Debroye, E. Challenges and Opportunities for CsPbBr3 Perovskites in Low- and High-Energy Radiation Detection. *ACS Energy Lett.* **2021**, *6* (4), 1290–1314. https://doi.org/10.1021/acsenergylett.1c00007.

(8) Pradhan, B.; Kumar, G. S.; Sain, S.; Dalui, A.; Ghorai, U. K.; Pradhan, S. K.; Acharya, S. Size Tunable Cesium Antimony Chloride Perovskite Nanowires and Nanorods. *Chem. Mater.* **2018**, *30* (6), 2135–2142. https://doi.org/10.1021/acs.chemmater.8b00427.

(9) Ghosh, S.; Pradhan, B. Lead-Free Metal Halide Perovskite Nanocrystals: Challenges, Applications, and Future Aspects. *ChemNanoMat* **2019**, *5* (3), 300–312. https://doi.org/10.1002/cnma.201800645.

(10) Lehner, A. J.; Fabini, D. H.; Evans, H. A.; Hébert, C.-A.; Smock, S. R.; Hu, J.; Wang, H.; Zwanziger, J. W.; Chabinyc, M. L.; Seshadri, R. Crystal and Electronic Structures of Complex Bismuth Iodides A3Bi2I9 (A = K, Rb,

Cs) Related to Perovskite: Aiding the Rational Design of Photovoltaics. *Chem. Mater.* **2015**, *27* (20), 7137–7148. https://doi.org/10.1021/acs.chemmater.5b03147.

(11) Bass, K. K.; Estergreen, L.; Savory, C. N.; Buckeridge, J.; Scanlon, D. O.; Djurovich, P. I.; Bradforth, S. E.; Thompson, M. E.; Melot, B. C. Vibronic Structure in Room Temperature Photoluminescence of the Halide Perovskite $Cs_3Bi_2Br_9$. *Inorg. Chem.* **2017**, *56* (1), 42–45. https://doi.org/10.1021/acs.inorgchem.6b01571.

(12) Dai, Y.; Tüysüz, H. Lead-Free Cs3Bi2Br9 Perovskite as Photocatalyst for Ring-Opening Reactions of Epoxides. *ChemSusChem* **2019**, *12* (12), 2587–2592. https://doi.org/10.1002/cssc.201900716.

(13) Hoye, R. L. Z.; Eyre, L.; Wei, F.; Brivio, F.; Sadhanala, A.; Sun, S.; Li, W.; Zhang, K. H. L.; MacManus-Driscoll, J. L.; Bristowe, P. D.; Friend, R. H.; Cheetham, A. K.; Deschler, F. Fundamental Carrier Lifetime Exceeding 1 Ms in Cs2AgBiBr6 Double Perovskite. *Advanced Materials Interfaces* **2018**, *5* (15), 1800464. https://doi.org/10.1002/admi.201800464.

(14) Keshavarz, M.; Debroye, E.; Ottesen, M.; Martin, C.; Zhang, H.; Fron, E.; Küchler, R.; Steele, J. A.; Bremholm, M.; Van de Vondel, J.; Wang, H. I.; Bonn, M.; Roeffaers, M. B. J.; Wiedmann, S.; Hofkens, J. Tuning the Structural and Optoelectronic Properties of Cs2AgBiBr6 Double-Perovskite Single Crystals through Alkali-Metal Substitution. *Advanced Materials* **2020**, *32* (40), 2001878. https://doi.org/10.1002/adma.202001878.

(15) Steele, J. A.; Pan, W.; Martin, C.; Keshavarz, M.; Debroye, E.; Yuan, H.; Banerjee, S.; Fron, E.; Jonckheere, D.; Kim, C. W.; Baekelant, W.; Niu, G.; Tang, J.; Vanacken, J.; Van der Auweraer, M.; Hofkens, J.; Roeffaers, M. B. J. Photophysical Pathways in Highly Sensitive Cs2AgBiBr6 Double-Perovskite Single-Crystal X-Ray Detectors. *Advanced Materials* **2018**, *30* (46), 1804450. https://doi.org/10.1002/adma.201804450.

(16) Yin, L.; Wu, H.; Pan, W.; Yang, B.; Li, P.; Luo, J.; Niu, G.; Tang, J. Controlled Cooling for Synthesis of Cs2AgBiBr6 Single Crystals and Its Application for X-Ray Detection. *Advanced Optical Materials* **2019**, *7* (19), 1900491. https://doi.org/10.1002/adom.201900491.

(17) Zong, Y.; Zhou, Y.; Ju, M.; Garces, H. F.; Krause, A. R.; Ji, F.; Cui, G.; Zeng, X. C.; Padture, N. P.; Pang, S. Thin-Film Transformation of NH4PbI3 to CH3NH3PbI3 Perovskite: A Methylamine-Induced Conversion–Healing Process. *Angewandte Chemie* **2016**, *128* (47), 14943–14947. https://doi.org/10.1002/ange.201609529.

(18) Nedelcu, G.; Protesescu, L.; Yakunin, S.; Bodnarchuk, M. I.; Grotevent, M. J.; Kovalenko, M. V. Fast Anion-Exchange in Highly Luminescent Nanocrystals of Cesium Lead Halide Perovskites (CsPbX3, X = Cl, Br, I). *Nano Lett.* **2015**, *15* (8), 5635–5640. https://doi.org/10.1021/acs.nanolett.5b02404.

(19) Akkerman, Q. A.; D'Innocenzo, V.; Accornero, S.; Scarpellini, A.; Petrozza, A.; Prato, M.; Manna, L. Tuning the Optical Properties of Cesium Lead Halide Perovskite Nanocrystals by Anion Exchange Reactions. *J. Am. Chem. Soc.* **2015**, *137* (32), 10276–10281. https://doi.org/10.1021/jacs.5b05602.

(20) Li, Z.; Saruyama, M.; Asaka, T.; Tatetsu, Y.; Teranishi, T. Determinants of Crystal Structure Transformation of Ionic Nanocrystals in Cation Exchange Reactions. *Science* **2021**, *373* (6552), 332–337. https://doi.org/10.1126/science.abh2741.

(21) De Trizio, L.; Manna, L. Forging Colloidal Nanostructures via Cation Exchange Reactions. *Chem. Rev.* **2016**, *116* (18), 10852–10887. https://doi.org/10.1021/acs.chemrev.5b00739.

(22) Roman, B. J.; Otto, J.; Galik, C.; Downing, R.; Sheldon, M. Au Exchange or Au Deposition: Dual Reaction Pathways in Au–CsPbBr3 Heterostructure Nanoparticles. *Nano Lett.* **2017**, *17* (9), 5561–5566. https://doi.org/10.1021/acs.nanolett.7b02355.

(23) Le, Q. V.; Lee, J. W.; Sohn, W.; Jang, H. W.; Kim, J. K.; Kim, S. Y. Low Temperature Solution-Processable Cesium Lead Bromide Microcrystals for Light Conversion. *Crystal Growth & Design* **2018**, *18* (5), 3161–3166. https://doi.org/10.1021/acs.cgd.8b00264.

(24) Rodríguez-Carvajal, J. Recent Advances in Magnetic Structure Determination by Neutron Powder Diffraction. *Physica B: Condensed Matter* **1993**, *192* (1), 55–69. https://doi.org/10.1016/0921-4526(93)90108-I.

(25) Slavney, A. H.; Hu, T.; Lindenberg, A. M.; Karunadasa, H. I. A Bismuth-Halide Double Perovskite with Long Carrier Recombination Lifetime for Photovoltaic Applications. *J. Am. Chem. Soc.* **2016**, *138* (7), 2138–2141. https://doi.org/10.1021/jacs.5b13294.

(26) Du, K.; Meng, W.; Wang, X.; Yan, Y.; Mitzi, D. B. Bandgap Engineering of Lead-Free Double Perovskite Cs2AgBiBr6 through Trivalent Metal Alloying. *Angewandte Chemie International Edition* **2017**, *56* (28), 8158–8162. https://doi.org/10.1002/anie.201703970.

(27) Paul, S.; Dalal, B.; Jana, R.; Shit, A.; Datta, A.; De, S. K. Enhanced Photophysical Properties of Bi2S3/AgBiS2 Nanoheterostructures Synthesized via Ag(I) Cation Exchange-Mediated Transformation of Binary Bi2S3. *J. Phys. Chem. C* **2020**, *124* (23), 12824–12833. https://doi.org/10.1021/acs.jpcc.0c03487.

(28) Wang, J.; Li, L.; Yu, H.; Guan, F.; Wang, D. Binary–Ternary Bi2S3–AgBiS2 Rod-to-Rod Transformation via Anisotropic Partial Cation Exchange Reaction. *Inorg. Chem.* **2019**, *58* (19), 12998–13006. https://doi.org/10.1021/acs.inorgchem.9b01917.

(29) Li, X.; Wu, Y.; Zhang, S.; Cai, B.; Gu, Y.; Song, J.; Zeng, H. CsPbX3 Quantum Dots for Lighting and Displays: Room-Temperature Synthesis, Photoluminescence Superiorities, Underlying Origins and

White Light-Emitting Diodes. *Advanced Functional Materials* **2016**, *26* (15), 2435–2445. https://doi.org/10.1002/adfm.201600109.

(30) Basu, T.; Kishore, V. V. R.; Gohil, S.; Singh, K.; Mohapatra, N.; Bhattacharjee, S.; Gonde, B.; Lalla, N. P.; Mahadevan, P.; Ghosh, S.; Sampathkumaran, E. V. Displacive-Type Ferroelectricity from Magnetic Correlations within Spin-Chain. *Sci Rep* **2014**, *4* (1), 5636. https://doi.org/10.1038/srep05636.

(31) Saha, R. A.; Halder, A.; Saha-Dasgupta, T.; Fu, D.; Itoh, M.; Ray, S. Covalency Driven Modulation of Paramagnetism and Development of Lone Pair Ferroelectricity in Multiferroic Pb 3 TeMn 3 P 2 O 14. *Phys. Rev. B* **2020**, *101* (18), 180406. https://doi.org/10.1103/PhysRevB.101.180406.

(32) Xu, J.-T.; Yuan, J.-J.; Cheng, S.-Y. SAXS/WAXS/DSC Studies on Crystallization of a Polystyrene-b-Poly(Ethylene Oxide)-b-Polystyrene Triblock Copolymer with Lamellar Morphology and Low Glass Transition Temperature. *European Polymer Journal* **2003**, *11* (39), 2091–2098. https://doi.org/10.1016/S0014-3057(03)00155-1.

(33) Grothe, H.; Tizek, H.; Waller, D.; Stokes, D. J. The Crystallization Kinetics and Morphology of Nitric Acid Trihydrate. *Phys. Chem. Chem. Phys.* **2006**, *8* (19), 2232–2239. https://doi.org/10.1039/B601514J.

(34) Park, S. J.; Kim, A. R.; Hong, J. T.; Park, J. Y.; Lee, S.; Ahn, Y. H. Crystallization Kinetics of Lead Halide Perovskite Film Monitored by In Situ Terahertz Spectroscopy. *J. Phys. Chem. Lett.* **2017**, *8* (2), 401–406. https://doi.org/10.1021/acs.jpclett.6b02691.

(35) Pistor, P.; Meyns, M.; Guc, M.; Wang, H.-C.; Marques, M. A. L.; Alcobé, X.; Cabot, A.; Izquierdo-Roca, V. Advanced Raman Spectroscopy of Cs2AgBiBr6 Double Perovskites and Identification of Cs3Bi2Br9 Secondary Phases. *Scripta Materialia* **2020**, *184*, 24–29. https://doi.org/10.1016/j.scriptamat.2020.03.040.

(36) Valakh, M. Ya.; Lisitsa, M. P.; Trilis, A. V.; Yaremko, A. M.; Peresh, E. Yu. Raman Scattering in A3B2C9 Ferroelectric Crystals. *Phys. Solid State* **1997**, *39* (8), 1289–1291. https://doi.org/10.1134/1.1130062.

(37) Steele, J. A.; Puech, P.; Keshavarz, M.; Yang, R.; Banerjee, S.; Debroye, E.; Kim, C. W.; Yuan, H.; Heo, N. H.; Vanacken, J.; Walsh, A.; Hofkens, J.; Roeffaers, M. B. J. Giant Electron–Phonon Coupling and Deep Conduction Band Resonance in Metal Halide Double Perovskite. *ACS Nano* **2018**, *12* (8), 8081–8090. https://doi.org/10.1021/acsnano.8b02936.

(38) Timmermans, C. W. M.; Blasse, G. On the Luminescence of Cs3Bi2Br9 Single Crystals. *physica status solidi (b)* **1981**, *106* (2), 647–655. https://doi.org/10.1002/pssb.2221060230.

(39) J. Zelewski, S.; M. Urban, J.; Surrente, A.; K. Maude, D.; Kuc, A.; Schade, L.; D. Johnson, R.; Dollmann, M.; K. Nayak, P.; J. Snaith, H.; Radaelli, P.; Kudrawiec, R.; J. Nicholas, R.; Plochocka, P.; Baranowski,

M. Revealing the Nature of Photoluminescence Emission in the Metal-Halide Double Perovskite Cs 2 AgBiBr 6. *Journal of Materials Chemistry C* **2019**, *7* (27), 8350–8356. https://doi.org/10.1039/C9TC02402F.

(40) Shi, M.; Li, G.; Tian, W.; Jin, S.; Tao, X.; Jiang, Y.; Pidko, E. A.; Li, R.; Li, C. Understanding the Effect of Crystalline Structural Transformation for Lead-Free Inorganic Halide Perovskites. *Advanced Materials* **2020**, *32* (31), 2002137. https://doi.org/10.1002/adma.202002137.

(41) Miyata, K.; Meggiolaro, D.; Trinh, M. T.; Joshi, P. P.; Mosconi, E.; Jones, S. C.; De Angelis, F.; Zhu, X.-Y. Large Polarons in Lead Halide Perovskites. *Science Advances* **2017**, *3* (8), e1701217. https://doi.org/10.1126/sciadv.1701217.

(42) Zhang, H.; Debroye, E.; Zheng, W.; Fu, S.; Virgilio, L. D.; Kumar, P.; Bonn, M.; Wang, H. I. Highly Mobile Hot Holes in Cs2AgBiBr6 Double Perovskite. *Science Advances* **2021**, *7* (52), eabj9066. https://doi.org/10.1126/sciadv.abj9066.

(43) Hossain, M.; Sheikh, M. S.; Rao, K. D. M. Hot-Spin Casting Synthesis of Freestanding Cs2AgBiBr6 Double Perovskite Facet-Oriented Microcrystals for Efficient Photodetectors. *Advanced Materials Interfaces* **2021**, *8* (18), 2100570. https://doi.org/10.1002/admi.202100570.

(44) Lei, L.-Z.; Shi, Z.-F.; Li, Y.; Ma, Z.-Z.; Zhang, F.; Xu, T.-T.; Tian, Y.-T.; Wu, D.; Li, X.-J.; Du, G.-T. High-Efficiency and Air-Stable Photodetectors Based on Lead-Free Double Perovskite Cs2AgBiBr6 Thin Films. *J. Mater. Chem. C* **2018**, *6* (30), 7982–7988. https://doi.org/10.1039/C8TC02305K.

(45) D. Grandjean, E. Coutiño-Gonzalez, N. T. Cuong, E. Fron, W. Baekelant, S. Aghakhani, P. Schlexer, F. D'Acapito, D. Banerjee, M. B. J. Roeffaers, M. T. Nguyen, J. Hofkens, P. Lievens, *Science* **2018**, 361, 686–690.

Chapter 6
Conclusion and Outlook

6.1 General Conclusions

In this dissertation, stable, phase-pure, highly crystalline perovskites with excellent photonic properties have been successfully synthesized, characterized and investigated for their potential application as radiation detectors.

In the first part (Chapter 3), we have successfully demonstrated a scalable synthesis and deposition method under ambient conditions for fabricating flexible, uniform, and crack-free films consisting of perovskite MCs. The implementation of the 2D $CsPb_2Br_5$ phase into $CsPbBr_3$ MCs has been investigated, revealing improved stability and tolerance to higher voltage X-ray detection. It has been found that introducing the secondary phase results in a prolonged lifetime due to the presence of additional shallow defects. The dual-phase $CsPbBr_3$-$CsPb_2Br_5$ MCs also exhibit suppressed ion migration, which, in combination with the formed shallow defect states, prevents the building up of polarization in the device configuration. These findings open up promising avenues for future improvements in stability, charge extraction and X-ray image resolution.

In the second part (Chapter 4), chemical vapor deposition has been used as a scalable, solvent-free synthesis method for the fabrication of phase-pure, uniform, and pinhole free $CsPbBr_3$ thin films with excellent charge carrier characteristics. We found that the thickness and coverage of the films can be precisely adjusted by controlling the substrate temperature. The impact of the grain size on the carrier transport properties has been investigated, indicating enhanced mobility upon increased grain size. Additionally, Rb-doping has been shown to improve the external quantum efficiency of the films as photodetectors. The knowledge gained from this work has been utilized to optimize a home-built setup, aiming to further investigate e.g. the influence of dopants on film properties, such as the charge carrier lifetime and conductivity. This work contributes to the development of high-quality perovskite films for high-performance optoelectronic devices in the near future.

In the last part (Chapter 5), a comprehensive study of the reaction mechanism from ternary $Cs_3Bi_2Br_9$ to quaternary $Cs_2AgBiBr_6$ lead-free perovskite structures via cation exchange has been provided. A combination of techniques including XRD, Raman spectroscopy, UV-Vis diffuse reflectance, and photoluminescence spectroscopy has been employed to understand the phase evolution, structural changes, and optical properties at different stages of the reaction. The analysis of the intermediate samples has provided insights

into the chemical conversion process by identifying the degree of phase transformation and quantifying the growth kinetics. Furthermore, the proof-of-concept photodetector device based on $Cs_2AgBiBr_6$ microcrystals obtained by cation exchange has shown improved photoresponse compared to those obtained by direct antisolvent precipitation synthesis. These findings highlight the potential of cation exchange as a promising pathway towards homogeneous perovskite materials for high-end optoelectronics.

As a result, the dual-phase $CsPbBr_3$-$CsPb_2Br_5$ perovskite has been identified as the most promising material for both X-ray and photodetection. However, the optimal preparation method varies depending on the intended application. For X-ray detection, a thicker (~500 µm) layer is necessary, and this can be achieved using the proposed polymer-based deposition method. Conversely, for photodetection, a CVD-grown thin (~200-400 nm) layer is preferred.

Overall, the findings presented in this PhD dissertation contribute to the advancement of both Pb-based MHPs and lead-free perovskite materials for application in X-ray and photodetection. We have addressed three main challenges of perovskite materials, namely material stability, film fabrication, and lead toxicity. The demonstrated scalable synthesis and deposition methods, optimization of the chemical vapor deposition process, and cation exchange approach offer new pathways for improving the performance and stability of perovskite-based devices. The insights gained from this research provide a solid foundation for further studies and pave the way for the development of novel, high-performance, and more efficient perovskite-based optoelectronic devices in the future.

6.2 Outlook

Device fabrication. In chapter 3, we introduce a new fabrication method for producing compact, thick and pinhole-free films. However, as the polymer used in this method is non-conductive, it hampers charge extraction, leaving room for improvement. Therefore, optimization of the amount and type of polymer can be performed to tune the sensitivity and flexibility while maintaining the densely packed films. It might be interesting to explore the use of conductive polymers such as polyaniline or polypyrrole. Importantly, solubility of all components in the desired medium needs to be properly evaluated.

Home-build CVD setup. Further experiments are necessary to optimize the synthesis parameters for the in-house setup to reach phase-pure $CsPbBr_3$ films. The first parameter that should be optimized is the substrate temperature, as lowering the temperature may decrease the number of pinholes and lead to a larger grain size. Furthermore, applying a delayed flow technique might be interesting. By introducing the flow only when the substrate temperature reaches the desired value, it should minimize the loss of $PbBr_2$ precursor due to early evaporation, which otherwise gets carried away in the tube by the carrier gas. Finally, post-synthesis annealing for one hour at 450 °C can be performed to convert the $CsPb_2Br_5$ side phase to $CsPbBr_3$. To enhance the performance of the films as photoactive layer in photodetectors, the next step will be to precisely modify the composition of the material, for example, through doping. Some interesting strategies may include the partial replacement of Cs with other alkali metals or Br with I.

Fabrication of $Cs_2AgBiBr_6$ perovskite using CVD. $Cs_2AgBiBr_6$ SCs have already demonstrated excellent response as photoactive material in X-ray detectors. However, the processability of these SCs is crucial, as flat-panels X-ray detectors used in hospitals are large (e.g. 46 x 46 cm^2) and require large-area coverage, which is challenging to achieve with SCs. Therefore, an alternative approach is to fabricate high-quality double perovskite films via CVD, which has not been previously explored.

*Improvement of other lead-free perovskite*s. In contrast to $Cs_2AgBiBr_6$, the lead-free perovskite $Cs_2AgInCl_6$ exhibits a direct bandgap, making it a promising material for various optoelectronic devices such as LEDs.[1] However, one of the key challenges for $Cs_2AgInCl_6$ is achieving a high PLQY for efficient photonic applications. To address this challenge, significant progress has been made by alloying $Cs_2AgInCl_6$ with Na^+ dopants.[2] Looking into the future, cation exchange transformation could be an interesting approach to gradually introduce foreign ions and to investigate their effects on the bandgap of the material.

Device fabrication of the optimized lead-free perovskites using CVD. Once new promising lead-free perovskite materials have been explored, it is important to test their performance in the desired device applications. As earlier mentioned, the fabrication method for producing compact, thick and pinhole-free films presented in Chapter 3 can be used to create X-ray detectors. To test the response of these materials as photodetectors or LEDs, the synthesis of high-quality thin films using CVD can be a useful approach. The most promising materials can then be chosen to fabricate (flexible)

pixelated photodetector arrays by applying a dry-lift approach, as described in one of the group's recent works.[3]

Fabrication of pixelated perovskite-based detectors. In order to commercialize perovskites, the fabrication of pixelated devices should be optimized. To achieve this, several interesting methods are worth investigating, as summarized in Scheme 1. The most straightforward method involves depositing the contact material using thermal or physical evaporation, with the pattern defined using a mask. This approach is applicable to all materials. Next, photolithography, a commonly used technique in semiconductor device fabrication, could prove beneficial for both X-ray and photodetection applications. Both the dual-phase MCs and cation-exchanged lead-free MCs might be good candidates for this technique, as they have shown high stability to harsh environments. For CVD grown $CsPbBr_3$ thin films, the earlier proposed dry lift-off might be a more suitable technique. Finally, screen or inkjet printing can be explored, offering a suitable option for rapid, cost-effective, and large-scale deposition of contact material.

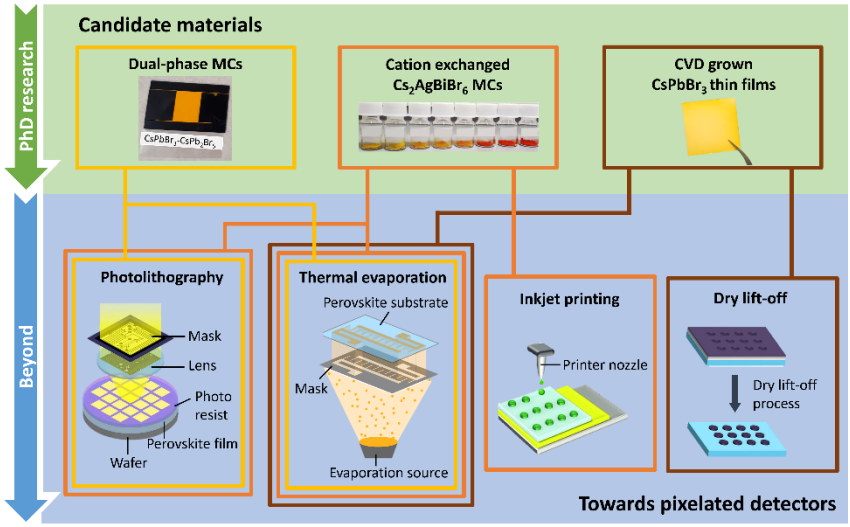

Scheme 1. Technology roadmap indicating interesting fabrication methods for future pixelated detectors.

6.3 References

(1) Mathew, N. P.; Rajeev Kumar, N.; Radhakrishnan, R. First Principle Study of the Structural and Optoelectronic Properties of Direct Bandgap Double Perovskite Cs2AgInCl6. *Materials Today: Proceedings* **2020**, *33*, 1252–1256. https://doi.org/10.1016/j.matpr.2020.03.489.

(2) Liu, Y.; Nag, A.; Manna, L.; Xia, Z. Lead-Free Double Perovskite Cs2AgInCl6. *Angewandte Chemie* **2021**, *133* (21), 11696–11707. https://doi.org/10.1002/ange.202011833.

(3) Xia, B.; Tu, M.; Pradhan, B.; Ceyssens, F.; Tietze, M. L.; Rubio-Giménez, V.; Wauteraerts, N.; Gao, Y.; Kraft, M.; Steele, J. A.; Debroye, E.; Hofkens, J.; Ameloot, R. Flexible Metal Halide Perovskite Photodetector Arrays via Photolithography and Dry Lift-Off Patterning. *Advanced Engineering Materials* **2022**, *24* (1), 2100930. https://doi.org/10.1002/adem.202100930.

Appendix

1. Safety Information

The experimental work in this thesis was performed in accordance with the Code of Practice for Safety in the Lab and the safety guidelines provided in the departmental safety brochure. Detailed information and precautions can be found on the HSE service website (https://admin.kuleuven.be/sab/vgm/algemeen/EN) prior to setting up experiments. It is essential to correctly use personal and collective protective equipment. This includes wearing a lab coat, safety goggles, and gloves and conducting all experiments in the fumehood. Precautions to work with X-ray irradiation include following the "Basic Training Radiation Protection" to understand the danger of X-rays. Furthermore, a dosimeter should always be worn while working. The equipment is a closed box fabricated out of Pb and is designed so that X-rays will not be generated if it is not closed properly. Finally, regularly checking the radiation leakage is performed on a yearly basis. Familiarity with the properties of all chemicals used in the lab, as listed in the MSDS, is strongly recommended before starting any experiment. Prior to repeating any experiment in this dissertation, checking the risk assessments and searches in the KU Leuven hazardous substance database are highly advised. The hazards associated to the used solvents and reagents, classified as risk class E3 to $E4^{+}$, are provided below.

Solvents

- **Acetone**: Highly flammable, irritating to eyes, and causes serious eye irritation.
- **Dimethylformamide** (DMF): May cause harm to the unborn child, harmful by inhalation and in contact with skin, and irritating to eyes.
- **Dimethyl sulfoxide** (DMSO): Slightly irritant to skin.
- **Ethanol**: Highly flammable.
- **Hydrobromic acid** (HBr): Can cause severe skin burns and eye damage by contact. After any exposure, skin should be thoroughly rinsed with water.
- **Isopropyl alcohol**: Highly flammable.
- **Toluene**: Highly flammable, teratogenic, irritating to skin, possible risk of harm to the unborn child, and may cause lung damage if swallowed.

Reagents (E3, E4 or $E4^{+}$)

- **Bismuth bromide** ($BiBr_3$): Can cause severe burns and eye damage.
- **Lead bromide** ($PbBr_2$): Teratogenic and harmful to fertility. Damage to certain organs through prolonged or repeated exposure.
- **Silver bromide** (AgBr): Can cause severe burns and eye damage.

2. List of Publications

1) Lotte Clinckemalie, Rafikul Ali Saha, Donato Valli, Eduard Fron, Maarten B.J. Roeffaers, Johan Hofkens, Bapi Pradhan and Elke Debroye, Transformation of $Cs_3Bi_2Br_9$ to $Cs_2AgBiBr_6$ lead-free perovskite microcrystals through cation exchange, *Advanced Optical Materials*, 2023, 202300578.

2) Lotte Clinckemalie, Donato Valli, Maarten B.J. Roeffaers, Johan Hofkens, Bapi Pradhan and Elke Debroye, Challenges and Opportunities for $CsPbBr_3$ Perovskites in Low- and High-Energy Radiation Detection, *ACS Energy Lett.* 2021, 6, 4, 1290–1314.

3) Gebruers, M., Saha, R., Kubarev, A., Clinckemalie, L., Liao, Y., Debroye, E., Weng, B., and Roeffaers, M., Optimized colloidal growth of hexagonal close-packed Ag microparticles and their stability under catalytic conditions, *New Journal Of Chemistry,* 2022, 46, 13352-13361.

4) Maria Isabel Pintor Monroy, Iakov Goldberg, Karim Elkhouly, Epimitheas Georgitzikis, Lotte Clinckemalie, Guillaume Croes, Nirav Annavarapu, Weiming Qiu, Elke Debroye, Yinghuan Kuang, Maarten BJ Roeffaers, Johan Hofkens, Robert Gehlhaar and Jan Genoe, All-Evaporated, All-Inorganic $CsPbI_3$ Perovskite-Based Devices for Broad-Band Photodetector and Solar Cell Applications, *ACS Appl. Electron. Mater.* 2021, 3, 7, 3023–3033.

3. Student Supervision

Bachelor thesis students:

- **Simon De Hertogh** (2018-2019): Doping of Bismuth based Perovskite Microcrystals in Order to Improve X-ray Conductivity.
- **Arnout Benoy** (2019-2020): Morphology Control of Perovskite Microcrystals using Capping Ligands.
- **Dean Swerts** (2019-2020): Wat is de invloed van dopering op de fysische en chemische eigenschappen van een perovskiet?

Master thesis students:

- **Roeland Baeyens** (2019-2020): Exploring new lead-free perovskite materials for X-ray detection.
- **Jolien Smeets** (2020-2021): Synthesis and characterization of lanthanide doped double perovskite microcrystals for application in X-ray photodetection.
- **Roel Vanden Brande** (2021-2022): Finetuning the deposition of $CsPbBr_3$ perovskite films using chemical vapor deposition.